THE UNIVERSITY *of* EDINBURGH

Two-Dimensional Horizontal (2DH) Boussinesq Modelling of Waves at the Coast

Frances Judge

Doctor of Philosophy

The University of Edinburgh

2017

Declaration of originality

I declare that this thesis has been composed solely by myself and that it has not been submitted, in whole or in part, in any previous application for a degree. Except where stated otherwise by reference or acknowledgement, the work presented is entirely my own.

Signed: _____ Date: _____

Lay Summary

Understanding the behaviour of waves and their interaction with the coast is vital for marine engineers and maritime planners. As sea levels rise due to climate change, low-lying coastal areas and existing sea defences will become increasingly vulnerable to run-up and overtopping by large wave events. Accurate and efficient numerical models are essential tools for the assessment of such events and the impact they have on the coast, so that effective coastal protection can be designed.

This thesis presents a numerical model, or computer program, capable of generating realistic wave events at a coastal location. As waves approach the shoreline, they steepen and eventually break. The numerical model allows the behaviour of such waves to be studied. The model has the capability to represent waves before they break and how they propagate post-breaking.

Standard benchmark test cases are used to verify that the different components of the numerical model are working correctly. The complete model is validated by comparing the numerical simulations of laboratory experiments with high quality experimental data from the UK Coastal Research Facility (UKCRF). The laboratory experiments simulated include the interaction of both regular waves and wave groups with beaches of different configurations. It is found that the numerical model provides satisfactory predictions of the behaviour of waves as they approach the shore, and reproduces most of the flow features of waves and currents in the shallow nearshore environment.

Abstract

Understanding the behaviour of waves and their interaction with the coast is vital for marine engineers and maritime planners. As sea levels rise due to climate change, low-lying coastal areas and existing sea defences will become increasingly vulnerable to run-up and overtopping by large wave events. Accurate and efficient numerical models are essential tools for the assessment of such events and the impact they have on the coast so that effective coastal protection can be designed.

This thesis presents a depth-integrated numerical solver with two horizontal dimensions for modelling waves in the coastal zone from intermediate depth to zero depth. Pre-breaking, the evolution of the water surface is calculated using the enhanced Boussinesq equation set of Madsen and Sørensen (1992). This equation set has improved dispersion characteristics over the classical Boussinesq equations, but with relatively few terms compared to models based on the Navier-Stokes equations, allowing for more efficient numerical modelling while maintaining sufficient accuracy. The equations are discretised using second-order finite differences and solved using the conjugate gradient method with fourth-order Runge-Kutta time stepping. Switching from the Boussinesq equation set to the shallow water equations allows shoaling waves to break, with the broken waves then propagating as bores. The shallow water equations are solved using a finite volume MUSCL-Hancock scheme with an HLLC approximate Riemann solver in order to resolve the behaviour of steep-fronted bores at the shore. The model incorporates a wetting and drying algorithm that models the moving wet/dry front. Waves are generated by a line of independently moving piston paddles, allowing full replication of laboratory experiments. A mapping technique is used in the region of the paddles to map the moving physical domain onto a fixed computational domain to facilitate the solution of the governing equations.

Different aspects of the model are verified using standard benchmark tests. The complete model is then validated by comparing the numerical simulation of laboratory experiments with high quality experimental data from the UK Coastal Research Facility (UKCRF). The laboratory experiments simulated include the interaction of regular waves with sinusoidal and tri-cuspate beaches, and the interaction of both uni-

directional and multi-directional focused wave groups with a plane beach. It is found that the model provides satisfactory wave phase resolution and reproduces most of the flow features of waves and currents in the shallow nearshore environment.

Acknowledgements

I would like to give my most sincere thanks to my supervisor Professor Alistair Borthwick. Studying for my PhD has been a very enjoyable and fulfilling experience, and this is largely due to Alistair's qualities as a supervisor. His guidance, encouragement, advice and friendship are appreciated more than I can say, and I count myself very lucky to be numbered among his students. He has opened many doors for me, and I am very grateful for what he has done for my career. I would also like to thank the ENFORCE team of Alison Raby, Paul Taylor, Jana Orszaghova, Colm Fitzgerald and Colin Whittaker for including me in their research activities and for providing very constructive comments on my work. In particular, I would like to thank Alison Raby, for making herself available to discuss her experimental work, the results of which were used in this thesis; and Jana Orszaghova for her willingness to discuss features of her marvellous model OXBOU, and for her offers to assist in any way possible. My gratitude also goes to Professor David Ingram for his assistance in implementing the parallelised features of the code developed in this work. My love as well as my thanks goes to my parents, whose baby sitting services and general support made my life so much easier. Most of all, I'd like to thank my partner Eamonn, for his unwavering support of all my endeavours.

Contents

Nomenclature

α	Weighting coefficient
Δt	Time stepping interval
Δx	Computational grid resolution in the x-direction
Δy	Computational grid resolution in the y-direction
δ_{nm}	Kronecker delta function
ϵ	Nonlinearity parameter
η	Free-surface elevation above a prescribed horizontal datum
λ	Wavelength
$\mathbf{Q}$	Vector of horizontal fluxes, (q_x, q_y)
$\mathbf{u}$	Vector of horizontal velocity components, (u, v)
μ	Dispersion parameter
ω	Angular frequency
Φ	Velocity potential
ρ	Density
σ_θ	Variance of the angular distribution
τ_{bx}, τ_{by}	Bed friction stresses

Θ	Magnitude of free-surface slope
$\tilde{u}_{\max}$	Maximum wave particle velocity
$\tilde{x}, \tilde{y}$	Transformed x, y coordinates
ε	Eddy viscosity
$\widetilde{B}$	Number of grid points in the x-direction in the moving paddle domain
$\widetilde{C}_f$	Wave bed friction coefficient
ξ	Moving ordinate
ξ_0	Iribarren number
ζ	Free-surface elevation above still water level
A	Coefficient matrix
A_b	Excursion length of the orbital motion at the bed
A_f	Linear focus amplitude
B	Boussinesq dispersion coefficient
$b0$	Initial length in x-direction of moving paddle domain
B_d	Number of grid points in the x-direction in the computational domain
b_θ	Spreading factor
B_{switch}	Switch point between Boussinesq and shallow water equation sets
C	Solitary wave celerity
c	Wave celerity
c_0	Biésel transfer function
C_f	Bed friction coefficient

C_{fcur}	Current bed friction coefficient
d	Total water depth
f	Frequency
f_{ramp}	Ramping function
g	Acceleration due to gravity
H	Wave height
h	Still water depth
$imax$	Number of grid points in the y-direction in the physical domain
$jmax$	Number of grid points in the x-direction in the physical domain
k	Wavenumber
M_T	Dimensionless mixing parameter
R	Wave run-up (vertical)
R_h	Roughness height
r_s	x-coordinate of start of ramping zone
$S(\omega)$	Wave spectral density
T	Wave period
T_{xx}, T_{yy}, T_{xy}	Effective stresses
$U_{19.5}$	Wind velocity at 19.5m above still water level
w	Vertical velocity component
x_f	Focus location
x_p	Paddle displacement
z_b	Bed elevation above a prescribed horizontal datum

Chapter 1

Introduction and literature review

This chapter provides a brief introduction to ocean waves and describes the transformation they undergo as they approach the shore. Numerical models for coastal hydrodynamics are described, with a particular focus on Boussinesq-type models. The aims and objectives of this thesis are explained and an outline given of the thesis contents.

1.1 Ocean waves

Progressive gravity waves are created when shear forces act on a liquid causing its surface to deform, against the restoring forces of gravity and surface tension. Gravity waves of translation occur when the body of liquid is given a sudden displacement; standing waves are gravity waves that form as a result of two waves of equal period travelling in opposite directions. The wavelength gives an indication of the magnitude of the forces at work. Ocean waves range from very short capillary waves, with a typical wavelength of < 2 cm, to tsunamis whose wavelength is of the order of 100s of kilometres, to tidal waves, characterised by a wavelength of half the earth's circumference. The longer the waves, the more important gravity is in relation to surface tension.

Wind generated waves are broadly grouped in to capillary waves, wind sea and swell and typically have periods of up to ~20 s. When waves are generated by the local

wind field, the resulting waves are called wind waves or 'sea'. See Kinsman (1965) for a detailed account of the generation of wind-induced surface waves on water. Wind-induced gravity waves are often irregular and directionally spread; a large number of wave components with varying wave height, period and propagation direction are superimposed and the resulting sea state is referred to as short crested. Swell occurs when the waves propagate away from their area of origin, and naturally separate into groups of common wavelength and direction. This is due to frequency dispersion, where waves of different wave lengths propagate at different speeds, a phenomenon which governs all wind generated waves.

Long waves, with periods ranging from 20-30 s to 40 minutes include surf beats, seiches and tsunamis. Surf beat, first identified by Munk (1949), is an oscillation in the wave set-up at the coast that results from the incoming waves travelling in groups. The oscillation has a period 6-8 times the mean wave period. A seiche is a standing wave in an enclosed (e.g. a lagoon), or a semi-enclosed body of water such a bay or harbour. Seiches are generally caused by a sudden variation in wind and have periods in the range of 2-40 minutes. A tsunami is a series of waves generated by a sudden displacement of a large volume of water, generally by an earthquake or a landslide. Tsunamis typically have periods of 5-60 minutes and wavelengths of hundreds of kilometres in the open ocean, where they can travel at speeds of over 800 km/h. Their very large wavelengths mean that even in deep water, tsunamis can be considered as shallow water waves. Unlike wind-generated or progressive waves, which propagate energy without any significant movement of the water itself, tsunamis transport large amounts of water. Waves with periods of larger than 1 hour, are typically referred to as water-level variations, and include tidal variations and storm surge.

1.2 Wave transformation at the coast

Waves transform as they enter shallower water approaching the coastline. Refraction is caused by the decrease in propagation speed of waves travelling from deeper to shallower water. This results in the wave crests becoming more parallel to the contours of sea bed. Diffraction, where wave energy is transferred from high to low energy regions,

also involves a direction change, as waves interact with a large-scale (often surface-piercing) obstacle, such as a breakwater or a headland. Shoaling is the steepening of waves as they enter shallower water; as the wave speed and wavelength decreases, the wave height increases. This eventually leads to wave breaking, when the wave crest becomes too steep. The region of wave breaking is known as the surf zone. There are four types of breaking waves: spilling, plunging, collapsing, and surging, described in detail in most water waves reference text books, such as Dean and Dalrymple (1991) and Sarpkaya and Isaacson (1981). The Iribarren number, or surf similarity parameter is a dimensionless parameter given by

$$\xi_0 = \frac{\tan\alpha}{\sqrt{H_0/\lambda_0}}, \tag{1.1}$$

where α is the bed slope, H_0 is the offshore wave height and $\lambda_0 = gT^2/2\pi$ is the deep water wavelength, in which T is the period and g is the acceleration due to gravity. The Iribarren number can be used to describe the breaker type, with $\xi_0 > 3.3$ corresponding to a surging or collapsing breaker, $0.5 < \xi_0 < 3.3$ indicating a plunging breaker, while spilling breakers tend to have an Iribarren number of $\xi_0 < 0.5$ (see Battjes (1974)). Low Iribarren numbers are generally associated with a wide surf zone, whereas narrow surf zones tend to correspond to higher values. After breaking, waves travel up the beach as bores.

Wave run-up is defined as the maximum level the water reaches due to the uprush of waves above the still water level (Kobayashi (1999)). It is a combination of wave set-up and swash. Wave set-up is the local increase of the mean water level within the surf zone due to the presence of breaking waves. Swash describes the oscillating fluctuations above the wave set-up, resulting from individual bores, and lower frequency infragravity waves (Guza and Thornton (1982)). The beach region affected by the swash is known as the swash zone.

Breaking waves can generate currents that flow in both the offshore and alongshore directions. A rip current is a strong, narrow, localised current directed away from the beach, out to sea. As waves break approaching the shore, differences in wave set-up cause pressure gradients that drive nearshore circulation. The mass transport of water onshore generates longshore flows which converge to form seaward directed rip currents.

Rip currents typically occur through a depression such as a break in a sand bar, or in the embayments between cusp horns on cuspate beaches. Longshore currents travel parallel to the shoreline, and are generally associated with incoming breaking waves approaching the shore obliquely.

Understanding of the behaviour of waves as they approach and interact with the coastline is vital for designing effective coastal protection. McGranahan et al. (2007) state that 10 % of the world's population lives in the Low Elevation Coastal Zone, the contiguous area along the coast that is less than 10 m above sea level. Devastating tsunamis in recent decades highlight the vulnerability of many coastal communities that inhabit this zone. The 2004 Indian Ocean tsunami resulted in approximately 280,000 fatalities across 14 different countries[1]. The 2011 Tōhoku earthquake caused a tsunami that penetrated up to 10 km inland in the Sendai area. It resulted in approximately 18,500 deaths and hundreds of billions of dollars of insured losses, as well as causing catastrophic failure at the Fukushima Daiichi Nuclear Power Plant complex. Figure 1.1 shows the enormous reach of the tsunami, which is visualised using wave amplitude contours. The effects propagate as far as New Zealand to the south and the west coast of South America.

Storm waves can also cause enormous loss of life, long-term reduction in health and wellbeing, and damage to infrastructure. The aftermaths of Hurricanes Katrina, Sandy, and most recently, Irma provide well known examples of the damage and casualties that can result from large storm events. Coastal flooding that can result from storms is due to the combined effect of tides, storm surge and waves. Storm surge is a rise in water level due to the combination of strong winds pushing water towards the shore, and low atmospheric pressure. For example, December 2013 and January 2014 saw a succession of winter storms hitting the UK, where storm surge and large waves combined with spring tides to cause coastal flooding in a number of areas[2] (such as Aberystwyth depicted in Figure 1.2). Flooding occurs when coastal defences are breached or overtopped by waves (i.e. when wave run-up exceeds the crest height of the structure). Individual overtopping events may present a risk to pedestrians and the

[1] http://news.bbc.co.uk/2/hi/asia-pacific/4204385.stm

[2] http://www.metoffice.gov.uk/climate/uk/interesting/2013-decwind

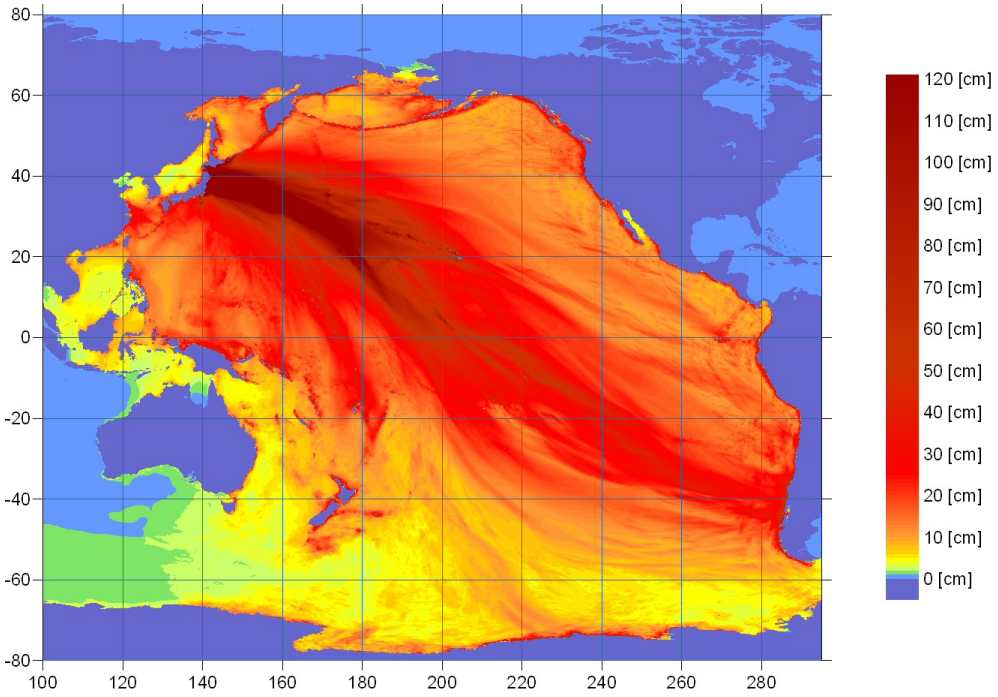

Figure 1.1: Ocean energy distribution map from the 2011 Japan earthquake (NOAA). Image taken from https://upload.wikimedia.org/wikipedia/commons/6/6a/2011Sendai-NOAA-Energylhvpd9-05.jpg (Accessed: August 18th 2017)

occupants of vehicles travelling along the coast.

Figure 1.2: Coastal flooding at Aberystwyth, Wales in January 2014. Photo: Jem Rowland, taken from http://www.walesonline.co.uk/news/wales-news/wales-weather-homes-student-halls-6470889

1.3 Modelling waves in the coastal zone

Coastal engineers need tools to help analyse and predict the complicated hydrodynamic processes that occur at the coast, in order to design effective coastal protection schemes. Numerous strategies exist to model the propagation of waves in the coastal zone, and the associated run-up and overtopping of sea defences. The latter has traditionally been investigated in the laboratory, whereas early run-up experiments were carried out in the field. Both methods are expensive and time-consuming however. Efforts have been made to develop empirical formulae for run-up and overtopping, such as proposed by Hunt (1959) for breaking wave run-up on smooth uniform slopes in relatively deep water. Overtopping is usually calculated using mean discharge rates as opposed to individual overtopping events (see for example van der Meer (1998)). The CLASH project (De Rouck et al. (2009)) used neural networks trained on a database of over 10,000

tests involving irregular waves, to calculate the mean overtopping discharge. van der Meer et al. (2016) combined the results of many research projects including CLASH to create the EurOtop design guide to assist coastal engineers analysing the overtopping of many types of sea defence. Although calculations of sea defence overtopping in terms of mean discharge lead to useful design parameters, such calculations do not provide information on spatial and temporal variations. In practice, the prediction and characterisation of large individual overtopping events is important for determining sea defence failure modes, and assessing the hazard posed to pedestrians and vehicles. In this regard, numerical models have an advantage over design tools based on empirical data. Phase-resolving numerical models based on the nonlinear shallow water equations, the Navier-Stokes equations and the Boussinesq equations have been used by many researchers to model run-up and overtopping as well as wave propagation, and are discussed further below.

1.3.1 Phase-averaged models

Phase-averaged ray-type models are very useful tools for determining the overall nearshore circulation patterns generated by the interaction of waves and currents. Such models are generally constructed as a modified form of the nonlinear shallow water equations, with additional radiation stress gradients after averaging each term in the equations over a wave period (following an analagous approach to Reynolds-averaging in computational fluid dynamics). Radiation stress, a concept introduced by Longuet-Higgins and Stewart (1960), is the mean excess momentum flux induced by waves. Breaking waves cause variations in radiation stress, driving nearshore currents through a pumping effect. Period-averaged models are good predictors of nearshore circulation, as demonstrated by Rogers et al. (2004), who extended an earlier model proposed by Yoo (1986) so that it was solved on an adaptive locally refined grid using a Godonov finite volume scheme. The relative simplicity of period-averaged models means that they are relatively easy to solve numerically, with low computational cost, and can thus be applied to large domains. Their disadvantage lies in the absence of phase information, necessary for predicting run-up, for example.

1.3.2 Mild-slope equations

The mild-slope equations combine the effects of refraction, diffraction, shoaling and reflection, and are applicable in all water depths, assuming a small bed slope. Their classical formulation was first derived by Berkhoff (1972) who integrated the velocity potential for linear waves over the depth, while neglecting the effect of bottom friction and currents. Berkhoff's equations were later extended by other researchers to include the effects of wave-current interaction (see Booij (1981) and Kirby (1984)). The mild-slope equations provide information on the wave amplitude field. The modified mild-slope equations of Radder and Dingemans (1985) form the basis of the linear, phase-resolving MILDwave model developed at Ghent University by Troch (1998). MILDwave is a useful tool for modelling wave propagation at the coast, but is restricted to small amplitude waves in water of slowly varying depth.

1.3.3 Nonlinear shallow water equations

The nonlinear shallow water equations (NSWEs) provide the basis of many numerical models applied to coastal engineering and large-scale flooding problems. The NSWEs can be derived as the depth-integrated form of the Reynolds-averaged continuity and Navier-Stokes equations. The governing equations are parabolic-hyperbolic in form, and behave essentially as advection-diffusion equations. Over the past half century, stable, efficient and robust numerical solvers have been developed, nowadays enhanced by Godunov-type shock-capturing schemes that enable steep-fronted flows to be modelled accurately (examples including bores, dam breaks and coastal inundation). Dodd (1998) applied the NSWEs to random wave run-up and overtopping; however their non-dispersive nature and underlying hydrostatic assumption mean the NSWEs are only applicable to domains containing very shallow water where the velocity can be assumed to be nearly horizontal. Examples of two-dimensional numerical models based on the NSWEs are those of Fraccarollo and Toro (1995), Rogers et al. (2001) and Liang and Borthwick (2009).

1.3.4 Navier Stokes models

Numerical models that solve the three-dimensional continuity and Navier-Stokes equations, and are known as Computational Fluid Dynamics (CFD) models, provide the most accurate means of predicting wave transformation, breaking, run-up and overtopping at the coast. However such models incur very high computational cost, and so are not generally applied to medium/large domains unless significant computing power is available. For example, OpenFOAM is an open source CFD modelling system that can simulate unsteady flows using the continuity and Navier-Stokes equations. When applying the Navier-Stokes equations to flows in the swash zone, it is commonplace for certain simplifications to be adopted to ease the computational burden. Examples of simplified models include the Reynolds-Averaged Navies Stokes equations (RANS) (e.g. Lin and Liu (1998)) and Large-Eddy Simulation (LES) (see Zhou et al. (2014)). An alternative to the Eulerian mesh-based methods for solving the Navier-Stokes equations, is the Lagrangian, particle-based approach of Smoothed Particle Hydrodynamics (SPH), first applied to fluids by Monaghan (1994) and subsequently advanced by many other researchers, including Dalrymple and Rogers (2006) and Altomare et al. (2014). In SPH methods, the fluid mass is discretised into constituent particles with associated physical quantities. An advantage of these types of models is their natural capability to deal with complex interactions such as wave breaking and overtopping.

1.3.5 Boussinesq-type models

The Boussinesq equations (originally formulated by Boussinesq (1872)) represent a depth-averaged approximation of the Navier-Stokes equations that fully describe three-dimensional flow. They are more advanced than the shallow water equations in that they retain the influence of vertical accelerations and hydrodynamic pressure. Application of the Boussinesq equations to the solution of coastal engineering problems became possible with the advent of the computer, and was spearheaded by Peregrine (1967), whose equations are nowadays referred to as the classical Boussinesq equations. Over the past 50 years, Boussinesq-type models have become increasingly popular amongst coastal engineers, due to the ability of the Boussinesq equations to represent adequately

the main physical processes at the shore, while remaining relatively computationally efficient, compared to Navier-Stokes CFD solvers.

Early Boussinesq models that developed as a result of Peregrine's work were limited to modelling very long waves, because of the weakly nonlinear, weakly dispersive nature of the governing equations, i.e. $O(\mu^2) = O(\epsilon) << 1$, where the dispersion parameter μ is the ratio of water depth to wavelength and the nonlinearity parameter ϵ is the ratio of the wave amplitude to water depth. The early models were used to simulate seiching, and hence predict ship motions and mooring forces in harbours (e.g. Lepelletier and Raichlen (1987)); this application of Boussinesq-type models remains valid today. The need for accurate models of shorter waves in the coastal zone, led to a concerted effort in the 1990s to improve the dispersion characteristics of the classical Boussinesq equations. While simply including contributions to the governing equations at a higher order than $O(\mu^2)$ would achieve an improvement in the dispersion properties of the equations, it would also lead to higher-order derivatives than the third-order derivatives that occur in the classical Boussinesq equations and hence would be increasingly difficult to solve. To overcome this limitation, Madsen and Sørensen (1992) applied a linear operator to the momentum equation that resulted in higher-order dispersive contributions, while maintaining only third-order derivatives. This led to an equation set valid for relative water depth up to $\mu = 0.5$. Nwogu (1993) also achieved improved dispersion characteristics without increasing the order of the governing equations by formulating the equations in terms of a chosen reference velocity (evaluated at a specific depth) rather than a depth-averaged velocity.

While the foregoing research led to equations with improved dispersion characteristics, the resulting models were still restricted to weakly nonlinear interactions. Amongst others, Wei et al. (1995), Madsen and Schäffer (1998), and Gobbi et al. (2000) further extended the validity of Boussinesq-type equations by developing fully nonlinear models where $O(\epsilon) = 1$. Agnon et al. (1999) were the first to achieve the same accuracy in nonlinear properties as in dispersion properties. The model was further enhanced by Madsen et al. (2003) who achieved a more accurate vertical velocity profile for a mildly sloping bed. The later model of Madsen et al. (2006) is valid for both fully nonlinear

and highly dispersive waves propagating over a rapidly changing bathymetry.

As most Boussinesq-type models are based on the assumption of irrotational flow, they cannot model wave breaking, and must be modified to account for the associated energy dissipation. The main approaches to this are the surface roller model and the eddy-viscosity model. The surface roller concept, stemming from the work of Svendsen (1984), forms the basis of models proposed by Schäffer et al. (1993) and Madsen et al. (1997). The surface roller concept is also implemented in MIKE21, the commercial wave modelling tool developed by the Danish Hydraulic Institute (DHI) (Madsen and Sørensen (1992) and Schäffer et al. (1993)). The eddy-viscosity approach to wave breaking introduces a diffusive-type term in the momentum equation and has been implemented in one-dimension by Karambas and Koutitas (1992) and in two-dimensions by Chen et al. (2000). An alternative approach is to use a hybrid model based on Boussinesq-type equations pre-breaking and the nonlinear shallow water equations post-breaking. A very similar approach is adopted in the present research study, and builds on previous research of Borthwick et al. (2006), Orszaghova (2011), and Orszaghova et al. (2012). Hybrid Boussinesq-NSWE numerical models have also been proposed by Tonelli and Petti (2009), Tonelli and Petti (2012), Shi et al. (2012), and McCabe et al. (2013).

Before computer technology advanced to a stage where Boussinesq modelling of the surf-zone became possible, most models of wave-induced circulation in the nearshore zone were based on period-averaged, depth-integrated conservation laws of mass and momentum. Early work on modelling wave-current interaction using Boussinesq-type equations was carried out by Yoon and Liu (1989). Chen et al. (2000) developed a two-dimensional model of wave-induced nearshore circulation based on the fully nonlinear Boussinesq equations and achieved satisfactory results for waves breaking over a rapidly changing bathymetry. Chen et al. (1999) applied the model to a rip current system. The most sophisticated Boussinesq models used to simulate wave-induced currents and wave-current interactions are those based on the fully nonlinear equations, e.g. Chen et al. (2003).

Efforts have also been made to develop models that give a more accurate description

of the vertical flow structure, by incorporating a number of vertical layers (see Lynett and Liu (2004)). This approach, being more three-dimensional in nature, has led to improvements in the nonlinear-dispersive properties, while limiting the highest order derivatives to third order, but is more reliant on significant computational power.

1.4 Aims and objectives

The one-dimensional hybrid numerical solver developed by Orszaghova (2011) has proved to be a computationally efficient and accurate tool for modelling nearshore wave propagation, run-up and overtopping (Orszaghova et al. (2012), Fitzgerald et al. (2016)). The present thesis aims to extend Orszaghova's solver to two horizontal dimensions (2DH) and investigate its ability to model more complicated wave-wave and wave-shoreline interactions, in particular those interactions that lead to wave-induced nearshore currents and multi-directional wave focusing in the coastal zone. It is therefore proposed to develop a 2DH model, that solves the enhanced Boussinesq equation set of Madsen and Sørensen (1992) pre-breaking and the nonlinear shallow water equations post-breaking. Although the Madsen and Sørensen equations are relatively simple in comparison with the more sophisticated, higher-order Boussinesq equation sets, simplicity is a key consideration for the development of a numerical model that does not necessarily require high-performance computing resources to be a useful tool to the coastal engineer. Waves in the model are generated by a system of independently moving piston-type paddles. A domain transformation is applied in the region of the paddles, and the governing equations are solved on the transformed, fixed domain, to overcome the problem of a time-varying domain when the paddles are in motion. The wave generation mechanism enables full replication of laboratory experiments, including the generation of multi-directional seas and their interaction with shorelines of different configurations. The ultimate aim is to develop a model that will be able to quantify run-up and overtopping events caused by both long and short-crested seas. By including gridded water depth and flow data behind sea defences, the model could ultimately be used to determine the risk posed to people and property, and the resulting damage caused.

Thus the objectives of this research are summarised as follows:

- To develop a two-horizontal-dimensional (2DH) numerical model based on Boussinesq-type equations and the nonlinear shallow water equations that is capable of replicating the hydrodynamics of coastal laboratory wave basins, including the interaction of multi-directional sea states with shorelines of different configurations.
- To verify the numerical model using standard benchmark tests, including the sloshing of a Gaussian hump of water in a frictionless rectangular tank, sloshing in a parabolic basin with bed frection, the interaction of a dam break wave with three bed obstacles, and the propagation of a solitary wave in a rectangular domain.
- To apply the numerical model to reproduce and interpret the results of laboratory tests carried out at the UK Coastal Research Facility (UKCRF) involving nearshore circulation at a multi-cusped beach, and the interaction of focused wave groups with a plane beach.

1.5 Thesis outline

Chapter 2 outlines the mathematical theory behind this research, including derivation of the governing equations that form the mathematical basis of the numerical model. **Chapter 3** presents full details of the numerical solver, including wave generation, solution of the governing equations for prescribed initial and boundary conditions, the switching mechanism between Boussinesq and NSWE equations triggered by wave breaking, and the wetting and drying algorithm. **Chapter 4** presents results from a series of benchmark tests, selected to verify different aspects of the model. The propagation of a symmetrical wave in a closed, square basin is used to confirm the accuracy of the Boussinesq solver, including the correct handling of the cross-derivative terms. Harmonic analysis of the free-surface motions is used to create a template for similar analysis of focused wave groups, described in Chapter 6. The finite volume solver and wetting and drying algorithm are verified using the test cases of sloshing in a parabolic basin,

and the propagation of a dam break wave. A semi-analytical solution for a solitary wave is used to verify the correct implementation of the piston paddles, as well as confirming the conservation properties of the model. **Chapter 5** presents results from simulations involving nearly horizontal wave-induced currents that form nearshore circulation patterns. Regular waves interacting with sinusoidal and cuspate beaches are considered. The results are compared with data from laboratory experiments conducted previously at the University of Liverpool in the early 1980s and in the U.K. Coastal Research Facility in the mid-1990s. **Chapter 6** presents simulations of focused wave groups as they interact with a plane beach, and the predictions compared against laboratory measurements acquired at the UKCRF in the early 2000s. The harmonic structure of multi-directional focused wave groups is interpreted. **Chapter 7** discusses the main findings, summarises the conclusions, and makes recommendations for further research.

Acknowledgements

The author would like to acknowledge the UK Engineering and Physical Sciences Research Council (EPSRC) and HR Wallingford Ltd for their co-sponsorship of the U.K. Coastal Research Facility (UKCRF).

The multi-cusped beach tests at the UKCRF were funded through EPSRC grant GR/K04125 held at the University of Oxford; Yolanda Foote assisted in the measurements and image processing.

The focused wave tests at the UKCRF were carried out as a joint research project between the Universities of Manchester and Oxford. Alison Hunt and Tong Feng assisted in carrying out the data measurements in the UKCRF, funded through EPSRC grants GR/N21741, GR/N22595, and GR/R05369.

Chapter 2

Mathematical theory

In this chapter, the classical Boussinesq equations are first derived, and the manipulations that lead to the enhanced equations of Madsen and Sørensen (1992) are then described. The nonlinear shallow water equations are also introduced and both equation sets reformulated in terms of stage and discharge $(\eta, \mathbf{Q})$. The theory behind generating waves using paddles is also described.

2.1 Classical Boussinesq equations

The Boussinesq equations essentially reduce the mathematical description of three-dimensional flow to two dimensions by eliminating the vertical coordinate, while retaining the effect of the vertical acceleration. There are a number of ways of achieving this result: the approach followed by Peregrine (1967) among others, uses the continuity and Euler equations and involves perturbation expansions of the surface elevation and velocity components and integration of the vertical Euler equation. Madsen and Schäffer (1999) commence with a power series expansion of the velocity potential in the vertical coordinate, which is then substituted into the Laplace equation. This latter approach is followed here. Two important parameters that are associated with Boussinesq-type equations are the nonlinearity parameter, ϵ, the ratio of amplitude to depth, and the dispersion parameter, μ, the ratio of depth to wave length. The classical Boussinesq equations are valid for weak dispersion and weak nonlinearity, and it is

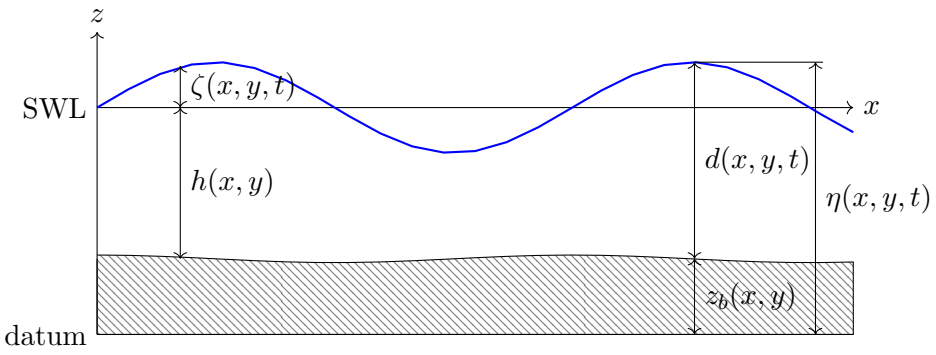

Figure 2.1: Definition sketch

assumed that ϵ and μ^2 are of the same order.

The derivation of Boussinesq-type equations is now explained, following Madsen and Schäffer (1999). It is assumed that the fluid is incompressible and inviscid and that the flow is irrotational. A Cartesian coordinate system is used with the $x-$ and y-axes located at the still water level and the z-axis pointing vertically upwards, as illustrated in Figure 2.1. The fluid domain is bounded by the sea bed at $z = -h(x, y)$ and the free surface, $z = \zeta(x, y, t)$.

The Laplace equation, and bed and free-surface boundary conditions are given by

$$\Phi_{zz} + \nabla^2\Phi = 0 \qquad -h < z < \zeta, \tag{2.1a}$$

$$\Phi_z + \nabla h \cdot \nabla\Phi = 0 \qquad z = -h, \tag{2.1b}$$

$$\Phi_t + g\zeta + \frac{1}{2}\left((\nabla\Phi)^2 + (\Phi_z)^2\right) = 0 \qquad z = \zeta, \tag{2.1c}$$

$$-\Phi_z + \zeta_t + \nabla\zeta \cdot \nabla\Phi = 0 \qquad z = \zeta, \tag{2.1d}$$

where Φ is the velocity potential, h is the still water depth, ζ is the free-surface elevation above the still water level, g is the acceleration due to gravity and t is time. ∇ is the two-dimensional gradient operator $(\partial/\partial x, \partial/\partial y)$, and the z and t subscripts represent $\partial/\partial z$ and $\partial/\partial t$ respectively.

Non-dimensional variables are used in the derivation, given as follows:

$$x' = \frac{x}{l_0}, \quad y' = \frac{y}{l_0}, \quad z' = \frac{z}{h_0}, \quad t' = \frac{\sqrt{gh_0}}{l_0}t, \quad h' = \frac{h}{h_0}, \quad \zeta' = \frac{\zeta}{a_0}, \quad \Phi' = \frac{h_0}{a_0 l_0 \sqrt{gh_0}}\Phi \tag{2.2}$$

where the primes denote non-dimensional quantities and h_0, l_0 and a_0 represent a typical water depth, wavelength and wave amplitude. The velocity components are related to the velocity potential by

$$\mathbf{u} = \nabla\Phi, \quad w = \Phi_z \tag{2.3}$$

where $\mathbf{u} = (u, v)$ is the vector of horizontal velocity components.

The Laplace equation and associated boundary conditions in non-dimensional form for the fully dispersive and fully nonlinear irrotational wave problem are given as follows, with the primes omitted for convenience:

$$\Phi_{zz} + \mu^2\nabla^2\Phi = 0 \qquad -h < z < \epsilon, \zeta \tag{2.4a}$$

$$\frac{1}{\mu^2}\Phi_z + \nabla h \cdot \nabla\Phi = 0 \qquad z = -h, \tag{2.4b}$$

$$\Phi_t + \zeta + \frac{\epsilon}{2}\left((\nabla\Phi)^2 + \frac{1}{\mu^2}(\Phi_z)^2\right) = 0 \qquad z = \epsilon\zeta, \tag{2.4c}$$

$$-\frac{1}{\mu^2}\Phi_z + \zeta_t + \epsilon\nabla\zeta \cdot \nabla\Phi = 0 \qquad z = \epsilon\zeta. \tag{2.4d}$$

The nonlinearity parameter is $\epsilon = a_0/h_0$ and the dispersion parameter is $\mu = h_0/l_0$.

Expressing the velocity potential as a power series in the vertical direction, using the expansion

$$\Phi(x, y, z, t) = \sum_{n=0}^{\infty} z^n \Phi^n(x, y, t), \tag{2.5}$$

and inserting into (2.4a), leads to the recurrence relation

$$\Phi^{n+2} = -\mu^2 \frac{\nabla^2\Phi^{(n)}}{(n+1)(n+2)}, \quad n = 1, 2, 3, \ldots \tag{2.6}$$

By combining (2.5) with (2.6), it is possible to obtain a general expression for the velocity potential given by

$$\Phi(x, y, z, t) = \sum_{n=0}^{\infty}(-1)^n \left(\frac{z^{2n}}{(2n)!}\mu^{2n}\nabla^{2n}\hat{\Phi} + \frac{z^{2n+1}}{(2n+1)!}\mu^{2n+2}\nabla^{2n}\hat{w}\right). \tag{2.7}$$

Substituting (2.7) into (2.3) the following expressions are obtained for the velocity field

$$\mathbf{u}(x, y, z, t) = \sum_{n=0}^{\infty}(-1)^n \left(\frac{z^{2n}}{(2n)!}\mu^{2n}\nabla(\nabla^{2n-2}(\nabla \cdot \hat{\mathbf{u}})) + \frac{z^{2n+1}}{(2n+1)!}\mu^{2n+2}\nabla(\nabla^{2n}\hat{w})\right) \tag{2.8a}$$

and

$$w(x,y,z,t) = \sum_{n=0}^{\infty}(-1)^n \left(-\frac{z^{2n+1}}{(2n)!}\mu^{2n+2}\nabla^{2n}(\nabla\cdot\hat{\mathbf{u}}) + \frac{z^{2n}}{(2n)!}\mu^{2n+2}\nabla^{2n}\hat{w} \right) \tag{2.8b}$$

where

$$\begin{aligned} &\hat{\Phi} \equiv \Phi(x,y,0,t), \quad \hat{\mathbf{u}} \equiv \nabla\hat{\Phi} \equiv \mathbf{u}(x,y,0,t), \quad \text{and} \\ &\hat{w} \equiv \frac{1}{\mu^2}\Phi_z(x,y,0,t) = \frac{1}{\mu^2}w(x,y,0,t). \end{aligned} \tag{2.9}$$

Equations (2.7) and (2.8) define the wave kinematics in terms of the velocity components at the still water level.

Application of the kinematic boundary condition at the sea bed establishes the relationship between the horizontal and vertical velocity components. Inserting (2.7) into (2.4b) and using (2.9), the relationship between the horizontal and vertical velocity components is established as

$$\hat{w} + \sum_{n=0}^{\infty}(-1)^n\mu^{2n}\nabla\cdot\left(\frac{h^{2n+1}}{(2n+1)!}(\nabla(\nabla^{2n-2}(\nabla\cdot\hat{\mathbf{u}}))) - \mu^2\frac{h^{2n+2}}{(2n+2)!}\nabla(\nabla^{2n}\hat{w}) \right) = 0. \tag{2.10}$$

The relationship between $\hat{w}$ and $\hat{\mathbf{u}}$ given in (2.10) is of infinite order μ and is exact for any bottom slope. For the general case of a spatially varying water depth, Madsen and Schäffer (1998) assume $\mu << 1$ and use the expansion

$$\hat{w}(x,y,t) = \sum_{m=0}^{\infty}\mu^{2m}w^{(m)}(x,y,t) \tag{2.11}$$

to derive the following explicit recursive expression for $w^{(p)}$ at the order $O(\mu^{2p})$:

$$\begin{aligned} w^{(p)} =& \frac{(-1)^{p+1}}{(2p+1)!}\nabla\cdot(h^{2p+1}\nabla(\nabla^{2p-2}(\nabla\cdot\hat{\mathbf{u}}))) \\ &+ \sum_{n=0}^{p-1}\frac{(-1)^n}{(2n+2)!}\nabla\cdot(h^{2n+2}\nabla(\nabla^{2n}w^{(p-n-1)})). \end{aligned} \tag{2.12}$$

Equations (2.11) and (2.12) can be used to express $\hat{w}$ in terms of $\hat{\mathbf{u}}$ for any order in μ, which for order $O(\mu^2)$ is given by

$$\hat{w}(x,y,t) = -\nabla\cdot(h\hat{\mathbf{u}}) + \mu^2\nabla\cdot\left(\frac{h^3}{6}\nabla(\nabla\cdot\hat{\mathbf{u}}) - \frac{h^2}{2}\nabla(\nabla\cdot(h\hat{\mathbf{u}})) \right) + O(\mu^4). \tag{2.13}$$

Equation (2.13), in conjunction with (2.8a) and (2.8b), describe the wave kinematics in terms of derivatives of $\hat{\mathbf{u}}$.

The formulations above relate to the wave kinematics in the fluid interior, and only involve the linear dispersion parameter, μ. The free-surface boundary conditions are now considered. These are responsible for the nonlinearity of the system. Equation (2.4d), the kinematic free-surface condition, can be written

$$\zeta_t - \tilde{w} + \epsilon \nabla\zeta \cdot \tilde{\mathbf{u}} = 0 \tag{2.14}$$

where the horizontal and vertical velocity components at the free surface ($z = \epsilon\zeta$) are given by

$$\tilde{\mathbf{u}} \equiv (\nabla\Phi)_{z=\epsilon\zeta}, \quad \tilde{w} \equiv \frac{1}{\mu^2}(\Phi_z)_{z=\epsilon\zeta}. \tag{2.15}$$

Using (2.8a) and (2.8b), $\tilde{\mathbf{u}}$ and $\tilde{w}$ at the surface can be related to $\hat{\mathbf{u}}$ and $\hat{w}$ at the still water level as follows:

$$\tilde{\mathbf{u}} = \sum_{n=0}^{\infty}(-1)^n \left(\epsilon^{2n}\mu^{2n}\frac{\zeta^{2n}}{(2n)!}\nabla(\nabla^{2n-2}(\nabla\cdot\hat{\mathbf{u}})) + \epsilon^{2n+1}\mu^{2n+2}\frac{\zeta^{2n+1}}{(2n+1)!}\nabla(\nabla^{2n}\hat{w}) \right) \tag{2.16a}$$

and

$$\tilde{w} = \sum_{n=0}^{\infty}(-1)^n \left(-\epsilon^{2n+1}\mu^{2n}\frac{\zeta^{2n+1}}{(2n+1)!}\nabla^{2n}(\nabla\cdot\hat{\mathbf{u}}) + \epsilon^{2n}\mu^{2n}\frac{\zeta^{2n}}{(2n)!}\nabla^{2n}\hat{w} \right). \tag{2.16b}$$

Substituting (2.16a) and (2.16b) into the kinematic free-surface boundary condition (2.14) gives

$$\begin{aligned} \zeta_t - \hat{w} + \sum_{n=0}^{\infty}(-1)^n\epsilon^{2n+1}\mu^{2n}\nabla\cdot\Bigg(& \frac{\zeta^{2n+1}}{(2n+1)!}\nabla(\nabla^{2n-2}(\nabla\cdot\hat{\mathbf{u}})) \\ & + \epsilon\mu^2\frac{\zeta^{2n+2}}{(2n+2)!}\nabla(\nabla^{2n}\hat{w})\Bigg) = 0, \end{aligned} \tag{2.17}$$

which is an exact representation of the kinematic free-surface boundary condition expressed in terms of $\hat{\mathbf{u}}$ and $\hat{w}$.

An alternative to the kinematic free-surface condition is the depth-integrated continuity equation defined by

$$\zeta_t + \nabla\cdot\mathbf{Q} = 0, \qquad \mathbf{Q} \equiv \int_{-h}^{\epsilon\zeta}\mathbf{u}\mathrm{d}z, \tag{2.18}$$

where $\mathbf{Q} = (q_x, q_y)$ is the vector of horizontal fluxes. Vertical integration of (2.8a) gives the following expression for $\mathbf{Q}$ in terms of $\hat{\mathbf{u}}$ and $\hat{w}$:

$$\begin{aligned}\mathbf{Q} = \sum_{n=0}^{\infty}(-1)^n \Bigg(& \mu^{2n}\frac{(\epsilon^{2n+1}\zeta^{2n+1} + h^{2n+1})}{(2n+1)!}\nabla(\nabla^{2n-2}(\nabla\cdot\hat{\mathbf{u}})) \\ & + \mu^{2n+2}\frac{(\epsilon^{2n+2}\mu^{2n+2} - h^{2n+2})}{(2n+2)!}\nabla(\nabla^{2n}\hat{w})\Bigg).\end{aligned} \tag{2.19}$$

The final boundary condition to be satisfied is the dynamic free-surface boundary condition (2.4c). Applying the gradient operator to this boundary condition leads to

$$\begin{aligned}&\sum_{n=0}^{\infty}(-1)^n\nabla\left(\epsilon^{2n}\mu^{2n}\frac{\zeta^{2n}}{(2n!)}\nabla^{2n-2}(\nabla\cdot\hat{\mathbf{u}}_t) + \epsilon^{2n+1}\mu^{2n+2}\frac{\zeta^{2n+1}}{(2n+1)!}\nabla^{2n}\hat{w}_t\right) \\ &+ \nabla\zeta + \nabla\left(\epsilon\frac{\tilde{\mathbf{u}}\cdot\tilde{\mathbf{u}}}{2} + \epsilon\mu^2\frac{\tilde{w}^2}{2}\right) = 0.\end{aligned} \tag{2.20}$$

Using (2.16a) and (2.16b), equations (2.17) and (2.20) can be expressed in terms of $\zeta, \hat{\mathbf{u}}$ and $\hat{w}$. $\hat{w}$ can then be eliminated by use of (2.11) and (2.12) to obtain a system of equations in terms of ζ and $\hat{\mathbf{u}}$, given by

$$\zeta_t + \nabla\cdot(\hat{\mathbf{u}}(h+\epsilon\zeta)) + \mu^2\Gamma_2^I = O(\mu^4) \tag{2.21a}$$

and

$$\hat{\mathbf{u}}_t + \nabla\zeta + \epsilon\hat{\mathbf{u}}\cdot\nabla\hat{\mathbf{u}} + \mu^2\Gamma_2^{II} = O(\mu^2), \tag{2.21b}$$

where the order of magnitude of the dispersive terms is

$$\Gamma_2^I = O(1, \epsilon^2, \epsilon^3); \quad \Gamma_2^{II} = O(\epsilon, \epsilon^2, \epsilon^3). \tag{2.22}$$

To express the momentum equation in terms of the depth-integrated flux $\mathbf{Q}$, we first obtain an expression for the depth-integrated velocity $\mathbf{U}$ in terms of $\hat{\mathbf{u}}$, where

$$\mathbf{U} \equiv \frac{1}{h+\epsilon\zeta}\int_{-h}^{\epsilon\zeta}\mathbf{u}\ \mathrm{dz} = \frac{\mathbf{Q}}{(h+\epsilon\zeta)}. \tag{2.23}$$

This is achieved by substituting (2.13) into (2.19) and inserting the result into (2.23). This relation is then inverted so that $\hat{\mathbf{u}}$ is expressed in terms of $\mathbf{U}$, by using successive substitutions at lowest order in μ^2. $\hat{\mathbf{u}}$ can then be eliminated from the momentum

equation (2.21b) and replaced by functions of $\mathbf{U}$. The resulting momentum vector equation is given by

$$\frac{\partial \mathbf{U}}{\partial t} + \nabla\zeta + \epsilon \mathbf{U}\cdot\nabla\mathbf{U} + \mu^2 h \frac{\partial}{\partial t}\left(\frac{1}{6}h\nabla(\nabla\cdot\mathbf{U}) - \frac{1}{2}\nabla(\nabla\cdot(h\mathbf{U}))\right) = O(\mu^4). \tag{2.24}$$

Using (2.23) and neglecting terms of order μ^4 and higher, (2.24) can be formulated in terms of the depth averaged flux, giving

$$\begin{aligned}\frac{\partial \mathbf{Q}}{\partial t} + (h+\epsilon\zeta)\nabla\zeta + \epsilon\nabla\left(\frac{\mathbf{Q}^2}{h+\epsilon\zeta}\right) + \mu^2\frac{dh^2}{6}\frac{\partial}{\partial t}\left(\nabla\left(\nabla\cdot\left(\frac{\mathbf{Q}}{d}\right)\right)\right) \\ - \mu^2\frac{dh}{2}\frac{\partial}{\partial t}\nabla(\nabla\cdot\left(\frac{h\mathbf{Q}}{d}\right) = O(\mu^4).\end{aligned} \tag{2.25}$$

As $d \equiv h + \epsilon\zeta$, equation (2.25) contains higher order nonlinear effects and can be simplified to $O(\epsilon, \mu^2)$, to give

$$\begin{aligned}\frac{\partial \mathbf{Q}}{\partial t} + d\nabla\zeta + \epsilon\nabla\left(\frac{\mathbf{Q}^2}{d}\right) + \mu^2\frac{h^3}{6}\frac{\partial}{\partial t}\left(\nabla\left(\nabla\cdot\left(\frac{\mathbf{Q}}{h}\right)\right)\right) \\ - \mu^2\frac{h^2}{2}\frac{\partial}{\partial t}\nabla(\nabla\cdot\mathbf{Q}) = O(\epsilon^2, \epsilon\mu^2, \mu^4).\end{aligned} \tag{2.26}$$

Converting (2.18) and (2.26) back into dimensional variables, noting that $\mathbf{Q}' = \frac{1}{a_0\sqrt{gh_0}}\mathbf{Q}$, leads to

$$\frac{\partial \zeta}{\partial t} + \nabla\cdot\mathbf{Q} = 0, \tag{2.27a}$$

$$\frac{\partial \mathbf{Q}}{\partial t} + gd\nabla\zeta + \nabla\left(\frac{\mathbf{Q}^2}{h}\right) = \mathbf{\Psi} \tag{2.27b}$$

where

$$\mathbf{\Psi} = -\frac{h^3}{6}\frac{\partial}{\partial t}\left(\nabla\left(\nabla\cdot\left(\frac{\mathbf{Q}}{h}\right)\right)\right) + \frac{h^2}{2}\frac{\partial}{\partial t}\nabla(\nabla\cdot\mathbf{Q}). \tag{2.28}$$

(2.27) and (2.28) are the classical Boussinesq equations of order $O(\epsilon, \mu^2)$ formulated in terms of $(\zeta, \mathbf{Q})$. (2.28) represents the dispersive terms which are expressed in terms of the still water depth, h, and thus neglect the nonlinear effects arising from the difference between the total water depth d, and h.

2.2 Enhanced Boussinesq equations

Boussinesq-type equations are limited in the range of water depths in which they can be applied. Depending on the form of the coefficients for the dispersive terms in (2.27b),

the classical equations apply for depth to deep-water wavelength ratios (h/L_0) in the range from 0.12 to approximately 0.22 ($kh \approx 1.38$), at which the error in the celerity is 5%. Madsen and Sørensen (1992) present a new form of the Boussinesq equations that extends their range of applicability offshore. Assuming that first derivatives of h are small, and neglecting higher order derivatives and products of derivatives, the dispersive terms, i.e. (2.28), where $\mathbf{\Psi} = (\Psi_1, \Psi_2)$, can be simplified to

$$\Psi_1 = \frac{h^2}{3}\left(\frac{\partial^3 q_x}{\partial x^2 \partial t} + \frac{\partial^3 q_y}{\partial x \partial y \partial t}\right) + \frac{h}{6}\frac{\partial h}{\partial y}\frac{\partial^2 q_y}{\partial x \partial t} + \frac{h}{6}\frac{\partial h}{\partial x}\left(2\frac{\partial^2 q_x}{\partial x \partial t} + \frac{\partial^2 q_y}{\partial y \partial t}\right) \tag{2.29a}$$

and

$$\Psi_2 = \frac{h^2}{3}\left(\frac{\partial^3 q_y}{\partial y^2 \partial t} + \frac{\partial^3 q_x}{\partial x \partial y \partial t}\right) + \frac{h}{6}\frac{\partial h}{\partial x}\frac{\partial^2 q_x}{\partial y \partial t} + \frac{h}{6}\frac{\partial h}{\partial y}\left(2\frac{\partial^2 q_y}{\partial y \partial t} + \frac{\partial^2 q_x}{\partial x \partial t}\right). \tag{2.29b}$$

Using the linear long wave approximations,

$$\frac{\partial q_x}{\partial t} + gh\frac{\partial \zeta}{\partial x} \approx 0, \quad \frac{\partial q_y}{\partial t} + gh\frac{\partial \zeta}{\partial y} \approx 0, \tag{2.30}$$

and applying spatial differentiation, leads to

$$\frac{\partial^3 q_x}{\partial x^2 \partial t} + 2g\frac{\partial h}{\partial x}\frac{\partial^2 \zeta}{\partial x^2} + gh\frac{\partial^3 \zeta}{\partial x^3} \approx 0, \tag{2.31a}$$

$$\frac{\partial^3 q_x}{\partial x \partial y \partial t} + g\frac{\partial h}{\partial x}\frac{\partial^2 \zeta}{\partial x \partial y} + g\frac{\partial h}{\partial y}\frac{\partial^2 \zeta}{\partial x^2} + gh\frac{\partial^3 \zeta}{\partial x^2 \partial y} \approx 0, \tag{2.31b}$$

$$\frac{\partial^3 q_y}{\partial y^2 \partial t} + 2g\frac{\partial h}{\partial y}\frac{\partial^2 \zeta}{\partial y^2} + gh\frac{\partial^3 \zeta}{\partial y^3} \approx 0, \tag{2.31c}$$

and

$$\frac{\partial^3 q_y}{\partial x \partial y \partial t} + g\frac{\partial h}{\partial y}\frac{\partial^2 \zeta}{\partial x \partial y} + g\frac{\partial h}{\partial x}\frac{\partial^2 \zeta}{\partial y^2} + gh\frac{\partial^3 \zeta}{\partial x \partial y^2} \approx 0. \tag{2.31d}$$

Premultiplying (2.31) by Bh^2 and adding (2.31a) and (2.31d) to (2.29a), and (2.31b) and (2.31c) to (2.29b) leads to

$$\begin{aligned}\Psi_1 = &\left(B + \frac{1}{3}\right)h^2\left(\frac{\partial^3 q_x}{\partial x^2 \partial t} + \frac{\partial^3 q_y}{\partial x \partial y \partial t}\right) + Bgh^3\left(\frac{\partial^3 \zeta}{\partial x^3} + \frac{\partial^3 \zeta}{\partial x \partial y^2}\right) \\ &+ h\frac{\partial h}{\partial x}\left(\frac{1}{3}\frac{\partial^2 q_x}{\partial x \partial t} + \frac{1}{6}\frac{\partial^2 q_y}{\partial y \partial t} + 2Bgh\frac{\partial^2 \zeta}{\partial x^2} + Bgh\frac{\partial^2 \zeta}{\partial y^2}\right)\end{aligned}$$

$$+ h\frac{\partial h}{\partial y}\left(\frac{1}{6}\frac{\partial^2 q_y}{\partial x \partial t} + Bgh\frac{\partial^2 \zeta}{\partial x \partial y}\right) \tag{2.32a}$$

and

$$\begin{aligned}\Psi_2 = &\left(B + \frac{1}{3}\right) h^2 \left(\frac{\partial^3 q_y}{\partial y^2 \partial t} + \frac{\partial^3 q_x}{\partial x \partial y \partial t}\right) + Bgh^3 \left(\frac{\partial^3 \zeta}{\partial y^3} + \frac{\partial^3 \zeta}{\partial x^2 \partial y}\right) \\ &+ h\frac{\partial h}{\partial y}\left(\frac{1}{3}\frac{\partial^2 q_y}{\partial y \partial t} + \frac{1}{6}\frac{\partial^2 q_x}{\partial x \partial t} + 2Bgh\frac{\partial^2 \zeta}{\partial y^2} + Bgh\frac{\partial^2 \zeta}{\partial x^2}\right) \\ &+ h\frac{\partial h}{\partial x}\left(\frac{1}{6}\frac{\partial^2 q_x}{\partial y \partial t} + Bgh\frac{\partial^2 \zeta}{\partial x \partial y}\right).\end{aligned} \tag{2.32b}$$

Equations (2.32a) and (2.32b), together with (2.27) represent the enhanced Boussinesq equation set, where B is the Boussinesq dispersion coefficient and the added terms are $O(\mu^2)$. By setting $B = 0$, (2.29) is recovered.

To verify the enhancement technique, the linearised one-dimensional version of (2.27) combined with (2.32) is considered. Denoting the one-dimensional flux as q, this reads as

$$\frac{\partial \zeta}{\partial t} + \frac{\partial q}{\partial x} = 0 \tag{2.33a}$$

and

$$\frac{\partial q}{\partial t} + gd\frac{\partial \zeta}{\partial x} + \frac{\partial}{\partial x}\left(\frac{q^2}{d}\right) = Bgh^3\frac{\partial^3 \zeta}{\partial x^3} + \left(B + \frac{1}{3}\right) h^2 \frac{\partial^3 q}{\partial x^2 \partial t} + \frac{\partial h}{\partial x}\left(2Bgh^2\frac{\partial^2 \zeta}{\partial x^2} + \frac{h}{3}\frac{\partial^2 q}{\partial x \partial t}\right) \tag{2.33b}$$

The wave equation for this system can be derived by using (2.33a) with (2.33b) to obtain a single higher order equation in ζ and substituting in solutions of the form $\zeta(x,t) = A(x)\mathrm{e}^{i(\omega t - \phi(x))}$ where A is the local wave amplitude, ω is the angular frequency, and ϕ is a phase function related to the local wave number by $\phi_x = k(x)$. Neglecting all x-derivatives of h, k, and A, the following embedded linear dispersion relation is obtained:

$$-\omega^2 + ghk^2 + Bgh^3k^4 - \left(B + \tfrac{1}{3}\right) k^2 h^2 \omega^2 = 0, \tag{2.34}$$

which can be written

$$\frac{c^2}{gh} = \frac{1 + Bk^2h^2}{1 + (B + \frac{1}{3})k^2h^2}, \tag{2.35}$$

where $c = \omega/k$ is the wave celerity. The exact linear dispersion relation (see Dean and Dalrymple (1991) for example) is given by

$$\frac{c^2}{gh} = \frac{\tanh kh}{kh}. \tag{2.36}$$

A Padé expansion of order [m][n] can be used to obtain an approximation of a function by expanding the function as a ratio of two power series. Applying an order [2][2] Padé expansion to (2.36) gives

$$[2][2]\frac{c^2}{gh} = \frac{1 + \frac{1}{15}(kh)^2}{1 + \frac{2}{5}(kh)^2} + O(\mu^6). \tag{2.37}$$

Thus by choosing $B = \frac{1}{15}$, (2.35) becomes (2.37). As (2.37) is $O(\mu^4)$, the enhancement procedure has doubled the accuracy of the linear dispersion of the classical Boussinesq equations.

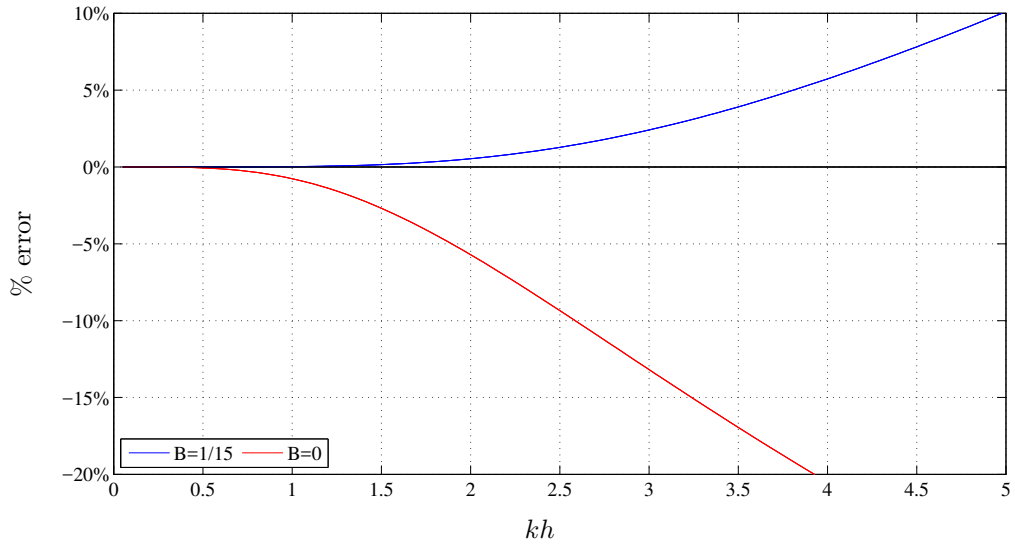

Figure 2.2: Percentage error in the phase celerity of the embedded dispersion relation (2.35) for $B = 1/15$ and $B = 0$ compared to phase celerity of the exact linear dispersion relation (2.36)

Figure 2.2 shows the percentage error of the wave celerities of the enhanced ($B = 1/15$) and classical ($B = 0$) Boussinesq equation sets, relative to the exact celerity calculated from (2.36). It is evident from the plot that the enhanced equations show

a significant improvement in linear dispersion, giving good accuracy ($< 2.5\%$ error) up to $kh \approx 3$.

2.3 Nonlinear shallow water equations

The nonlinear shallow water equations may be derived using the same technique as in Section 2.1, assuming $O(\epsilon) = 1$ and $\mu << 1$ where all nonlinear terms are retained and all the dispersive terms neglected. The equations may also be derived through depth integration of the continuity and Navier-Stokes equations, which is the method followed by Falconer (1993). This method allows the deviatoric stresses, i.e. viscosity and turbulence, to be carried through the derivation and can lead to a number of different versions of the shallow water equations.

For predominantly horizontal flows, vertical accelerations are assumed to be small in comparison to the acceleration due to gravity. Shear stresses in the z-direction are also neglected, leading to a hydrostatic pressure distribution, i.e. $p = \rho g(\zeta - z)$, where ρ is the water density.

The nonlinear shallow water equations implemented in the numerical model include the effects of bed friction and deviatoric stresses, and are given by

$$\frac{\partial \zeta}{\partial t} + \frac{\partial q_x}{\partial x} + \frac{\partial q_y}{\partial y} = 0, \tag{2.38a}$$

$$\frac{\partial q_x}{\partial t} + gd\frac{\partial \zeta}{\partial x} + \frac{\partial}{\partial x}\left(\frac{q_x^2}{d}\right) + \frac{\partial}{\partial y}\left(\frac{q_x q_y}{d}\right) = -\frac{\tau_{bx}}{\rho} + \frac{1}{\rho}\left(\frac{\partial}{\partial x}(dT_{xx}) + \frac{\partial}{\partial y}(dT_{xy})\right) \tag{2.38b}$$

and

$$\frac{\partial q_y}{\partial t} + gd\frac{\partial \zeta}{\partial y} + \frac{\partial}{\partial y}\left(\frac{q_y^2}{d}\right) + \frac{\partial}{\partial x}\left(\frac{q_x q_y}{d}\right) = -\frac{\tau_{by}}{\rho} + \frac{1}{\rho}\left(\frac{\partial}{\partial x}(dT_{xy}) + \frac{\partial}{\partial y}(dT_{yy})\right). \tag{2.38c}$$

τ_{bx} and τ_{by} are bed friction stresses, estimated empirically from

$$\tau_{bx} = \rho C_f u\sqrt{u^2 + v^2} \quad \text{and} \quad \tau_{by} = \rho C_f v\sqrt{u^2 + v^2}, \tag{2.39}$$

in which C_f is the bed roughness coefficient and T_{xx}, T_{xy} and T_{yy} are effective stress terms. The effective stresses are the deviatoric stresses, grouped together with the

stresses that arise from the non-uniformity of the vertical velocity profile as a result of the depth-integration process. They consist of three components: a molecular viscous stress, a Reynolds stress due to turbulent fluctuating velocity components, and a stress related to the non-uniformity of the vertical velocity profile. For most flow situations, the first and third components are significantly smaller than the Reynolds stresses, and can be neglected. The method of evaluating the Reynolds stresses is referred to as the turbulence model.

The Boussinesq eddy viscosity concept forms the basis of many turbulence models. It expresses the Reynolds stresses in terms of the gradients of the time-averaged velocity components, giving

$$T_{xx} = 2\rho\varepsilon\frac{\partial u}{\partial x}, \quad T_{xy} = \rho\varepsilon\left(\frac{\partial v}{\partial x} + \frac{\partial u}{\partial y}\right), \text{ and } T_{yy} = 2\rho\varepsilon\frac{\partial v}{\partial y}, \tag{2.40}$$

in which ρ is the fluid density and ε is the eddy viscosity. This is the turbulence model used by Borthwick and Barber (1992), and it is also implemented in the present model. The value of ε can be be calculated from constant or depth-averaged eddy viscosity models. In this research, a constant value has been assumed.

In shallow water, i.e. where $kh < \pi/10$, the wave celerity is given by $c = \sqrt{gd} = \sqrt{g(h+\zeta)}$. This implies that a wave crest travels faster than a wave trough, leading to a continual steepening of the wave front and eventual wave breaking, even where waves are propagating over a flat bottom. Thus, (2.38) does not have a solution of permanent form and use of the equations for modelling waves at the coast should be restricted to the inner surf zone.

In order to solve the nonlinear shallow water equations using a Godunov-type finite volume solver, (2.38) must be written in hyperbolic conservation form, which necessitates splitting of the $gd\frac{\partial\zeta}{\partial x}$ and $gd\frac{\partial\zeta}{\partial y}$ terms. Rogers et al. (2001) propose a method of splitting these terms that is numerically balanced for a non-uniform topography. In the x-direction, the split applied is as follows:

$$gd\frac{\partial\zeta}{\partial x} = \frac{g}{2}\frac{\partial(\zeta^2 + 2\zeta h)}{\partial x} - g\zeta\frac{\partial h}{\partial x}. \tag{2.41}$$

A similar split is applied in the y-direction. The resulting system may be written in

hyperbolic conservation form as

$$\frac{\partial \mathbf{u}}{\partial t} + \frac{\partial \mathbf{f}}{\partial x} + \frac{\partial \mathbf{g}}{\partial y} = \mathbf{s}, \tag{2.42}$$

where $\mathbf{u}, \mathbf{f}, \mathbf{g}$ and $\mathbf{s}$ are vectors representing the conserved variables, the fluxes in the x and y-directions and the source/sink terms respectively. These vectors are given by

$$\begin{aligned} \mathbf{u} &= \begin{bmatrix} \zeta \\ q_x \\ q_y \end{bmatrix}, \quad \mathbf{f} = \begin{bmatrix} q_x \\ \frac{q_x^2}{d} + \frac{1}{2}g(\zeta^2 + 2\zeta h) \\ \frac{q_x q_y}{d} \end{bmatrix}, \quad \mathbf{g} = \begin{bmatrix} q_y \\ \frac{q_x q_y}{d} \\ \frac{q_y^2}{d} + \frac{1}{2}g(\zeta^2 + 2\zeta h) \end{bmatrix} \quad \text{and} \\ \mathbf{s} &= \begin{bmatrix} 0 \\ g\zeta\frac{\partial h}{\partial x} - \frac{\tau_{bx}}{\rho} + \frac{1}{\rho}\left(\frac{\partial}{\partial x}(dT_{xx}) + \frac{\partial}{\partial y}(dT_{xy})\right) \\ g\zeta\frac{\partial h}{\partial y} - \frac{\tau_{by}}{\rho} + \frac{1}{\rho}\left(\frac{\partial}{\partial x}(dT_{xy}) + \frac{\partial}{\partial y}(dT_{yy})\right) \end{bmatrix}. \end{aligned} \tag{2.43}$$

2.4 Stage-discharge formulation

Formulation in terms of the free-surface elevation ζ and the still water depth h presents difficulties when applying the shallow water equations to problems that involve a wet-dry interface, as both h and ζ are difficult to define at the interface and in dry areas. Liang and Borthwick (2009) propose splitting the free-surface gradient terms as follows for the x-direction:

$$gd\frac{\partial \zeta}{\partial x} = \frac{g}{2}\frac{\partial(\eta^2 - 2z_b\eta)}{\partial x} + g\eta\frac{\partial z_b}{\partial x}, \tag{2.44}$$

and similarly in the y-direction, where $\eta = z_b + h + \zeta$. From Figure 2.1 it can be seen that because η is measured relative to the datum, it is always consistently defined. The system of shallow water equations implemented in the numerical model thus becomes

$$\frac{\partial \mathbf{u}}{\partial t} + \frac{\partial \mathbf{f}}{\partial x} + \frac{\partial \mathbf{g}}{\partial y} = \mathbf{s}, \tag{2.45}$$

where

$$\mathbf{u} = \begin{bmatrix} \eta \\ q_x \\ q_y \end{bmatrix}, \quad \mathbf{f} = \begin{bmatrix} q_x \\ \frac{q_x^2}{d} + \frac{1}{2}g(\eta^2 - 2\eta z_b) \\ \frac{q_x q_y}{d} \end{bmatrix}, \quad \mathbf{g} = \begin{bmatrix} q_y \\ \frac{q_x q_y}{d} \\ \frac{q_y^2}{d} + \frac{1}{2}g(\eta^2 - 2\eta z_b) \end{bmatrix} \quad \text{and}$$
$$\mathbf{s} = \begin{bmatrix} 0 \\ -\frac{\tau_{bx}}{\rho} - g\eta\frac{\partial z_b}{\partial x} + \frac{1}{\rho}\left(\frac{\partial}{\partial x}(dT_{xx}) + \frac{\partial}{\partial y}(dT_{xy})\right) \\ -\frac{\tau_{by}}{\rho} - g\eta\frac{\partial z_b}{\partial y} + \frac{1}{\rho}\left(\frac{\partial}{\partial x}(dT_{xy}) + \frac{\partial}{\partial y}(dT_{yy})\right) \end{bmatrix}. \tag{2.46}$$

The enhanced Boussinesq equation set given by (2.27) and (2.32) are also reformulated in terms of $(\eta, \mathbf{Q})$ for consistency and to facilitate the joining of the equation sets within the hybrid model. As the Boussinesq equations are only applied in deeper water where h and ζ are well defined, the presence of the still water depth h in the reformulated equations does not pose any difficulties. Thus, including the effects of bed friction and eddy viscosity, the enhanced Boussinesq equation set implemented in the numerical model is as follows:

$$\frac{\partial \eta}{\partial t} + \frac{\partial q_x}{\partial x} + \frac{\partial q_y}{\partial y} = 0, \tag{2.47a}$$

$$\begin{aligned} \frac{\partial q_x}{\partial t} + \frac{\partial(\frac{q_x^2}{d})}{\partial x} + \frac{g}{2}\frac{\partial \eta^2}{\partial x} - g\frac{\partial(\eta z_b)}{\partial x} + \frac{\partial(\frac{q_x q_y}{d})}{\partial y} &= -\frac{\tau_{bx}}{\rho} - g\eta\frac{\partial z_b}{\partial x} \\ &+ \frac{1}{\rho}\left(\frac{\partial}{\partial x}(dT_{xx}) + \frac{\partial}{\partial y}(dT_{xy})\right) \\ &+ \left(B + \frac{1}{3}\right)h^2\left(\frac{\partial^3 q_x}{\partial x^2 \partial t} + \frac{\partial^3 q_y}{\partial x \partial y \partial t}\right) \\ &+ Bgh^3\left(\frac{\partial^3 \eta}{\partial x^3} + \frac{\partial^3 \eta}{\partial x \partial y^2}\right) \\ &+ h\frac{\partial h}{\partial x}\left(\frac{1}{3}\frac{\partial^2 q_x}{\partial x \partial t} + \frac{1}{6}\frac{\partial^2 q_y}{\partial y \partial t} + 2Bgh\frac{\partial^2 \eta}{\partial x^2} + Bgh\frac{\partial^2 \eta}{\partial y^2}\right) \\ &+ h\frac{\partial h}{\partial y}\left(\frac{1}{6}\frac{\partial^2 q_y}{\partial x \partial t} + Bgh\frac{\partial^2 \eta}{\partial x \partial y}\right), \end{aligned} \tag{2.47b}$$

and

$$\begin{aligned} \frac{\partial q_y}{\partial t} + \frac{\partial(\frac{q_y^2}{d})}{\partial y} + \frac{g}{2}\frac{\partial \eta^2}{\partial y} - g\frac{\partial(\eta z_b)}{\partial y} + \frac{\partial(\frac{q_x q_y}{d})}{\partial x} &= -\frac{\tau_{by}}{\rho} - g\eta\frac{\partial z_b}{\partial y} \\ &+ \frac{1}{\rho}\left(\frac{\partial}{\partial x}(dT_{xy}) + \frac{\partial}{\partial y}(dT_{yy})\right) \end{aligned}$$

$$
\begin{aligned}
&+\left(B+\frac{1}{3}\right)h^2\left(\frac{\partial^3 q_y}{\partial y^2\partial t}+\frac{\partial^3 q_x}{\partial x\partial y\partial t}\right)\\
&+Bgh^3\left(\frac{\partial^3\eta}{\partial y^3}+\frac{\partial^3\eta}{\partial x^2\partial y}\right)\\
&+h\frac{\partial h}{\partial y}\left(\frac{1}{3}\frac{\partial^2 q_y}{\partial y\partial t}+\frac{1}{6}\frac{\partial^2 q_x}{\partial x\partial t}+2Bgh\frac{\partial^2\eta}{\partial y^2}+Bgh\frac{\partial^2\eta}{\partial x^2}\right)\\
&+h\frac{\partial h}{\partial x}\left(\frac{1}{6}\frac{\partial^2 q_x}{\partial y\partial t}+Bgh\frac{\partial^2\eta}{\partial x\partial y}\right). \qquad (2.47c)
\end{aligned}
$$

To facilitate Runge-Kutta time-stepping, (2.47b) and (2.47c) are rewritten in the form suggested by Bradford and Sanders (2002), keeping all time-dependent terms on the left hand side of the equation, and the non-time-dependent terms on the right. The system then becomes

$$
\frac{\partial\eta}{\partial t}=-\frac{\partial q_x}{\partial x}-\frac{\partial q_y}{\partial y}, \qquad (2.48a)
$$

$$
\begin{aligned}
F_x\left(\frac{\partial q_x}{\partial t}\right)=&-\frac{\partial(\frac{q_x^2}{d})}{\partial x}-\frac{g}{2}\frac{\partial\eta^2}{\partial x}+g\frac{\partial(\eta z_b)}{\partial x}-\frac{\partial(\frac{q_x q_y}{d})}{\partial y}-\frac{\tau_{bx}}{\rho}-g\eta\frac{\partial z_b}{\partial x}\\
&+\frac{1}{\rho}\left(\frac{\partial}{\partial x}(dT_{xx})+\frac{\partial}{\partial y}(dT_{xy})\right)\\
&+Bgh^3\left(\frac{\partial^3\eta}{\partial x^3}+\frac{\partial^3\eta}{\partial x\partial y^2}\right)+2Bgh^2\frac{\partial h}{\partial x}\frac{\partial^2\eta}{\partial x^2}\\
&+Bgh^2\frac{\partial h}{\partial x}\frac{\partial^2\eta}{\partial y^2}+Bgh^2\frac{\partial h}{\partial y}\frac{\partial^2\eta}{\partial x\partial y} \qquad (2.48b)
\end{aligned}
$$

and

$$
\begin{aligned}
F_y\left(\frac{\partial q_y}{\partial t}\right)=&-\frac{\partial(\frac{q_y^2}{d})}{\partial y}-\frac{g}{2}\frac{\partial\eta^2}{\partial y}+g\frac{\partial(\eta z_b)}{\partial y}-\frac{\partial(\frac{q_x q_y}{d})}{\partial x}-\frac{\tau_{by}}{\rho}-g\eta\frac{\partial z_b}{\partial y}\\
&+\frac{1}{\rho}\left(\frac{\partial}{\partial x}(dT_{xy})+\frac{\partial}{\partial y}(dT_{yy})\right)\\
&+Bgh^3\left(\frac{\partial^3\eta}{\partial y^3}+\frac{\partial^3\eta}{\partial x^2\partial y}\right)+2Bgh^2\frac{\partial h}{\partial y}\frac{\partial^2\eta}{\partial y^2}\\
&+Bgh^2\frac{\partial h}{\partial y}\frac{\partial^2\eta}{\partial x^2}+Bgh^2\frac{\partial h}{\partial x}\frac{\partial^2\eta}{\partial x\partial y}, \qquad (2.48c)
\end{aligned}
$$

where

$$
F_x=\frac{\partial q_x}{\partial t}-\left(B+\frac{1}{3}\right)h^2\left(\frac{\partial^3 q_x}{\partial x^2\partial t}+\frac{\partial^3 q_y}{\partial x\partial y\partial t}\right)
$$

$$- h\frac{\partial h}{\partial x}\left(\frac{1}{3}\frac{\partial^2 q_x}{\partial x \partial t} + \frac{1}{6}\frac{\partial^2 q_y}{\partial y \partial t}\right) - \frac{h}{6}\frac{\partial h}{\partial x}\frac{\partial^2 q_x}{\partial y \partial t} \tag{2.49a}$$

and

$$\begin{aligned} F_y =& \frac{\partial q_y}{\partial t} - \left(B + \frac{1}{3}\right) h^2 \left(\frac{\partial^3 q_y}{\partial y^2 \partial t} + \frac{\partial^3 q_x}{\partial x \partial y \partial t}\right) \\ & - h\frac{\partial h}{\partial y}\left(\frac{1}{3}\frac{\partial^2 q_y}{\partial y \partial t} + \frac{1}{6}\frac{\partial^2 q_x}{\partial x \partial t}\right) - \frac{h}{6}\frac{\partial h}{\partial x}\frac{\partial^2 q_x}{\partial y \partial t}. \end{aligned} \tag{2.49b}$$

2.5 Wave generation

Piston paddles are often used to generate waves in laboratory flumes and basins. A wave flume will typically have a single paddle (Figure 2.3), whereas wave basins incorporate multiple paddles for the generation of both long- and short-crested seas (Figure 2.4). In either case, the paddles move horizontally according to a displacement time series calculated using wavemaker theory, to produce waves of the desired amplitude and frequency. An overview of the theory is given in Chapter 6 of Dean and Dalrymple (1991).

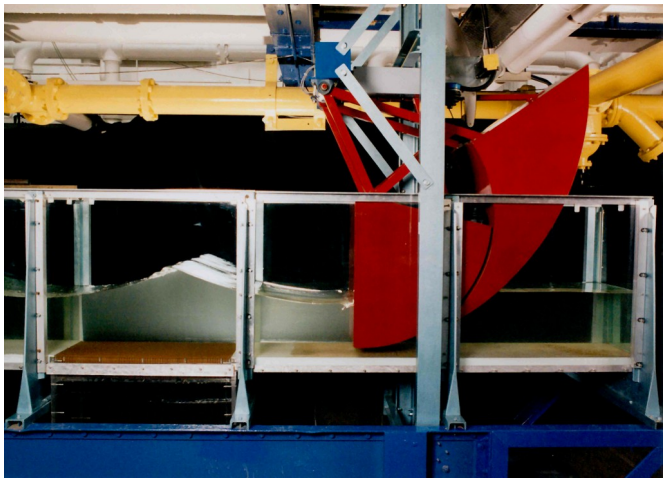

Figure 2.3: Piston paddle in a laboratory flume (www.edesign.co.uk)

First-order wavemaker theory is derived directly from linear wave theory with additional lateral boundary conditions applied to take account of the moving wavemaker.

Figure 2.4: Piston paddles in a laboratory wave basin (www.edesign.co.uk)

It leads to the following solutions for the ζ and Φ at the wave maker.

$$\zeta \approx \zeta_0 = a\cos(kx - \omega t) \tag{2.50a}$$

and

$$\Phi \approx \Phi_0 = -\frac{ag}{\omega}\frac{\cosh(k(h+z))}{\cosh(kh)}\sin(kx - \omega t), \tag{2.50b}$$

where a is the wave amplitude, k is the wave number and ω is the angular frequency of the wave. Application of the superposition principle leads to the following expression for irregular waves,

$$\zeta \approx \sum_{n=1}^{N} a_n \cos(k_n x - \omega_n t + \phi_n), \tag{2.51}$$

where N is the number of regular wave trains under consideration. The phase, ϕ_n, is set to zero or a fixed value for focused wave generation.

For the piston-paddle problem, the horizontal flow velocity at the paddle must match the speed of the paddle motion, giving rise to the following boundary condition:

$$\Phi_x = \frac{\partial x_p}{\partial t} \quad \text{at } x = x_p, \tag{2.52}$$

where x_p is the paddle displacement. Expressing Φ as a power series and expanding about $x = 0$ leads to the following first-order expression for the paddle displacement series for regular waves

$$x_p = a_p \sin(\omega t), \tag{2.53}$$

where a_p is the amplitude of the paddle motion. This can be solved to give

$$\zeta_0 = a_p c_0 \cos(kx - \omega t) + \sum_{j=1}^{\infty} a_p |c_j| e^{-|k_j|x} \sin(\omega t). \tag{2.54}$$

The first term in (2.54) represents a progressive wave made by the wavemaker, while the summation term represents a series of standing waves, called evanescent waves, which decay away from the wavemaker. These waves arise because the vertical velocity profile of the generated wave does not match the paddle motion which is constant with depth. For the progressive wave, the wavenumber $k_0 = k$ is calculated from the linear dispersion relation

$$\omega^2 = gk \tanh kh. \tag{2.55}$$

The wavenumber k_j is purely imaginary and associated with the j^{th} evanescent mode ($j = 1, 2, ...$). It also satisfies the dispersion relation (2.55) which can be written more generally as,

$$\omega^2 = -gk_j \tan k_j h, \tag{2.56}$$

where the first solution (i.e. for $j = 0$) is $k_0 = ik$. The amplitudes of the evanescent waves decrease exponentially with increasing x, so that away from the wavemaker, the target wave is generated to first-order. In (2.54), the coefficient c_j is given by

$$c_j = \frac{2(\cosh(2k_j h) - 1)}{\sinh(2k_j h) + 2k_j h}. \tag{2.57}$$

For the evanescent waves, i.e. $j = 1, 2, ...$, this number is purely imaginary, but for $j = 0$, c_0 is real and is known as the Biésel transfer function. It gives the relationship between the paddle amplitude, a_p and the amplitude of the generated wave, i.e.

$$a = c_0 a_p. \tag{2.58}$$

Therefore for irregular waves, the first-order paddle signal can be calculated from

$$x_p = \sum_{n=1}^{N} \frac{a_n}{c_{0_n}} \sin(\omega_n t). \tag{2.59}$$

2.6 Chapter summary

- In this chapter, the classical Boussinesq equations are derived through a power series expansion of the velocity potential, used in conjunction with the Laplace equation. The manipulations that lead to the enhanced Boussinesq equation set of Madsen and Sørensen (1992) are then described, and the improvement in the dispersive properties is demonstrated by comparing the embedded dispersion relation of the enhanced equations with the exact linear dispersion relation.

- A derivation of the nonlinear shallow water equations is presented, and both equation sets are reformulated in terms of stage and discharge $(\eta, \mathbf{Q})$. A turbulence model that expresses the Reynolds' stresses in terms of the eddy viscosity and time-averaged velocity components is included in the governing equations.

- First-order wavemaker theory for piston-type paddles is discussed.

Chapter 3

Numerical implementation

This chapter details the numerical methods applied to create the 2DH numerical solver. A sample basin layout is given in Figure 3.1 and this can be used as a reference throughout the chapter. Waves are generated by numerical wavemakers at the western boundary. A mapping technique is implemented in the region adjacent to the paddles to transform this moving, physical domain onto a fixed computational domain to facilitate the solution of the governing Boussinesq equation set. A second-order finite-difference scheme is used to discretise the Boussinesq equations, which are then solved using the conjugate gradient method with fourth-order Runge-Kutta time stepping. The nonlinear shallow water equations are solved using a shock-capturing finite volume method with an in-built wetting and drying scheme which models the moving shoreline. The criterion for the switch from the Boussinesq to the shallow water domain is based on the magnitude of the slope of the water surface.

3.1 Choice of methodology

A hybrid finite difference - finite volume scheme is chosen to implement the governing Boussinesq and shallow water equation sets respectively. One of the main aims of this thesis is to extend the solver of Orszaghova (2011); Orszaghova's model implements such a hybrid scheme and has been extensively validated, producing excellent results in one-horizontal-dimension. Therefore, this was the main reason for choosing

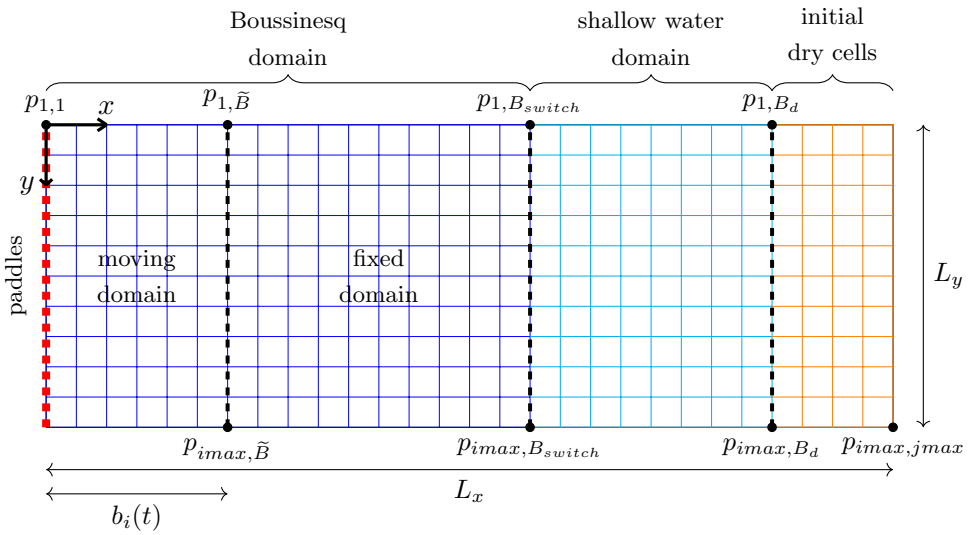

Figure 3.1: Sample basin layout

this methodology. While an argument could be made for implementing a finite volume method throughout the whole domain, finite differences present an intuitive and relatively straightforward method for dealing with the more complicated Boussinesq equation set. In order to model steep-fronted flows using the shallow water equations, a switch to a finite volume scheme with shock-capturing abilities is required as finite differences cannot deal with discontinuities. Therefore, the method described by Liang and Borthwick (2009) is used to implement the shallow water equations in two-horizontal-dimensions in the surf zone.

3.2 Grid definition and indexing convention

In the numerical model, the physical domain is represented by a two-dimensional, rectangular grid of points (see Figure 3.1). An arbitrary point, $p_{i,j}$ on the grid is referenced using a row-column indexing notation whereby the i, j subscripts represent the indices of points in the y- and x-directions respectively. Thus, for a typical rectangular domain, the northwest corner is referenced by $p_{1,1}$ and the southeast corner by $p_{imax,jmax}$ as shown in Figure 3.1. The subscript $imax$ is the total number of grid points in the y-direction and $jmax$ is the number of points in the x-direction. The computational

grid extends in the x-direction from $j = 1 \ldots B_d$, i.e. dry cells are excluded, unless they are about to be flooded (see Section 3.4.3). For a fully inundated basin, $B_d = jmax$.

3.3 Numerical implementation of the Boussinesq equations

3.3.1 Domain mapping

The physical domain under consideration is represented by a rectangular grid of length L_x and width L_y. Initially, when the paddles are at rest in the zero position, the Cartesian coordinates of the underlying uniform grid are given by

$$(x_j, y_i) = ((j-1)\Delta x, (i-1)\Delta y), \tag{3.1}$$

where $\Delta x = L_x/(j_{max} - 1)$ and $\Delta y = L_y/(i_{max} - 1)$, for $j = 1...j_{max}$ and $i = 1...i_{max}$. Δx and Δy are the spacings between grid points in the $x-$ and $y-$directions respectively.

The dimensions of the basin vary with time when the paddles are moving. To deal with this, the region governed by the Boussinesq equations is divided into two zones: the moving domain and the fixed domain. The moving domain is of variable length $b_i(t)$ in the x-direction and fixed width, L_y. At $t = 0$, all of the paddles are in the zero position, and the initial $x-$dimension of the moving domain is given by a fixed length, $b_i(t = 0)$, herein referred to as $b0$, which contains a fixed number of grid points, $\tilde{B}$, in the $x-$direction. The length of $b0$, and consequently the value of $\tilde{B}$ varies depending on the problem under consideration. A similar approach is adopted to that of Orszaghova (2011), whereby $b0$ is set to be approximately 10 times the maximum paddle sweep.

When the paddles at the western boundary are in motion, the lattice of grid points that define the paddle domain stretches and compresses as the paddles move. In order to avoid re-meshing in this region at every time step, a transformation is used to map the moving grid onto a fixed computational grid to facilitate the solution of the governing equations. As the paddles are confined to the western edge of the tank and can only move in the x-direction, the mapping employed is a function of x only. Each

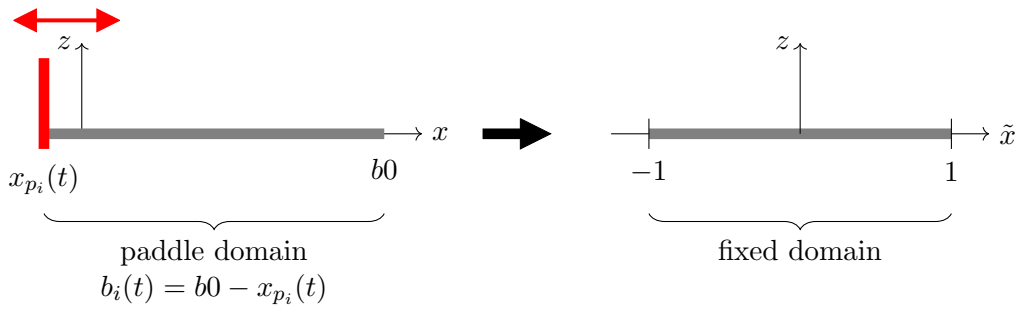

Figure 3.2: Paddle domain transformation applied to moving domain

moving row of grid points in the paddle domain is mapped onto a fixed row with points distributed evenly on the interval $(-1, 1)$, with spacing, $\Delta\tilde{x} = 2/(\widetilde{B} - 1)$.

The initial length of the paddle domain is given by a fixed length, $b0$. As the paddles move, each row, i, of the grid has a variable length $b_i(t) = b0 - x_{p_i}(t)$, where $x_{p_i}(t)$ is the paddle displacement time series for the i-th paddle. The transformation from the moving (x, y, t) domain to the fixed $(\tilde{x}, \tilde{y}, \tilde{t})$ domain, is based on the following mappings:

$$\tilde{x} = -1 + 2\left(\frac{x - x_{p_i}(t)}{b_i(t)}\right), \tag{3.2a}$$

$$\tilde{y} = y, \tag{3.2b}$$

$$\tilde{t} = t \tag{3.2c}$$

Thus, $f(x, y, t) \to \tilde{f}(\tilde{x}, \tilde{y}, \tilde{t})$. The transformed basic derivative operators are derived by applying the chain rule, i.e.

$$\frac{\partial f}{\partial x} = \frac{\partial \tilde{f}}{\partial \tilde{x}}\frac{\partial \tilde{x}}{\partial x} + \frac{\partial \tilde{f}}{\partial \tilde{y}}\frac{\partial \tilde{y}}{\partial x} + \frac{\partial \tilde{f}}{\partial \tilde{t}}\frac{\partial \tilde{t}}{\partial x},$$

with similar expressions for $\frac{\partial f}{\partial y}$ and $\frac{\partial f}{\partial t}$, to the mappings in (3.2), yielding

$$\frac{\partial}{\partial x} = \frac{2}{b_i(t)}\frac{\partial}{\partial \tilde{x}}, \tag{3.3a}$$

$$\frac{\partial}{\partial y} = \frac{\partial}{\partial \tilde{y}}, \tag{3.3b}$$

$$\frac{\partial}{\partial t} = \frac{\partial}{\partial \tilde{t}} + \frac{1}{b_i(t)}\frac{\partial b_i(t)}{\partial \tilde{t}}(1 - \tilde{x})\frac{\partial}{\partial \tilde{x}}. \tag{3.3c}$$

Higher order and mixed derivatives are obtained through careful combination of the above operators and are detailed in Appendix A.

Application of the transformations in (3.3) to (2.47) results in the following mapped Boussinesq equation set:

$$\frac{\partial \eta}{\partial \tilde{t}} = -\frac{1}{b}\frac{\partial b}{\partial \tilde{t}}(1-\tilde{x})\frac{\partial \eta}{\partial \tilde{x}} - \frac{2}{b}\frac{\partial q_x}{\partial \tilde{x}} - \frac{\partial q_y}{\partial \tilde{y}}, \tag{3.4a}$$

$$\begin{aligned}
\frac{\partial q_x}{\partial \tilde{t}} =& -\frac{1}{b}\frac{\partial b}{\partial \tilde{t}}(1-\tilde{x})\frac{\partial q_x}{\partial \tilde{x}} - \frac{2}{b}\frac{\partial}{\partial \tilde{x}}\left(\frac{q_x^2}{d}\right) - \frac{g}{b}\frac{\partial \eta^2}{\partial \tilde{x}} + \frac{2}{b}g\frac{\partial(\eta z_b)}{\partial \tilde{x}} - g\eta\frac{\partial z_b}{\partial \tilde{x}} - \frac{\tau_{bx}}{\rho} - \frac{\partial}{\partial \tilde{y}}\left(\frac{q_x q_y}{d}\right) \\
&+ \left(B+\frac{1}{3}\right)h^2\left[\frac{4}{b^2}\frac{\partial^3 q_x}{\partial \tilde{x}^2\partial \tilde{t}} + \frac{4}{b^3}\frac{\partial b}{\partial \tilde{t}}\left\{(1-\tilde{x})\frac{\partial^3 q_x}{\partial \tilde{x}^3} - 2\frac{\partial^2 q_x}{\partial \tilde{x}^2}\right\}\right] \\
&+ \left(B+\frac{1}{3}\right)h^2\left[\frac{2}{b}\frac{\partial^3 q_y}{\partial \tilde{x}\partial \tilde{y}\partial \tilde{t}} + \frac{2}{b^2}\frac{\partial b}{\partial \tilde{t}}\left\{(1-\tilde{x})\frac{\partial^3 q_y}{\partial \tilde{x}^2\partial \tilde{y}} - \frac{\partial^2 q_y}{\partial \tilde{x}\partial \tilde{y}}\right\}\right] \\
&+ Bgh^2\left[\frac{8}{b^3}\frac{\partial \eta^3}{\partial \tilde{x}^3} + \frac{2}{b}\frac{\partial \eta^3}{\partial \tilde{x}\partial \tilde{y}^2}\right] \\
&+ \frac{h}{3}\frac{2}{b}\frac{\partial h}{\partial \tilde{x}}\left[\frac{2}{b}\frac{\partial^2 q_x}{\partial \tilde{x}\partial \tilde{t}} + \frac{2}{b^2}\frac{\partial b}{\partial \tilde{t}}\left\{(1-\tilde{x})\frac{\partial^2 q_x}{\partial \tilde{x}^2} - \frac{\partial q_x}{\partial \tilde{x}}\right\}\right] \\
&+ \frac{h}{6}\frac{2}{b}\frac{\partial h}{\partial \tilde{x}}\left[\frac{\partial^2 q_y}{\partial \tilde{y}\partial \tilde{t}} + \frac{1}{b}\frac{\partial b}{\partial \tilde{t}}(1-\tilde{x})\frac{\partial^2 q_y}{\partial \tilde{x}\partial \tilde{y}}\right] + 2Bgh^2\frac{8}{b^3}\frac{\partial h}{\partial \tilde{x}}\frac{\partial \eta^2}{\partial \tilde{x}^2} \\
&+ Bgh^2\frac{2}{b}\frac{\partial h}{\partial \tilde{x}}\frac{\partial \eta^2}{\partial \tilde{y}^2} + \frac{h}{6}\frac{\partial h}{\partial \tilde{y}}\left[\frac{2}{b}\frac{\partial^2 q_y}{\partial \tilde{x}\partial \tilde{t}} + \frac{2}{b^2}\frac{\partial b}{\partial \tilde{t}}\left\{(1-\tilde{x})\frac{\partial^2 q_y}{\partial \tilde{x}^2} - \frac{\partial q_y}{\partial \tilde{x}}\right\}\right] \\
&+ Bgh^2\frac{\partial h}{\partial \tilde{y}}\frac{2}{b}\frac{\partial \eta^2}{\partial \tilde{x}\partial \tilde{y}},
\end{aligned} \tag{3.4b}$$

and

$$\begin{aligned}
\frac{\partial q_y}{\partial \tilde{t}} =& -\frac{1}{b}\frac{\partial b}{\partial \tilde{t}}(1-\tilde{x})\frac{\partial q_y}{\partial \tilde{x}} - \frac{\partial}{\partial \tilde{y}}\left(\frac{q_y^2}{d}\right) - \frac{g}{2}\frac{\partial \eta^2}{\partial \tilde{y}} + g\frac{\partial(\eta z_b)}{\partial \tilde{y}} - g\eta\frac{\partial z_b}{\partial \tilde{y}} - \frac{\tau_{by}}{\rho} - \frac{2}{b}\frac{\partial}{\partial \tilde{x}}\left(\frac{q_x q_y}{d}\right) \\
&+ \left(B+\frac{1}{3}\right)h^2\left[\frac{\partial^3 q_y}{\partial \tilde{y}^2\partial \tilde{t}} + \frac{1}{b}\frac{\partial b}{\partial \tilde{t}}(1-\tilde{x})\frac{\partial^3 q_y}{\partial \tilde{x}\partial \tilde{y}^2}\right] \\
&+ \left(B+\frac{1}{3}\right)h^2\left[\frac{2}{b}\frac{\partial^3 q_x}{\partial \tilde{x}\partial \tilde{y}\partial \tilde{t}} + \frac{2}{b^2}\frac{\partial b}{\partial \tilde{t}}\left\{(1-\tilde{x})\frac{\partial^3 q_x}{\partial \tilde{x}^2\partial \tilde{y}} - \frac{\partial^2 q_x}{\partial \tilde{x}\partial \tilde{y}}\right\}\right] \\
&+ Bgh^2\left[\frac{\partial \eta^3}{\partial \tilde{y}^3} + \frac{4}{b^2}\frac{\partial \eta^3}{\partial \tilde{x}^2\partial \tilde{y}}\right] \\
&+ \frac{h}{3}\frac{\partial h}{\partial \tilde{y}}\left[\frac{\partial^2 q_y}{\partial \tilde{y}\partial \tilde{t}} + \frac{1}{b}\frac{\partial b}{\partial \tilde{t}}(1-\tilde{x})\frac{\partial^2 q_y}{\partial \tilde{x}\partial \tilde{y}}\right] \\
&+ \frac{h}{6}\frac{\partial h}{\partial \tilde{y}}\left[\frac{2}{b}\frac{\partial^2 q_x}{\partial \tilde{x}\partial \tilde{t}} + \frac{2}{b^2}\frac{\partial b}{\partial \tilde{t}}\left\{(1-\tilde{x})\frac{\partial^2 q_x}{\partial \tilde{x}^2} - \frac{\partial q_x}{\partial \tilde{x}}\right\}\right] \\
&+ 2Bgh^2\frac{\partial h}{\partial \tilde{y}}\frac{\partial \eta^2}{\partial \tilde{y}^2} + Bgh^2\frac{\partial h}{\partial \tilde{y}}\frac{4}{b^2}\frac{\partial \eta^2}{\partial \tilde{x}^2} \\
&+ \frac{h}{6}\frac{2}{b}\frac{\partial h}{\partial \tilde{x}}\left[\frac{\partial^2 q_x}{\partial \tilde{y}\partial \tilde{t}} + \frac{1}{b}\frac{\partial b}{\partial \tilde{t}}(1-\tilde{x})\frac{\partial^2 q_x}{\partial \tilde{x}\partial \tilde{y}}\right] + Bgh^2\frac{4}{b^2}\frac{\partial h}{\partial \tilde{x}}\frac{\partial \eta^2}{\partial \tilde{x}\partial \tilde{y}}
\end{aligned} \tag{3.4c}$$

where b represents $b_i(t)$. In the fixed domain of the Boussinesq region, the equation set given by (2.47) applies.

3.3.2 Finite difference discretisation

The Boussinesq equations are discretised using a second-order finite difference scheme. This involves a three point stencil for first and second derivatives and a five point stencil for higher order derivatives. The stencils for the spatial cross-derivative terms, $\partial^2/\partial x\partial y$, $\partial^3/\partial x^2\partial y$ and $\partial^3/\partial x\partial y^2$, span three points in the x and y directions.

The derivative approximations for first, second and third derivatives for some arbitrary function f at a point $p_{i,j}$ in space are given in (3.5) below. Note that the subscripts i and j refer to the y and x directions respectively.

$$f_x(p_{i,j}) = \frac{1}{2\Delta x}\left(f_{i,j+1} - f_{i,j-1}\right) + O(\Delta x^2), \tag{3.5a}$$

$$f_{xx}(p_{i,j}) = \frac{1}{\Delta x^2}\left(f_{i,j+1} - 2f_{i,j} + f_{i,j-1}\right) + O(\Delta x^2), \tag{3.5b}$$

$$f_{xxx}(p_{i,j}) = \frac{1}{2\Delta x^3}\left(f_{i,j+2} - f_{i,j+1} + f_{i,j-1} - f_{i,j-2}\right) + O(\Delta x^2), \tag{3.5c}$$

$$f_y(p_{i,j}) = \frac{1}{2\Delta y}\left(f_{i+1,j} - f_{i-1,j}\right) + O(\Delta y^2), \tag{3.5d}$$

$$f_{yy}(p_{i,j}) = \frac{1}{\Delta y^2}\left(f_{i+1,j} - 2f_{i,j} + f_{i-1,j}\right) + O(\Delta y^2), \tag{3.5e}$$

$$f_{yyy}(p_{i,j}) = \frac{1}{2\Delta y^3}\left(f_{i+2,j} - f_{i+1,j} + f_{i-1,j} - f_{i-2,j}\right) + O(\Delta y^2). \tag{3.5f}$$

Finite difference expressions for the mixed derivative terms are obtained through combinations of the above stencils. For example,

$$f_{xy}(p_{i,j}) = \frac{1}{4\Delta x\Delta y}\left(f_{i+1,j+1} - f_{i+1,j-1} - f_{i-1,j+1} + f_{i-1,j-1}\right) + O(\Delta x^2, \Delta y^2). \tag{3.6}$$

Expressions for higher order mixed derivative terms are provided in Appendix B.

The finite difference expressions at the interface between the moving and fixed domains must be treated carefully, because different governing equation sets and grid spacing exist either side of $j = \widetilde{B}$. At a point $p_{i,j}$, where $j = wide\tilde{B}$, the three-point stencil defining first and second derivatives and the five-point higher order stencils will

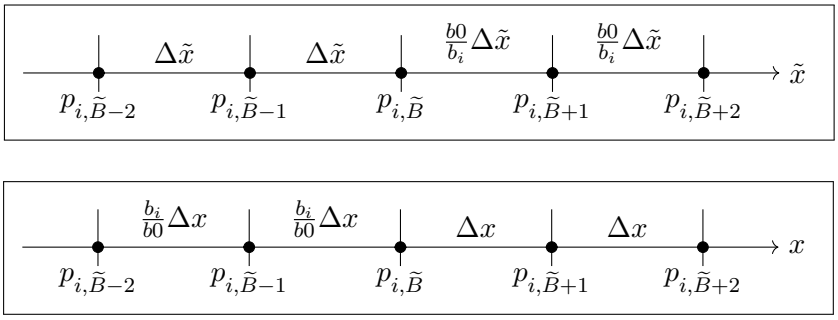

Figure 3.3: Computational grid in the region of $j = \widetilde{B}$ viewed from (a) the moving domain, and (b) the fixed domain.

span both regions. Where third-order derivatives are calculated at $j = \widetilde{B} - 1$, or $j = \widetilde{B} + 1$, the five-point stencil employed will again span both regions.

Figure 3.3 shows the grid in the region of the interface, viewed from the perspective of the transformed, moving domain 3.3 (a), and the fixed domain 3.3 (b). Depending on whether the spatial derivative is being evaluated at a point within the moving domain or the fixed domain, the spatial increment in the adjacent domain must be multiplied by a factor that will maintain the correct ratio between the increments. For example, when the paddles are moving forward, compressing the grid, the grid spacing in the moving domain will be smaller than that in the fixed domain, therefore when evaluating the spatial derivative at $p_{i,\widetilde{B}}$, the grid spacing in the adjacent fixed domain must be multiplied by $\frac{b0}{b_i}$. A non-uniform stencil is then required to deal with the different spatial increments. Mixed derivative non-uniform stencils are obtained through careful combination of the non-uniform and uniform stencils. Expressions for the first and second-order stencils are given in (3.7), with higher order expressions detailed in Appendix B.2. Note that $b_i(t)$ is abbreviated to b_i.

$$\begin{aligned} f_{\tilde{x}}(p_{i,j=\widetilde{B}}) = &- \frac{1}{\Delta\tilde{x}}\left(\frac{b0}{b_i + b0}\right) f_{i,\widetilde{B}-1} \\ &- \frac{1}{\Delta\tilde{x}}\left(\frac{b_i - b0}{b0}\right) f_{i,\widetilde{B}} \\ &+ \frac{1}{\Delta\tilde{x}}\left(\frac{b_i^2}{b0(b_i + b0)}\right) f_{i,\widetilde{B}+1}, \end{aligned} \tag{3.7a}$$

$$
\begin{aligned}
f_{\tilde{x}\tilde{x}}(p_{i,j=\widetilde{B}}) =& \frac{1}{\Delta\tilde{x}^2}\left(\frac{2b_i}{b_i+b0}\right) f_{i,\widetilde{B}-1}, \\
&- \frac{1}{\Delta\tilde{x}^2}\left(\frac{2b_i}{b0}\right) f_{i,\widetilde{B}} \\
&+ \frac{1}{\Delta\tilde{x}^2}\left(\frac{2b_i^2}{b0(b_i+b0)}\right) f_{i,\widetilde{B}+1},
\end{aligned} \tag{3.7b}
$$

$$
\begin{aligned}
f_{\tilde{x}y}(p_{i,j=\widetilde{B}}) =& -\frac{1}{2\Delta\tilde{x}\Delta y}\left(\frac{b0}{b_i+b0}\right)(f_{i+1,\widetilde{B}-1} - f_{i-1,\widetilde{B}-1}) \\
&- \frac{1}{2\Delta\tilde{x}\Delta y}\left(\frac{b_i-b0}{b0}\right)(f_{i+1,\widetilde{B}} - f_{i-1,\widetilde{B}}) \\
&+ \frac{1}{2\Delta\tilde{x}\Delta y}\left(\frac{b_i^2}{b0(b_i+b0)}\right)(f_{i+1,\widetilde{B}+1} - f_{i-1,\widetilde{B}+1}).
\end{aligned} \tag{3.7c}
$$

3.3.3 Time integration for the Boussinesq equations

The discretised systems to be solved can be written as

$$\boldsymbol{\eta}_t = \mathbf{a}(\eta, q_x, q_y) \tag{3.8a}$$

$$\mathbf{A}\mathbf{Q}_t = \mathbf{b}(\eta, q_x, q_y) \tag{3.8b}$$

where $\boldsymbol{\eta}$ represents the vector of values of η, and $\mathbf{Q}$ represents a vector containing values of q_x and q_y at each grid point within the Boussinesq domain. $\mathbf{a}$ is the vector of non-time-dependent terms corresponding to the right hand side of equation 2.48a, and $\mathbf{b}$ is a similar vector representing the right hand side of equations 2.48b and 2.48c. Thus $\mathbf{Q}$ and $\mathbf{b}$ have double the number of values of $\boldsymbol{\eta}$ and $\mathbf{a}$. $\mathbf{A}$ is a matrix of coefficients resulting from the discretisation of equations 2.49a and b, and is of size $(m \times m)$, where $m = imax \times B_{switch} \times 2)$. The system 3.8 is integrated forward in time using a fourth-order Runge-Kutta algorithm (RK4), which advances the equations as follows:

$$\boldsymbol{\eta}^{n+1} = \boldsymbol{\eta}^n + \frac{1}{6}\Delta t\left(\frac{\partial\boldsymbol{\eta}}{\partial t}_1 + 2\frac{\partial\boldsymbol{\eta}}{\partial t}_2 + 2\frac{\partial\boldsymbol{\eta}}{\partial t}_3 + \frac{\partial\boldsymbol{\eta}}{\partial t}_4\right) \tag{3.9a}$$

and

$$\mathbf{Q}^{n+1} = \mathbf{Q}^n + \frac{1}{6}\Delta t\left(\frac{\partial\mathbf{Q}}{\partial t}_1 + 2\frac{\partial\mathbf{Q}}{\partial t}_2 + 2\frac{\partial\mathbf{Q}}{\partial t}_3 + \frac{\partial\mathbf{Q}}{\partial t}_4\right), \tag{3.9b}$$

where

$$\frac{\partial \boldsymbol{\eta}}{\partial t}_1 = \mathbf{a}\left(\boldsymbol{\eta}^n, \mathbf{Q}^n\right), \tag{3.10a}$$

$$\frac{\partial \boldsymbol{\eta}}{\partial t}_2 = \mathbf{a}\left(\boldsymbol{\eta}^n + \frac{1}{2}\Delta t \frac{\partial \boldsymbol{\eta}}{\partial t}_1, \mathbf{Q}^n + \frac{1}{2}\Delta t \frac{\partial \mathbf{Q}^n}{\partial t}_1\right), \tag{3.10b}$$

$$\frac{\partial \boldsymbol{\eta}}{\partial t}_3 = \mathbf{a}\left(\boldsymbol{\eta}^n + \frac{1}{2}\Delta t \frac{\partial \boldsymbol{\eta}}{\partial t}_2, \mathbf{Q}^n + \frac{1}{2}\Delta t \frac{\partial \mathbf{Q}^n}{\partial t}_2\right), \tag{3.10c}$$

$$\frac{\partial \boldsymbol{\eta}}{\partial t}_4 = \mathbf{a}\left(\boldsymbol{\eta}^n + \Delta t \frac{\partial \boldsymbol{\eta}}{\partial t}_3, \mathbf{Q}^n + \Delta t \frac{\partial \mathbf{Q}^n}{\partial t}_3\right), \tag{3.10d}$$

and

$$\mathbf{A}\frac{\partial \mathbf{Q}}{\partial t}_1 = \mathbf{b}\left(\boldsymbol{\eta}^n, \mathbf{Q}^n\right), \tag{3.11a}$$

$$\mathbf{A}\frac{\partial \mathbf{Q}}{\partial t}_2 = \mathbf{b}\left(\boldsymbol{\eta}^n + \frac{1}{2}\Delta t \frac{\partial \boldsymbol{\eta}}{\partial t}_1, \mathbf{Q}^n + \frac{1}{2}\Delta t \frac{\partial \mathbf{Q}^n}{\partial t}_1\right), \tag{3.11b}$$

$$\mathbf{A}\frac{\partial \mathbf{Q}}{\partial t}_3 = \mathbf{b}\left(\boldsymbol{\eta}^n + \frac{1}{2}\Delta t \frac{\partial \boldsymbol{\eta}}{\partial t}_2, \mathbf{Q}^n + \frac{1}{2}\Delta t \frac{\partial \mathbf{Q}^n}{\partial t}_2\right), \tag{3.11c}$$

$$\mathbf{A}\frac{\partial \mathbf{Q}}{\partial t}_4 = \mathbf{b}\left(\boldsymbol{\eta}^n + \Delta t \frac{\partial \boldsymbol{\eta}}{\partial t}_3, \mathbf{Q}^n + \Delta t \frac{\partial \mathbf{Q}^n}{\partial t}_3\right). \tag{3.11d}$$

The superscripts n and $n+1$ refer to the current and next time step respectively.

Conjugate gradient solver

From (3.11) above, it can be seen that at each stage of the RK4 algorithm, a linear system of the form $\mathbf{Ax} = \mathbf{b}$ must be solved, where $\mathbf{x}$ is the vector of $\frac{\partial q_x}{\partial t}$ and $\frac{\partial q_y}{\partial t}$ at each grid point. $\mathbf{A}$ and $\mathbf{b}$ are as described in the previous section. The matrix $\mathbf{A}$ is a real, symmetric, positive definite, sparse banded matrix. The conjugate gradient method, originally proposed by Hestenes and Stiefel (1952) is suited to the numerical solution of such a system. It stems from the method of steepest descent, but instead of searching in the direction in which the function to be minimised, f, decreases most quickly, the search directions used are A-orthogonal to each other. Two vectors, d_i and d_j are said to be A-orthogonal, or conjugate, if

$$d_i^T \mathbf{A} d_j = 0.$$

Given the inputs $\mathbf{A}$, $\mathbf{b}$ and a starting estimate of the solution, $\mathbf{x}$ (typically zero), the method of conjugate gradients as summarised in Shewchuk (1994) is as follows:

$$
\begin{aligned}
&n = 0 \\
&\mathbf{d}_n = \mathbf{r}_n = \mathbf{b} - \mathbf{A}\mathbf{x}_n \\
&\delta_0 = \delta_{new} = \mathbf{r}_n^T \mathbf{r}_n \\
&\text{While } n < n_{max} \text{ and } \delta_{new} > \epsilon^2 \delta_0 \\
&\quad \alpha_n = \frac{\mathbf{r}_n^T \mathbf{r}_n}{\mathbf{d}_n^T \mathbf{A}\mathbf{d}_n} \\
&\quad \mathbf{x}_{n+1} = \mathbf{x}_n + \alpha_n \mathbf{d}_n \\
&\quad \mathbf{r}_{n+1} = \mathbf{r}_n - \alpha_n \mathbf{A}\mathbf{d}_n \\
&\quad \delta_{old} = \delta_{new} \\
&\quad \delta_{new} = \mathbf{r}_{n+1}^T \mathbf{r}_{n+1} \\
&\quad \beta = \frac{\mathbf{r}_{n+1}^T \mathbf{r}_{n+1}}{\mathbf{r}_n^T \mathbf{r}_n} \\
&\quad \mathbf{d}_{n+1} = \mathbf{r}_{n+1} + \beta \mathbf{d}_n \\
&\quad n = n + 1
\end{aligned}
\tag{3.12}
$$

where $\mathbf{d}$ is the vector of search directions, $\mathbf{r}$ is the residual, n is the iteration, and ϵ is the error tolerance. When the algorithm is fully converged, i.e. the minimum has been reached, the residual is equal to zero. In practice however, the algorithm stops when the norm of the residual falls below the specified tolerance, or the maximum number of iterations, n_{max}, is reached.

For large systems, the performance of the conjugate gradient method is generally improved through use of a preconditioner. Preconditioning is a technique that improves the condition number of a matrix, which allows the solution method of the linear system under consideration to converge faster. For a system $\mathbf{A}\mathbf{x} = \mathbf{b}$, the condition number of the matrix $\mathbf{A}$ gives an indication of how accurate the solution $\mathbf{x}$ will be after approximation. It is defined as the maximum ratio of the relative error in $\mathbf{x}$ divided by the relative error in $\mathbf{b}$. Therefore if the condition number is large, i.e. the matrix is ill-conditioned, a very small error in the input data, $\mathbf{b}$, may produce a large error in the solution, $\mathbf{x}$. The preconditioned conjugate gradient method is as follows:

$$
\begin{aligned}
&n = 0 \\
&\mathbf{r}_n = \mathbf{b} - \mathbf{A}\mathbf{x}_n \\
&\mathbf{d}_n = \mathbf{M}^{-1}\mathbf{r}_n \\
&\delta_0 = \delta_{new} = \mathbf{r}_n^T \mathbf{r}_n \\
&\text{While } n < n_{max} \text{ and } \delta_{new} > \epsilon^2 \delta_0 \\
&\quad \alpha_n = \frac{\mathbf{r}_n^T \mathbf{M}^{-1} \mathbf{r}_n}{\mathbf{d}_n^T \mathbf{A} \mathbf{d}_n} \\
&\quad \mathbf{x}_{n+1} = \mathbf{x}_n + \alpha_n \mathbf{d}_n \\
&\quad \mathbf{r}_{n+1} = \mathbf{r}_n - \alpha_n \mathbf{A} \mathbf{d}_n \\
&\quad \delta_{old} = \delta_{new} \\
&\quad \delta_{new} = \mathbf{r}_{n+1}^T \mathbf{r}_{n+1} \\
&\quad \beta = \frac{\mathbf{r}_{n+1}^T \mathbf{M}^{-1} \mathbf{r}_{n+1}}{\mathbf{r}_n^T \mathbf{M}^{-1} \mathbf{r}_n} \\
&\quad \mathbf{d}_{n+1} = \mathbf{M}^{-1} \mathbf{r}_{n+1} + \beta \mathbf{d}_n \\
&\quad n = n + 1
\end{aligned}
\tag{3.13}
$$

where $\mathbf{M}$, the preconditioner, is a symmetric, positive-definite matrix that approximates $\mathbf{A}$, but is easier to invert. The preconditioner must be chosen such that the cost of computing $\mathbf{M}^{-1}\mathbf{r}$ once per iteration is more than offset by the improvement in convergence. There are many different options when choosing a preconditioner; for this work, a number of preconditioning methods were tested, including Jacobi, successive over-relaxation (SOR) and incomplete Cholesky. However, when running the model on the laptop used for this research (compiled using gfortran on a late 2011 MacBook Pro with 2.3 GHz Intel Core i5 processor), it was found that the best balance between accuracy and speed of computation for the problems under consideration was achieved without a preconditioner. Should higher performance computing resources with parallel processing be available, use of a preconditioner may facilitate longer simulations and larger computational domains.

Numerical implementation of nearly any preconditioner is a significant task if the

code is being written from scratch. Thus the PETSc library of routines is implemented in the numerical model to facilitate testing different preconditioners. PETSc, or the Portable, Extensible Toolkit for Scientific Computation, is a suite of data structures and routines for the parallel solution of partial differential equations. In this research, the PETSc routine for the conjugate gradient method is implemented. Specifying a preconditioner to use with this routine is a straightforward process and thus the range of preconditioners listed above were tested with minimal coding.

Assembling the coefficient matrix, $\mathbf{A}$, is a process that must be performed with care. The matrix must be assembled so that each entry is in the correct location corresponding to the relevant entry in the solution vector, $\mathbf{x}$. If the system is being solved using PETSc, it is very important to specify the number of non-zero entries in each row of $\mathbf{A}$. The boundary conditions must also be incorporated into $\mathbf{A}$. This process is described in more detail in the following section.

3.3.4 Boundary conditions for the Boussinesq region

For ease of numerical implementation, the dispersive terms in the Boussinesq momentum equations are dropped at the points closest to the paddles ($j = 1, 2$). It is assumed that over this short distance, the lack of dispersion is not significant. A first-order forward difference discretisation of the resulting shallow water equations is used at the paddle faces ($j = 1$), with a second-order centred difference scheme implemented one column of grid points away from the paddles in the x-direction ($j = 2$). Second-order discretisation of the full Boussinesq equation set begins at $j = 3$.

At the start of each time step, the flux in the x-direction, q_x, at the paddle faces ($j = 1$) is updated to match the paddle motion,

$$q_{x_{i,1}} = d_{i,1}(x_{p_i}(t))_t, \tag{3.14}$$

where d is the local water depth at the paddle, and $(x_{p_i}(t))_t$ is the velocity of the i^{th} paddle at the current time step. Slip conditions are assumed along the paddle faces. Therefore, the steps that result along the $j = 1$ boundary due to the motion of the paddles in the x-direction are not considered. It is assumed that the relative motion

of adjacent paddles is sufficiently small so that the assumption of slip conditions along the paddle faces does not impact the results in a significant way.

The northern and southern boundaries of the domain ($i = 1$ and $i = imax$; $j = 1, \ldots B_{switch}$), are vertical solid walls, i.e. reflecting boundaries. Since there can be no flux through the boundaries, $q_{y_{1,j}} = q_{y_{imax,j}} = 0$. Slip boundary conditions are implemented in the numerical model using 'ghost' grid points beyond the boundary, whereby

$$\begin{aligned}
&\eta_{0,j} = \eta_{2,j}, \quad q_{x0,j} = q_{x2,j}, \quad q_{y0,j} = -q_{y2,j} \\
&\eta_{-1,j} = \eta_{3,j}, \quad q_{x-1,j} = q_{x3,j}, \quad q_{y-1,j} = -q_{y3,j} \\
&\eta_{imax+1,j} = \eta_{imax-1,j}, \quad q_{ximax+1,j} = q_{ximax-1,j}, \quad q_{yimax+1,j} = -q_{yimax-1,j} \\
&\eta_{imax+2,j} = \eta_{imax-2,j}, \quad q_{ximax+2,j} = q_{ximax-2,j}, \quad q_{yimax+2,j} = -q_{yimax-2,j}
\end{aligned} \tag{3.15}$$

In cases where the whole domain is solved by the Boussinesq equations, i.e. $B_{switch} = jmax$, no flow through the eastern boundary means that $q_{xi,jmax} = 0$ for $i = 1, \ldots imax$. Here, slip boundary conditions corresponding to vertical, solid walls must also be applied where again, ghost cells are used.

$$\begin{aligned}
&\eta_{i,jmax+1} = \eta_{i,jmax-1}, \quad q_{xi,jmax+1} = -q_{xi,jmax-1}, \quad q_{yi,jmax+1} = q_{yi,jmax-1} \\
&\eta_{i,jmax+2} = \eta_{i,jmax-2}, \quad q_{xi,jmax+2} = -q_{xi,jmax-2}, \quad q_{yi,jmax+2} = q_{yi,jmax-2}
\end{aligned} \tag{3.16}$$

Two rows of ghost cells are required in the Boussinesq domain to deal with the 5 point stencil of the third-order derivatives.

The boundary conditions in the Boussinesq domain are dealt with in the coefficient matrix **A** described in the previous section. For example, where reflective conditions apply along the northern boundary of the domain (at $i = 1$), the coefficients calculated at points where $i = 0$ are incorporated into the matrix by subtracting them from the coefficients calculated at $i = 2$. Slip conditions are applied by adding the coefficients calculated at $i = 0$ to those calculated at $i = 2$.

3.4 Numerical implementation of the nonlinear shallow water equations

3.4.1 Finite volume solver

The nonlinear shallow water equations are used to model the broken waves propagating as bores as well as being implemented in areas of shallow water ($h/\lambda < 0.05$, where h is the water depth and λ is the wavelength). Thus a numerical scheme with shock-capturing capabilities is necessary to evolve the resulting discontinuous, steep-fronted flows. When discontinuities are present, the derivatives approximated by finite difference methods cannot be calculated. Hence, a finite volume method is used, which is based on the integral form of (2.45), given by

$$\frac{\partial}{\partial t}\int_{\Omega}\mathbf{u}\,\mathrm{d}\Omega+\int_{\Omega}\left(\frac{\partial\mathbf{f}}{\partial x}+\frac{\partial\mathbf{g}}{\partial y}\right)\mathrm{d}\Omega=\int_{\Omega}\mathbf{s}\,\mathrm{d}\Omega \tag{3.17}$$

where $\mathbf{u}$, $\mathbf{f}$, $\mathbf{g}$ and $\mathbf{s}$ are given by (2.46) and Ω represents the volume element. In this thesis, the Godunov-type finite volume solver outlined by Liang and Borthwick (2009) is used, with an HLLC approximate Riemann solver used to evaluate the fluxes across the interfaces between volumes where discontinuities might be present. The three-wave HLLC solver is a modification of the two-wave HLL scheme, whereby the missing contact and shear waves are restored. Godunov, or upwind methods, use wave propagation information to construct the numerical scheme. The solver operates on a regular grid, with the coordinates of the centres of the grid cells or volumes given by (x_j, y_i) for $j = B_{switch}+1, \ldots B$ and $i = 1, \ldots imax$. In this scheme, the time-marching formula is given by

$$\mathbf{u}_{i,j}^{n+1}=\mathbf{u}_{i,j}^{n}-\frac{\Delta t}{\Delta x}(\mathbf{f}_E-\mathbf{f}_W)-\frac{\Delta t}{\Delta y}(\mathbf{g}_N-\mathbf{g}_S)+\Delta t\mathbf{s}_{i,j} \tag{3.18}$$

where the subscript i, j refers to the cell index, the superscript n represents the time level, Δt is the time step, Δx and Δy are the grid spacings, and $\mathbf{f}_E$, $\mathbf{f}_W$, $\mathbf{g}_N$ and $\mathbf{g}_S$ are the fluxes through east, west, north and south faces respectively of each cell.

Figure 3.4 shows the structure of the solution of the Riemann problem in the x-direction, which contains left and right waves as well as a middle, or shear wave. When

considering the x-direction Riemann problem, the shear wave arises from the presence of the y-direction momentum equation. On either side of the shear wave, the tangential velocity component, v, changes discontinuously (v_L and v_R), while the normal velocity component, $u*$, and the water depth, $d*$, remain constant. At the eastern face of a cell for example, the fluxes, $\mathbf{f}_E$ are given by

$$\mathbf{f}_E = \begin{cases} \mathbf{f}_L & \text{if } 0 \leq S_L, \\ \mathbf{f}_{*L} & \text{if } S_L < 0 < S_M, \\ \mathbf{f}_{*R} & \text{if } S_M \leq 0 < S_R, \\ \mathbf{f}_R & \text{if } 0 \geq S_R \end{cases} \tag{3.19}$$

where $\mathbf{f}_L = \mathbf{f}(\mathbf{u}_L)$ and $\mathbf{f}_R = \mathbf{f}(\mathbf{u}_R)$ are calculated from the left and right Riemann states, $\mathbf{u}_L$ and $\mathbf{u}_R$, existing at the eastern face. The values of $\mathbf{u}_L$ and $\mathbf{u}_R$ are calculated from the central values of the flow variables using a piece-wise linear reconstruction, described more fully in the next section. The fluxes $\mathbf{f}_{*L}$ and $\mathbf{f}_{*R}$ are the left and right sides of the middle wave, and are given by

$$\mathbf{f}_{*L} = \begin{bmatrix} f_{*1} \\ f_{*2} \\ v_L f_{*1} \end{bmatrix}, \quad \text{and} \quad \mathbf{f}_{*R} = \begin{bmatrix} f_{*1} \\ f_{*2} \\ v_R f_{*1} \end{bmatrix}. \tag{3.20}$$

where v_L and v_R are the left and right tangential velocity components which also apply across the left and right waves respectively. The fluxes, $\mathbf{f}_*$ are calculated from

$$\mathbf{f}_* = \frac{S_R \mathbf{f}_L - S_L \mathbf{f}_R + S_L S_R (\mathbf{u}_R - \mathbf{u}_R)}{S_R - S_L} \tag{3.21}$$

which is the HLL formula proposed by Harten, Lax and van Leer Harten et al. (1983).

S_L and S_R, the speeds of the left and right waves respectively are determined from

$$S_L = \begin{cases} u_R - 2\sqrt{g d_R} & \text{if } d_L = 0 \\ \min(u_L - \sqrt{g d_L}, u_* - \sqrt{g d_*}) & \text{if } d_L < 0 \end{cases} \tag{3.22}$$

and

$$S_R = \begin{cases} u_L + 2\sqrt{g d_L} & \text{if } d_R = 0 \\ \max(u_R + \sqrt{g d_R}, u_* + \sqrt{g d_*}) & \text{if } d_R < 0 \end{cases} \tag{3.23}$$

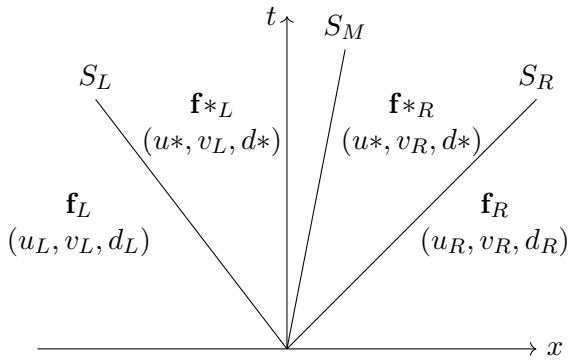

Figure 3.4: HLLC solution structure of a Riemann problem in the x-direction

where u_L, u_R, d_L and d_R are the left and right Riemann states at the cell interface under consideration. These wave speed estimates, proposed by Fraccarollo and Toro (1995) are valid for dry bed scenarios. u_* and d_* are given by

$$u_* = \frac{1}{2}(u_L + u_R) + \sqrt{gd_L} - \sqrt{gd_R} \tag{3.24}$$

and

$$h_* = \frac{1}{g}\left[\frac{1}{2}(\sqrt{gd_L} + \sqrt{gd_R}) + \frac{1}{4}(u_L - u_R)\right]^2 \tag{3.25}$$

The middle wave speed, S_M is then calculated from

$$S_M = \frac{S_L d_R(u_R - S_R) - S_R d_L(u_L - S_L)}{d_R(u_R - S_R) - d_L(u_L - S_L)}. \tag{3.26}$$

A similar calculation procedure is followed to determine $\mathbf{f}_W$, $\mathbf{g}_N$ and $\mathbf{g}_S$.

Slope limiter

Linear interpolation between the cell centre values of the conserved variables is used to calculate the values at the mid-points of the cell interfaces, with east and north taken as positive in the x and y-directions respectively. A slope limiter is implemented to improve the estimates of the cell face values by preventing numerical oscillations of the solution in the vicinity of steep gradients or jumps in the solution. The west and east face values for cell i, j are thus calculated from

$$\mathbf{u}_W^n = \mathbf{u}_{i,j}^n - \frac{1}{2}\Psi(r)(\mathbf{u}_{i,j}^n - \mathbf{u}_{i,j-1}^n), \quad \mathbf{u}_E^n = \mathbf{u}_{i,j}^n + \frac{1}{2}\Psi(r)(\mathbf{u}_{i,j}^n - \mathbf{u}_{i,j-1}^n) \tag{3.27}$$

where $\Psi(r)$ represents the slope limiter. The min-mod limiter used by Liang and Borthwick (2009) has been implemented and is given by

$$\Psi(r) = \max(0, \min(r, 1)); \tag{3.28}$$

where r represents the gradient ratios, defined for the three conserved variables in the x-direction as:

$$r = \frac{\eta_{i,j+1} - \eta_{i,j}}{\eta_{i,j} - \eta_{i,j-1}}, \quad r = \frac{q_{xi,j+1} - q_{xi,j}}{q_{xi,j} - q_{xi,j-1}}, \quad r = \frac{q_{yi,j+1} - q_{yi,j}}{q_{yi,j} - q_{yi,j-1}}. \tag{3.29}$$

A similar approach is taken in the y-direction, using information from the cells to the north and south of the current cell.

3.4.2 Time integration for the shallow water equations

The MUSCL-Hancock predictor-corrector method is adopted to integrate the equations forward in time. This method achieves second-order accuracy in time and space and consists of the following steps:

1. Face data reconstruction: Linear interpolation with a slope limiter applied to the conserved variables to determine the face values for each cell, i.e.,

$$\mathbf{u}_W^n = \mathbf{u}_{i,j}^n - \frac{1}{2}\Psi(r)(\mathbf{u}_{i,j}^n - \mathbf{u}_W^n), \quad \mathbf{u}_E^n = \mathbf{u}_{i,j}^n + \frac{1}{2}\Psi(r)(\mathbf{u}_{i,j}^n - \mathbf{u}_W^n),$$
$$\mathbf{u}_S^n = \mathbf{u}_{i,j}^n - \frac{1}{2}\Psi(r)(\mathbf{u}_{i,j}^n - \mathbf{u}_S^n), \quad \mathbf{u}_N^n = \mathbf{u}_{i,j}^n + \frac{1}{2}\Psi(r)(\mathbf{u}_{i,j}^n - \mathbf{u}_S^n),$$

2. Predictor step: The face values of $\mathbf{u}$ are updated over half a time step, i.e. at the west face of the current cell:

$$\mathbf{u}_W^{n+1/2} = \mathbf{u}_W^n - \frac{1}{2}\frac{\Delta t}{\Delta x}(\mathbf{f}_E - \mathbf{f}_W) - \frac{1}{2}\frac{\Delta t}{\Delta y}(\mathbf{g}_N - \mathbf{g}_S) + \frac{1}{2}\Delta t \mathbf{s}_{i,j},$$

   and similarly for $\mathbf{u}_E$, $\mathbf{u}_S$ and $\mathbf{u}_N$.

3. Corrector step: The HLLC approximate Riemann solver given by equations 3.19 to 3.26 is applied to calculate the fluxes through the cell interfaces. The left and right Riemann states of the western face of cell i, j, for example, are given by the values calculated in the predictor step:

$$\mathbf{u}_{W\,i,j}^L = \mathbf{u}_{E\,i,j-1}^{n+1/2} \quad \text{and} \quad \mathbf{u}_{W\,i,j}^R = \mathbf{u}_{W\,i,j}^{n+1/2}$$

The updating formula 3.18 is then implemented to give the new cell-averaged values of the conserved variables, $\mathbf{u}$.

3.4.3 Boundary conditions for the shallow water equations

If the eastern end of the basin is inundated, and the nonlinear shallow water equations are applied in this region, ghost cells are utilised beyond the eastern wall of the tank in a similar way as in the Boussinesq region. Given that the conserved variables are calculated at the cell centres in the finite volume solver, the eastern boundary of the basin exists at the interface between cells, giving rise to the boundary conditions

$$\eta_{i,jmax+1} = \eta_{i,jmax}, \quad q_{xi,jmax+1} = -q_{xi,jmax}, \quad q_{y_{i,jmax+1}} = q_{y_{i,jmax}}. \tag{3.30}$$

Similarly, the boundary conditions for the southern and northern boundaries of the shallow water domain are given by

$$\begin{aligned} &\eta_{0,j} = \eta_{1,j}, \quad q_{x0,j} = q_{x1,j}, \quad q_{y0,j} = -q_{y1,j} \\ &\eta_{imax+1,j} = \eta_{imax,j}, \quad q_{ximax+1,j} = q_{ximax,j}, \quad q_{y_{imax+1,j}} = -q_{y_{imax,j}} \end{aligned} \tag{3.31}$$

where $j = B_{switch+1}, \ldots B$.

Wetting and drying

In simulations where a wet/dry front exists towards the eastern end of the basin, the approach to wetting and drying described by Brufau et al. (2002) is used, whereby the local bed slope is modified to avoid spurious flow in dry cells. In general, dry cells are excluded from the computational domain unless they are about to be flooded, i.e., if a cell is dry but has a bed level below that of a wet neighbour. The moving shoreline is thus automatically tracked by the finite volume solver. Figure 3.5 illustrates the possible scenarios at the wet-dry front. In Figure 3.5(a), a wet cell is adjacent to a dry cell, where $d_L \neq 0$, $d_R = 0$ and $\eta_R = z_{bR} > \eta_L$. In this case, there is no flow through the interface between the cells. However, as $\eta_L \neq \eta_R$, the following modifications must be made to avoid the prediction of a non-physical flux:

$$\eta'_R = \eta_R - \Delta\eta \quad \text{and} \quad z_b{}'_R = \eta'_R \tag{3.32}$$

where $\Delta\eta = \eta_R - \eta_L$. In the wet cell, the velocity component normal to the wet-dry interface is set to zero to ensure no flow through the boundary. In Figure 3.5(b), $\eta_R = z_{bR} \leq \eta_L$, i.e. the bed elevation of the right hand dry cell is below the water level in the adjacent wet cell. In this case, water will flood the dry cell, and modification of the bed slope is unnecessary. In the case of two adjacent dry cells with different bed levels, as shown in Figure 3.5(c), a bed modification similar to that carried out in case (a) is applied, to prevent the numerical model predicting a spurious flux through the dry-dry interface.

To increase the stability of the model, any cell with a water depth less than the critical value (1mm) is automatically dried out and the fluxes set to zero. The small amount of water that was present is added to a wet adjacent cell to ensure mass conservation. In some cases, for example when the slope is steep, the model may predict that more water than is actually available will flow out of the current cell, causing a negative water depth. In this situation, the depth is set to zero and water is subtracted from the adjacent cell containing the most water, again ensuring mass is conserved. In both cases, the fluxes, q_x and q_y in the adjacent cell are adjusted to ensure the velocities remain the same as before.

3.5 Interface between the Boussinesq and shallow water domains

The switch from the Boussinesq to the shallow water equations occurs either to allow shoaling waves to break, or by considering the dispersion/shallowness parameter μ, defined as $\mu = \frac{h}{\lambda}$, where h is the water depth and λ is the wavelength. As the shallow water equations are non-dispersive, they are implemented in all areas where $\mu \leq \frac{1}{20}$, i.e. where dispersive effects are negligible. Bellotti and Brocchini (2002) show that dispersive contributions of $O(\mu^2)$ in Boussinesq-type equations disappear in the swash zone. Thus, as the shallow water equations are a subset of the Boussinesq equations, their use in this region is mathematically consistent. When the switch between equation sets occurs to allow wave breaking, it is triggered by a breaking criterion based on the

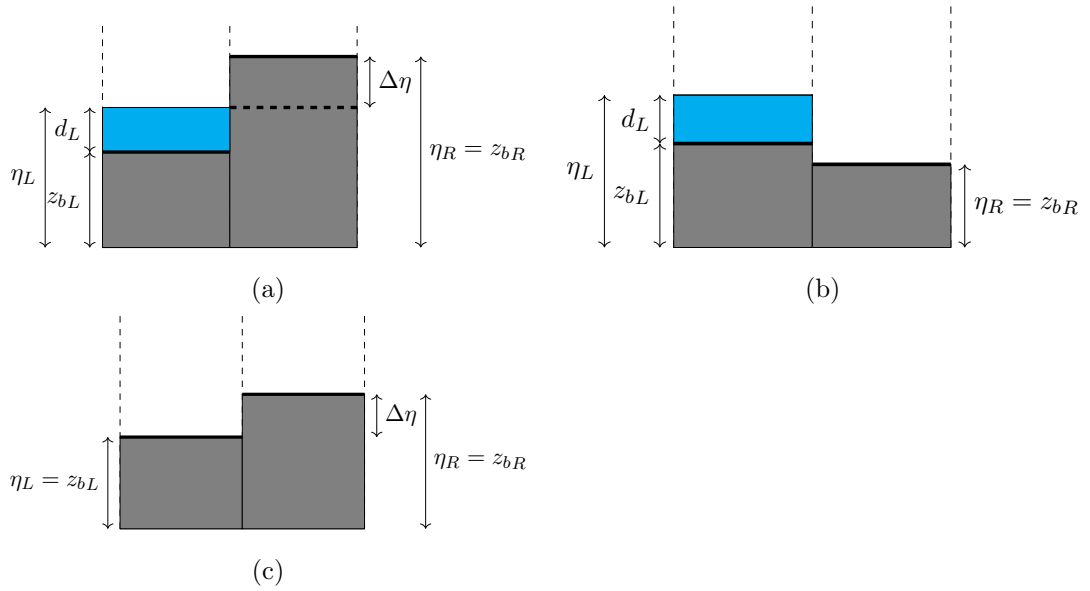

Figure 3.5: Local bed slope modification at the wet/dry front: (a) $d_L \neq 0$, $d_R = 0$ and $\eta_R = z_{bR} \geq \eta_L$; (b) $d_L \neq 0$, $d_R = 0$ and $\eta_R = z_{bR} \leq \eta_L$; (c) $d_L = 0$, $d_R = 0$.

local calculation of the magnitude of the free-surface slope, i.e.

$$\Theta = \sqrt{\left(\frac{\partial \eta}{\partial x}\right)^2 + \left(\frac{\partial \eta}{\partial y}\right)^2}. \tag{3.33}$$

This calculation is performed at all points in the Boussinesq domain at the beginning of every time step. The most offshore point where $\Theta \geq 0.4$, (approximately 22°) determines the breaking location. Following Orszaghova (2011), the switch point between equation sets, $x_{Bswitch}$, is located a quarter wavelength offshore of this point. The wavelength is estimated by a down-crossing method carried out in the x-direction, as waves are predominantly travelling in this direction.

To ensure a smooth transition, the dispersive terms of the Boussinesq equations given in (2.47) are gradually ramped down over half a wavelength so that they have fully disappeared by $x_{Bswitch}$. The ramping function is given by

$$f_{ramp} = \begin{cases} 1 & x < r_s, \\ \cos^2\left(\dfrac{\pi}{2}\dfrac{x - r_s}{x_{Bswitch} - r_s}\right) & r_s \leq x \leq x_{Bswitch}, \end{cases} \tag{3.34}$$

and is applied to all dispersive terms in the ramping zone. r_s denotes the x-coordinate of the starting point of this zone, which is located half a wavelength offshore of $x_{Bswitch}$

in the x-direction. The ramping zone is applied uniformly across the basin in the y-direction. Thus, all dispersive terms have disappeared by $x_{Bswitch}$ and the shallow water equations are solved onshore of this point. While this may appear to be an overly simplistic approach for a model that operates in two horizontal dimensions, it is sufficiently accurate for waves approaching the shore at a reasonably shallow angle ($\leq 30°$). A more sophisticated breaking criterion warrants further research.

Where the switch between the Boussinesq and shallow water regions exists, an adjustment must be made to the Boussinesq solver at the interface. In stage 4 of the RK4 algorithm, the calculation of the gradients of η, q_x and q_y at $x_{Bswitch}$ requires a five-point stencil of information in the x and y-direction. Therefore the stencil extends 2 points in the x-direction into the shallow water domain. Working the data requirements back to stage 1 of the RK4 algorithm, data extending to $x_{Bswitch+8}$ are required by the Boussinesq solver. These data are simply provided by solving the shallow water equations where $x_{Bswitch+1} \leq x \leq x_{Bswitch+8}$. In the coefficient matrix $\mathbf{A}$, the main diagonal entries for these data from the shallow water region, $A_{i,j}$ where $i = j$, are set to unity, and all corresponding off-diagonal entries are set to zero.

3.6 Model stability

3.6.1 Smoothing of the updated solution

A feature of iterative solvers such as the conjugate gradient method, is the accumulation of floating point error in the solution. These errors can grow rapidly and lead to saw-tooth instabilities that result in the model crashing. To mitigate against these instabilities, as well as the accumulation of error due to the first-order discretisation used at the paddle face, numerical smoothing is applied in the moving paddle domain. This takes the form of a 5-point filter applied in the y-direction. It is given by

$$\eta_{i,j}^{smooth} = \frac{1}{20}\big(\eta_{i-2,j} + 4\eta_{i-1,j} + 10\eta_{i,j} + 4\eta_{i+1,j} + \eta_{i+2,j}\big), \tag{3.35}$$

where $\eta_{i,j}^{smooth}$ represents the smoothed value of η at each grid point in the moving paddle domain, calculated using the updated values of η at the end of every time step. The same filter is applied to the fluxes q_x and q_y. Applying a filter in this way also

minimises the potential for instability due to the assumption of slip conditions at the paddle faces described in Section 3.3.4.

3.6.2 The CFL condition

The Courant-Friedrichs-Lewy (CFL) condition is an important consideration in the solution of partial differential equations by finite differences. To compute the amplitude of a wave travelling across a spatial grid using a numerical model, the time step of the model must be less than the time it takes the wave to travel between adjacent grid points. In other words, the numerical domain of dependence must contain the physical domain of dependence to ensure stability and the correct propagation of information. Thus, when the grid size is reduced, the upper limit for the time step also decreases. In the present model, the Courant number is calculated from

$$C = \frac{\left(\sqrt{u^2 + v^2} + \sqrt{gh}\right) \Delta t}{\sqrt{\Delta x^2 + \Delta y^2}} \tag{3.36}$$

C typically has a maximum value of $C_{\max} = 1$, although this value depends on the solution method being applied. The above calculation of the Courant number is used as a guide during model testing as it gives an indication of when the model is becoming unstable. Depending on the type of simulation being carried out, the numerical model tends to perform best when $C \approx 0.3 - 0.6$.

3.7 Chapter summary

- This chapter describes the numerical implementation of the 2DH model. The grid deformation caused by the moving paddles is dealt with in the numerical model through the adoption of a domain mapping technique, which maps the moving physical domain in the region of the paddles onto a fixed computational domain. This avoids remeshing at every time-step and makes the solution of the governing equations a more straight-forward process.

- The Boussinesq equations are discretised using second-order finite differences, solved using the conjugate-gradient method, and integrated forward in time using

a fourth-order Runge-Kutta algorithm. The nonlinear shallow water equations are solved using a finite volume method, with an HLLC approximate Riemann solver used to evaluate fluxes across the interfaces between volumes. Implementation of the MUSCL-Hancock method achieves second-order accuracy in time and space.

- The motion of the shoreline front is automatically tracked by the finite volume solver. Dry cells are excluded from the computational domain unless they are about to be flooded. At the wet/dry front, the local bed slope is temporarily adjusted, to prevent the generation of spurious flows between cells.

- Wave breaking is approximated by switching from the Boussinesq to the nonlinear shallow water equations. The switch point is determined by the magnitude of the slope of the water surface. The dispersive terms of the Boussinesq equations are ramped down approaching the switch point to ensure an smooth transition between equation sets.

- Slip boundary conditions are implemented in the numerical model, with no flow through the solid boundaries.

Chapter 4

Model verification tests

In this chapter, different aspects of the numerical model are verified by considering analytical solutions to benchmark problems. The evolution of a symmetric wave in a closed basin verifies the correct handling of the cross-derivative terms in the Boussinesq equation set. This test also allows comparisons to be made between the nonlinear behaviour of the numerical model and the linear analytical solution. The shallow water solver with its in-built wetting and drying algorithm is verified using the analytical case of sloshing in a parabolic basin. A more robust test of the two-dimensional wetting and drying algorithm is provided by the propagation of a dam break wave over a flood plain with three conical hills. The paddle signal for a solitary wave is calculated and used to test the correct implementation of the numerical piston paddle.

4.1 Evolution of sloshing waves in a closed basin

The evolution of symmetric sloshing waves in a closed square basin is considered to test the stability of the model and to verify the correct handling of the cross-derivative terms. The test has also been considered by other researchers to verify numerical models, including Wei and Kirby (1995) and Jalali and Borthwick (2017). The symmetric wave is of the form of an initial 'hump' of water shown in Figure 4.1. It is defined as a

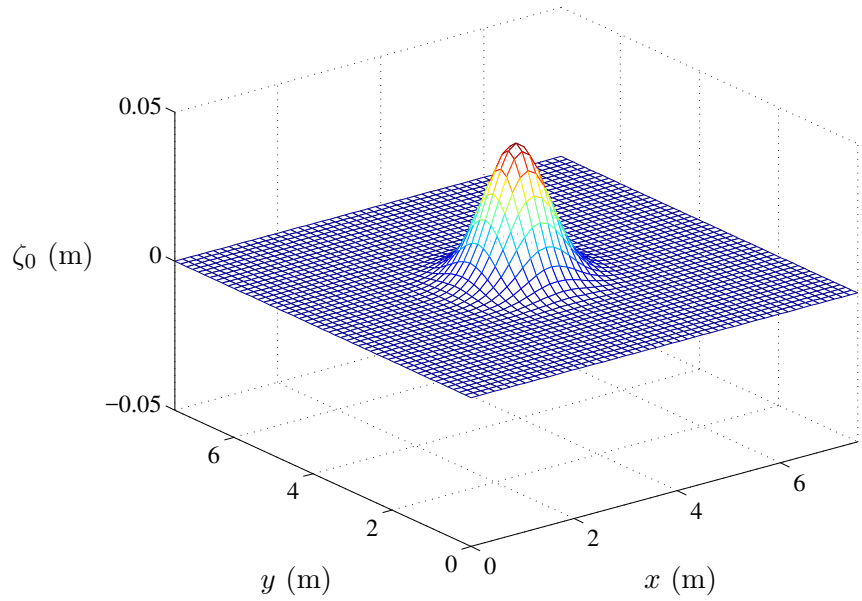

Figure 4.1: Evolution of a Gaussian hump in a closed basin: initial symmetric disturbance at $t = 0$ s

two-dimensional Gaussian surface, described by the equation

$$\zeta_0(x, y) = H_0 \exp\left[-b\left(\left(x - \frac{L_x}{2})^2 + (y - \frac{L_y}{2}\right)^2\right]\right] \tag{4.1}$$

where ζ_0 is the initial super-elevation of the water surface above an underlying still water depth h, L_x and L_y are the basin dimensions in the x and y-directions respectively, b is a spreading parameter and H_0 is the initial maximum super-elevation.

The basin under consideration has dimensions $L_x = L_y = 7.5$ m, has a flat, frictionless bottom, and is bounded by vertical, reflective walls on all four sides. The still water depth $h = 0.45$ m, the hump amplitude $H_0 = 0.045$ m and the spreading parameter $b = 2$ m. Wei and Kirby (1995) present the derivation of a linear analytical solution, where the tank domain $0 \leq x \leq L_x, 0 \leq y \leq L_y$, is extended in both the x and y directions, leading to a waveform that is periodic over $2L_x$ and $2L_y$. The solution at any individual point in the tank at time t with spatial coordinates (x, y) is given by

$$\zeta(x, y, t) = \sum_{n=0}^{\infty}\sum_{m=0}^{\infty} \tilde{\zeta}_{nm} \mathrm{e}^{-i\omega_{nm}t} \cos(n\lambda x)\cos(m\lambda y). \tag{4.2}$$

In the above formula, the amplitude $\tilde{\zeta}_{nm}$ of the n, m-th mode component is given by

the expression

$$\tilde{\zeta}_{nm} = \frac{4}{(1+\delta_{n0})(1+\delta_{m0})L_x L_y} \int_{-L_x}^{L_x} \int_{-L_y}^{L_y} \zeta_0(x,y)\cos(n\lambda x)\cos(m\lambda y)\,\mathrm{d}x\mathrm{d}y, \qquad (4.3)$$

where (n, m) are the wave modes, δ_{nm} is the Kronecker delta function, and the wavelength, $\lambda = \pi/L_x = \pi/L_y$. Each of the (m, n) modes of the waveform has a natural angular frequency, ω_{nm}, given by the dispersion equation, $\omega_{nm}^2 = gk_{nm}\tanh(k_{nm}h)$, where the wavenumber, k_{nm}, is given by $k_{nm} = \sqrt{(n\lambda)^2 + (m\lambda)^2}$.

Using a grid resolution of $\Delta x = \Delta y = 0.0375$ m and a time step, $\Delta t = 0.05$ s, the model is run for 100 s. Both the bed friction coefficient C_f, and the eddy viscosity parameter ε, are set to zero. Grid convergence is tested by considering increasingly high resolution grids, starting with $\Delta x = \Delta y = 0.15$ m (51 grid points in each direction). Visual inspection of the contour plots in Figures 4.6 and 4.7 shows that convergence is achieved with a grid spacing of 0.0375 m. Increasing the resolution beyond this does not yield a significantly more accurate solution, whereas the computation time slows considerably. As expected, the waveform propagates outwards in a circular fashion, as illustrated in Figure 4.2, demonstrating the correct handling of the cross-derivative terms. Figure 4.3 presents visualisations of the water surface at $t = 25, 50, 75$, and 100 s.

Figure 4.4 provides comparisons between the nonlinear numerical prediction and the linear analytical solution of the free-surface time histories, given by Equation (4.2), at the centre and corner of the tank. The analytical solution is generated by considering 51 wave components in the x- and y-directions (i.e. $m = n = 51$). Overall, there is very close agreement between the numerical and analytical solutions, particularly in the early stages of the wave evolution. As the simulation progresses, the nonlinear properties of the Boussinesq numerical model result in a very gradual phase shift, with discrepancies emerging in the amplitude of the peaks and troughs.

The same amplitude initial hump is again considered ($H_0 = 0.045$ m), but in a rectangular as opposed to a square basin of dimensions $L_x = 15$ m and $L_y = 7.5$ m. Again the grid resolution is set to $\Delta x = \Delta y = 0.0375$ m, the time step is $\Delta t = 0.05$ s and the model is run for 100 s. Figure 4.5 presents visualisations of the water surface at $t = 3$, 4, 25, 50, 75 and 100 s. As the hump is released, the generated radial

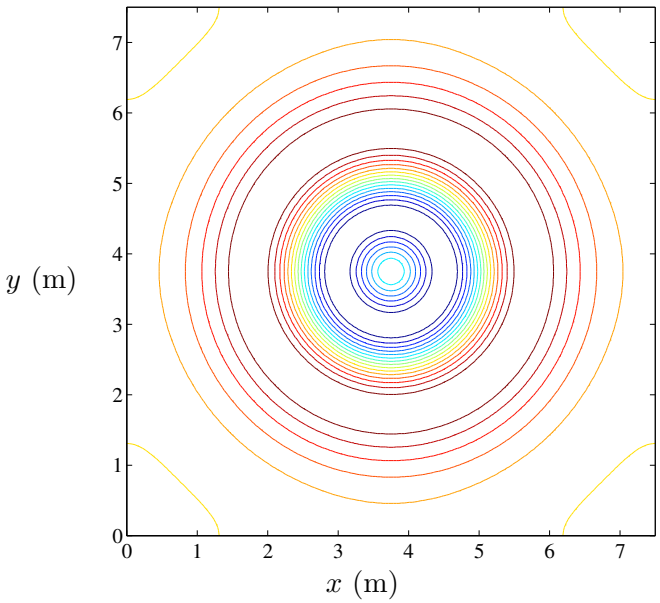

Figure 4.2: Evolution of a Gaussian hump in a closed basin: initial ζ-contours at $t = 1$ s

wave reflects off the north and south walls of the basin before it reaches the eastern and western boundaries. The reflected and radial waves combine and travel along the northern and southern boundary walls. By $t = 4$ s, a wave pattern develops that is dominated by longitudinal and transverse sloshing modes, which becomes increasingly complicated as the simulation progresses.

4.1.1 Grid convergence

Grid convergence is assessed numerically by calculating the evolution of the free surface on progressively finer grids and comparing the results. Four different grids are considered, where $\Delta x = \Delta y = 0.15$ m is the coarsest ($imax = jmax = 51$), and $\Delta x = \Delta y = 0.01875$ m ($imax = jmax = 401$) is the finest. For each grid refinement, both the grid resolution and the time step is reduced by a factor of 2 in order to keep the Courant number constant. The error $\mathbf{E}$ associated with each grid resolution is calculated by comparing the free surface profile at $t = 50$ s at each point on the grid to

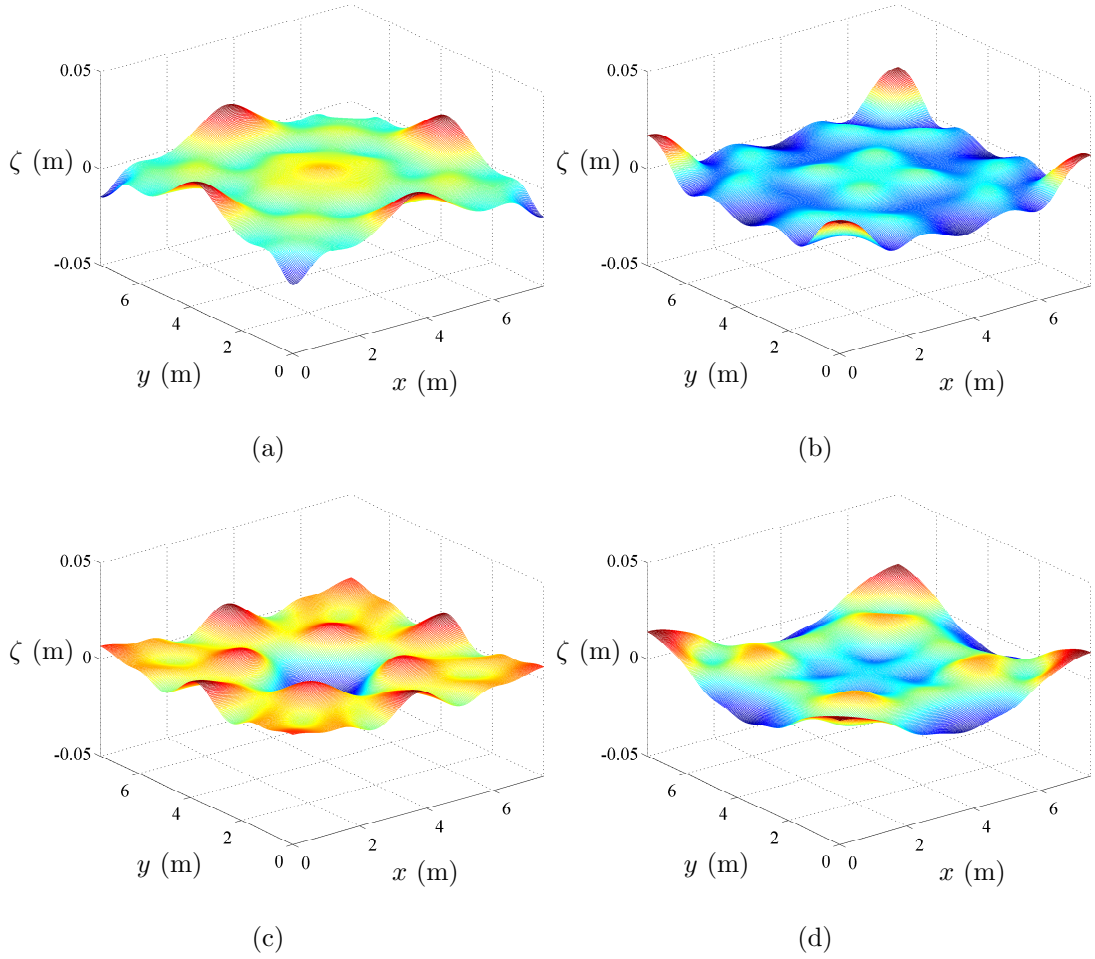

Figure 4.3: Evolution of initial Gaussian hump in a closed basin: numerically predicted free-surface elevation visualisations at: (a) $t = 25$ s; (b) $t = 50$ s; (c) $t = 75$ s; and (d) $t = 100$s.

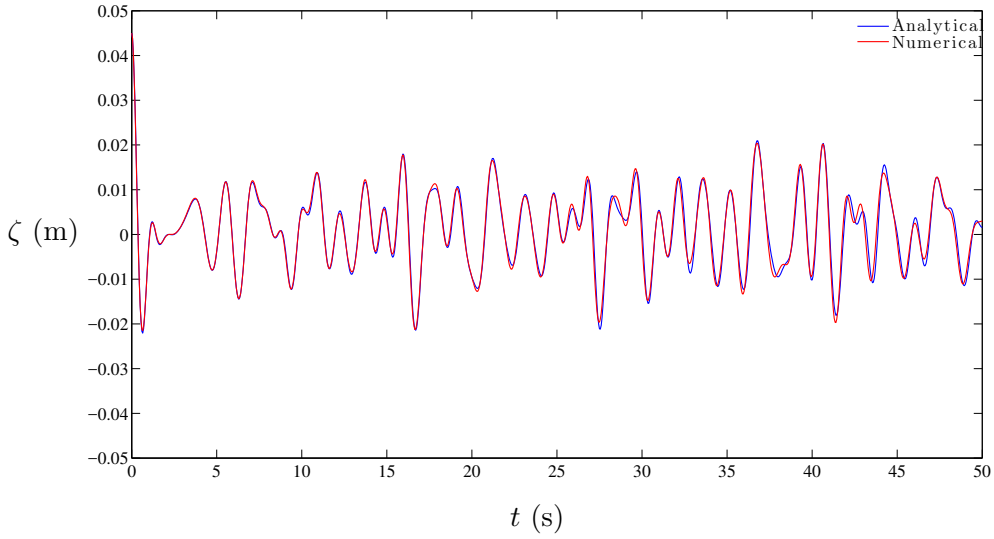

(a)

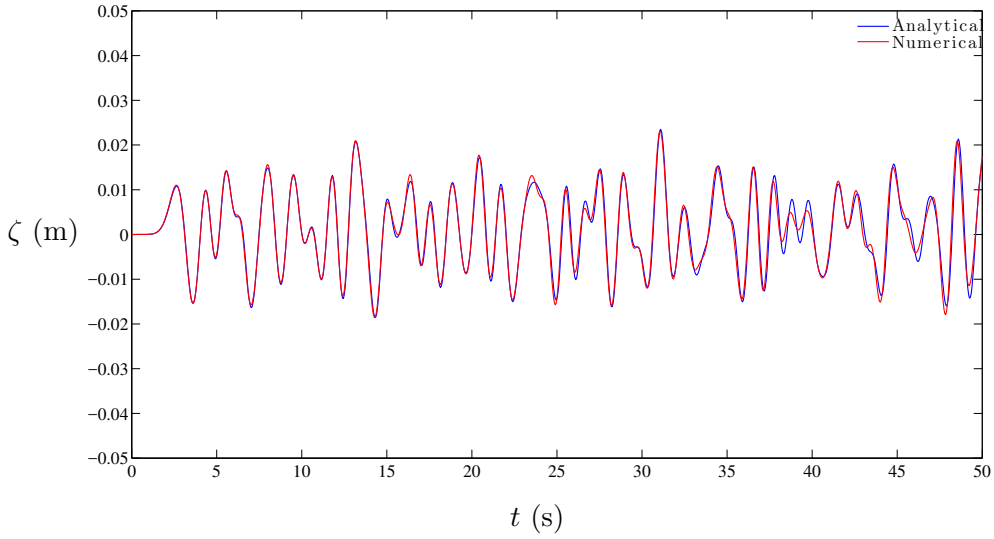

(b)

Figure 4.4: Evolution of initial Gaussian hump in a closed basin: comparison between the numerical prediction and the analytical solution of the free-surface elevation time series at (a) the basin centre point; (b) the basin corner.

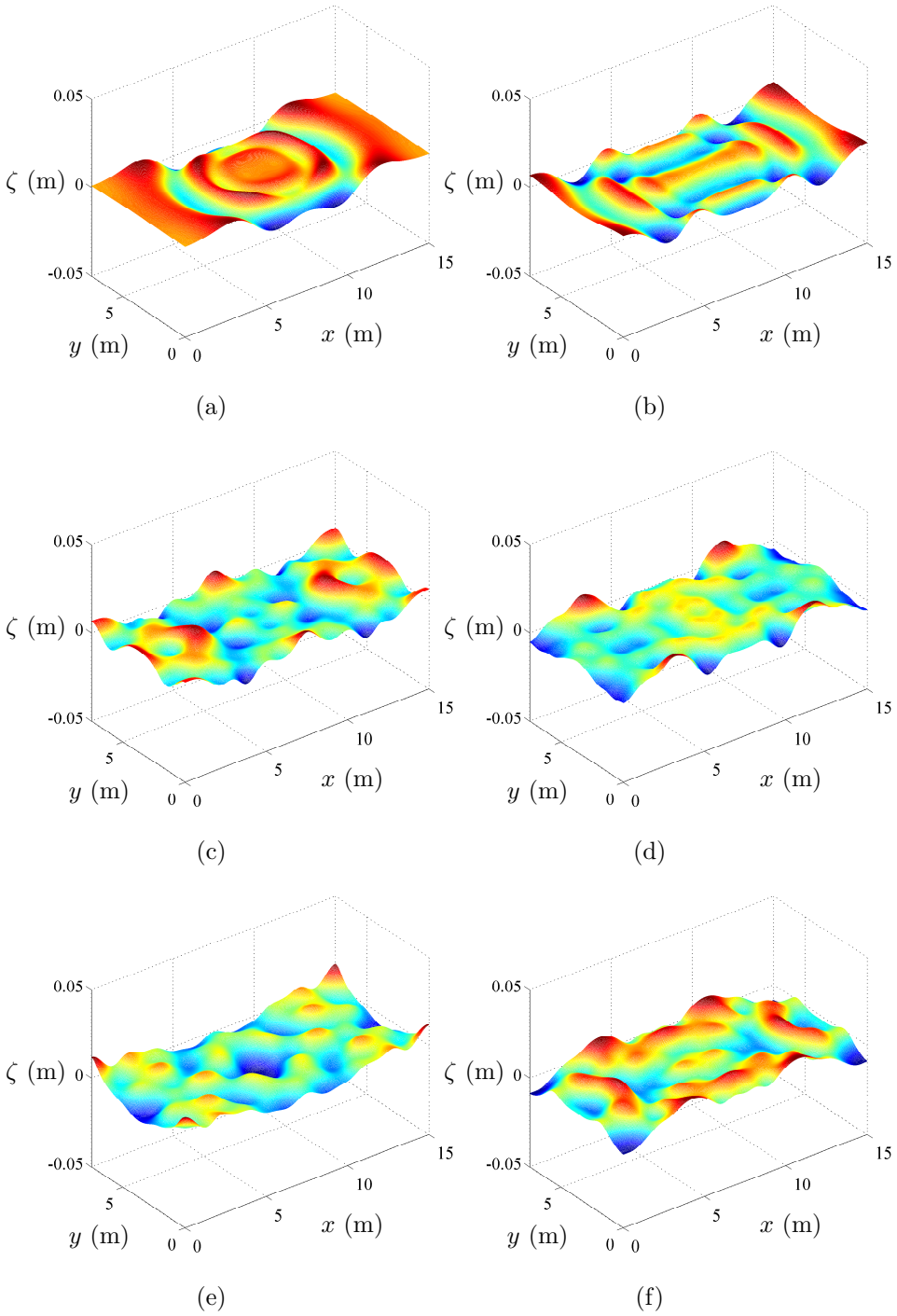

Figure 4.5: Evolution of initial Gaussian hump in a closed rectangular basin: numerically predicted free-surface elevation visualisations at: (a) $t = 3$ s; (b) $t = 4$ s; (c) $t = 25$ s; (d) $t = 50$ s; (e) $t = 75$ s; and (f) $t = 100$s.

$\Delta x = \Delta y$	Δt	$\|\|\mathbf{E}\|\|_2$	c_r	$\|\|\mathbf{E}\|\|_F$	c_r
0.015	0.20	0.0545	-	0.2236	-
0.075	0.10	0.0235	1.2115	0.1191	0.9091
0.0375	0.05	0.0066	1.8277	0.0320	1.8972
0.01875	0.025	0	-	0	-

Table 4.1: Error and convergence rate calculation of the numerical model at $t = 50$ s using the Gaussian hump test

the corresponding point on finest grid, giving

$$\mathbf{E} = \boldsymbol{\eta}_{coarse} - \boldsymbol{\eta}_{finest}. \tag{4.4}$$

The size of the error is determined by calculating both the L^2-norm along the diagonal of the basin, given by

$$||\mathbf{E}||_2 = \sqrt{|E_{1,1}|^2 + |E_{2,2}|^2 + \cdots + |E_{imax,jmax}|^2}, \tag{4.5}$$

and the Frobenius, or matrix norm, given by

$$||\mathbf{E}||_F = \sqrt{\sum_{i=1}^{imax} \sum_{j=1}^{jmax} |E_{ij}|^2}. \tag{4.6}$$

The convergence rate c_r is then calculated from

$$c_r = \frac{\ln(||\mathbf{E}_{fine}||) - \ln(||\mathbf{E}_{coarse}||)}{\ln(\Delta x_{fine}) - \ln(\Delta x_{coarse})}. \tag{4.7}$$

The calculated errors and associated convergence rates are given in Table 4.1. The table shows that for each grid refinement, the error reduces.

Figures 4.6 and 4.7 present contour plots at $t = 4$ and 10 s respectively for different grid resolutions.

4.1.2 Reversibility check

The reversibility of the Boussinesq model is verified by running the Gaussian hump simulation for 50 s, at which point the sign of the time step is changed and the simulation

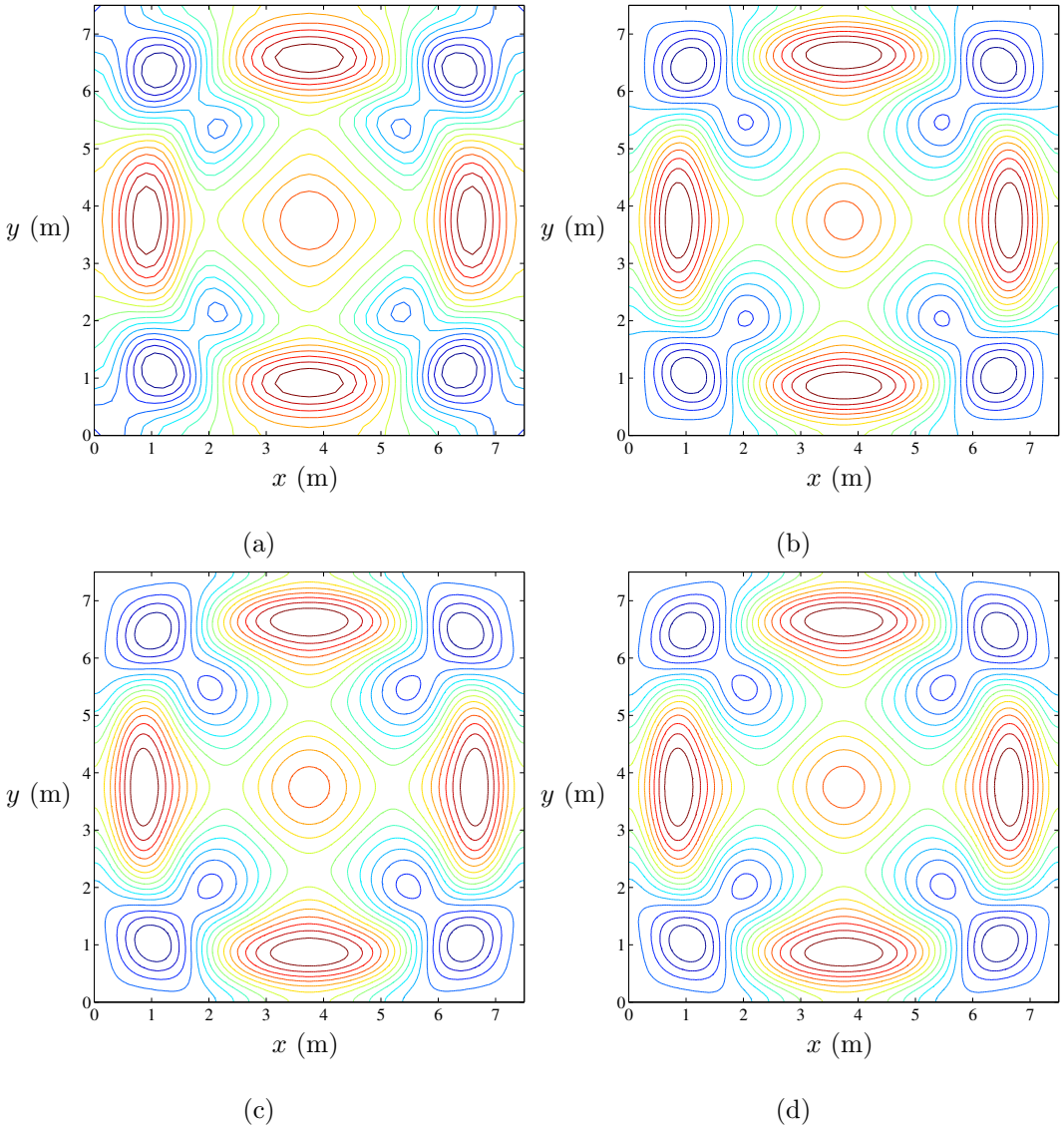

Figure 4.6: Evolution of initial Gaussian hump in a closed basin: numerically predicted free-surface elevation contours at $t = 4$ s for: (a) $\Delta x = \Delta y = 0.15$m; (b) $\Delta x = \Delta y = 0.075$m (c) $\Delta x = \Delta y = 0.0375$m; and (d) $\Delta x = \Delta y = 0.03$m.

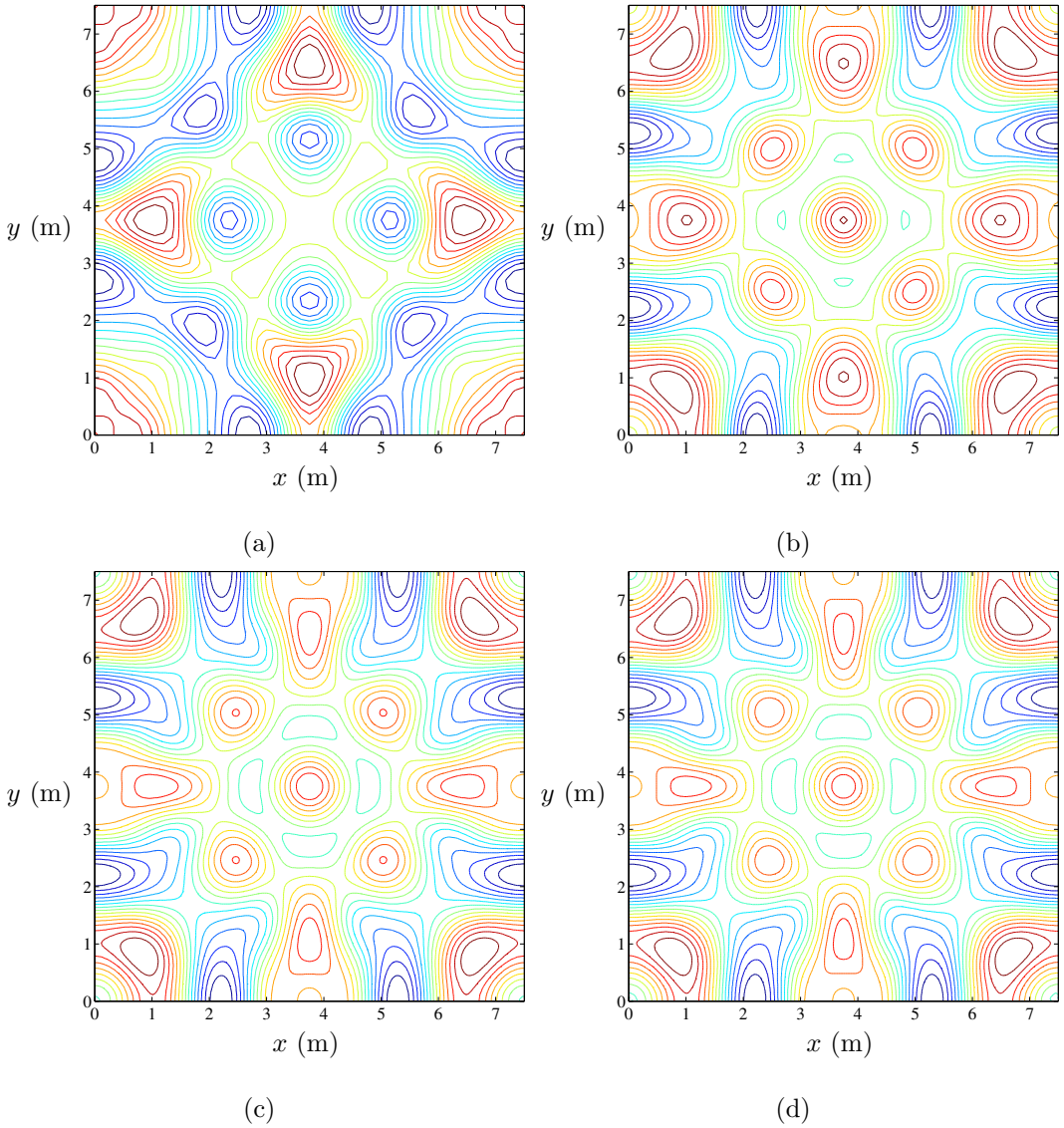

Figure 4.7: Evolution of initial Gaussian hump in a closed basin: numerically predicted free-surface elevation contours at $t = 10$ s for: (a) $\Delta x = \Delta y = 0.15$m; (b) $\Delta x = \Delta y = 0.075$m (c) $\Delta x = \Delta y = 0.0375$m; and (d) $\Delta x = \Delta y = 0.03$m.

is run backwards until $t = 0$ s. The total run time of 100 s provides a very sensitive check on the accuracy of the numerical model. As demonstrated in Figures 4.6, 4.7 and 4.3, the evolution of the Gaussian hump produces very complicated wave-wave and wave-wall interactions which are successfully reversed in this test. Figure 4.8 shows that the reversibility test recovers the initial Gaussian surface water profile, with negligible loss of amplitude. Figure 4.8b provides a closer look at the beginning and final stages of the reversibility check. The very small amplitude loss (≈ 0.2 mm) over the simulation duration is due to numerical dissipation in the Boussinesq solver, which can only approximate the evolution of the surface water profile by means of the numerical methods described in Chapter 3.

4.2 Harmonic analysis of sloshing waves

Spectral analysis is carried out on the symmetric sloshing problem described in Section 4.1 to investigate the harmonic structure of the evolving waveform. The methods described here provide a useful template for the investigation of the harmonic structure of focused wave groups in Chapter 6. A similar investigation was undertaken by Hunt (2003) into the structure of focused wave groups at the UKCRF.

4.2.1 Theoretical background

The combination of regular wave trains in deep water is used by Hunt (2003) to demonstrate the method for the isolation of harmonics and is summarised here. First-order linear wave theory produces sinusoidal waves. However real seas are nonlinear and do not have a sinusoidal profile; they are characterised by tall, narrow crests and flat troughs. Such seas can be described mathematically by a perturbation expansion, where each term provides a higher order correction to the linear theoretical model. Fenton (1990) gives the water surface elevation above still water level for a regular wave using a Stokes expansion up to fifth order:

$$\zeta(x,t) = \frac{1}{k}\sum_{i=1}^{5}\epsilon^i\sum_{j=1}^{i}B_{ij}\cos j(kx-\omega t), \tag{4.8}$$

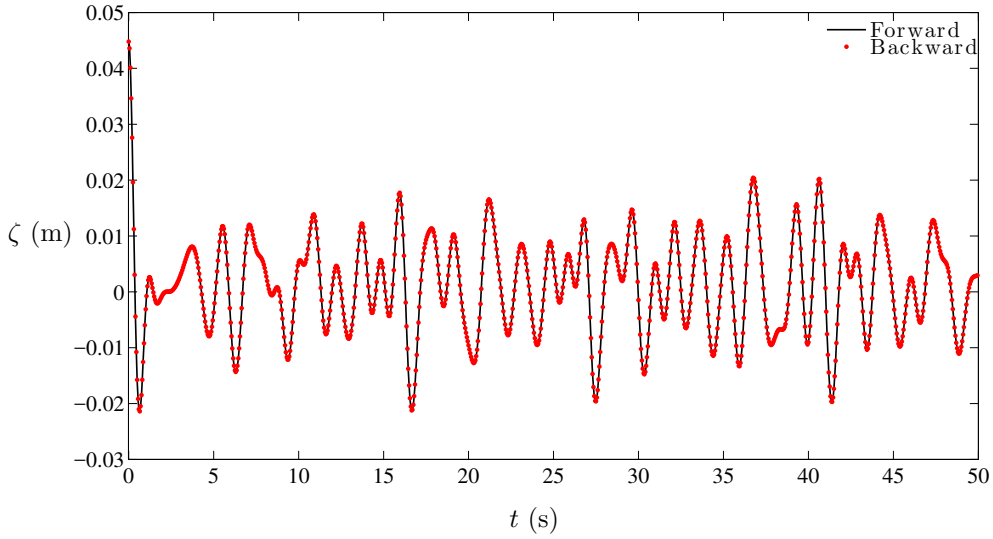

(a)

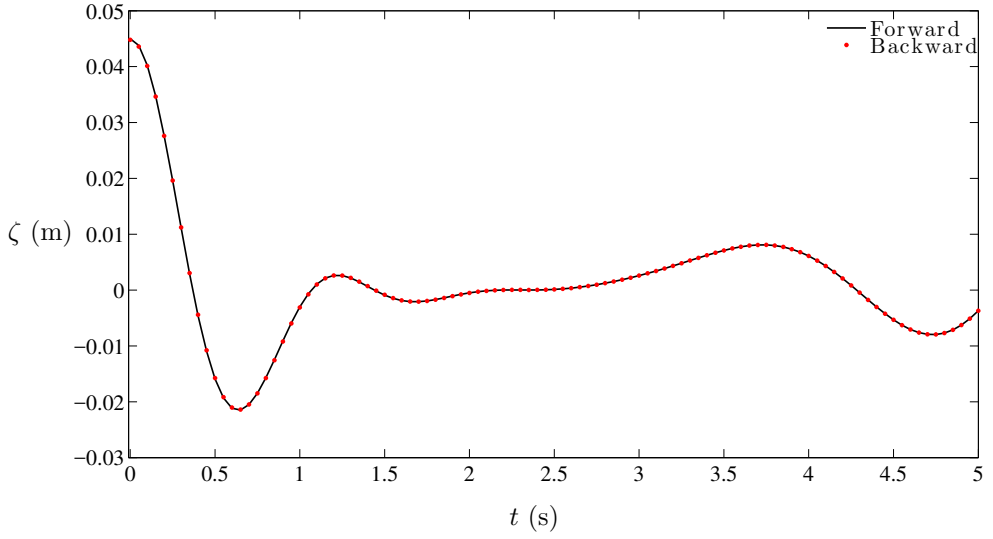

(b)

Figure 4.8: Evolution of initial Gaussian hump in a closed basin: reversibility check - numerical prediction of the surface elevation time series at the basin centre point for (a) 0 to 50 s and back to 0 s (b) 0 to 5 s and back to 0 s.

where x is the cross-shore distance in the direction of propagation, t is the time, k is the wave number, ω is the wave angular frequency, $\epsilon = ka$ where a is the wave amplitude and B_{ij} are coefficients given by Fenton (1990). For deep water, to third order, equation 4.8 becomes

$$\zeta(x,t) = a\cos(kx - \omega t) + \frac{1}{2}a^2 k \cos 2(kx - \omega t) + \frac{3}{8}a^3 k^2 \cos 3(kx - \omega t). \tag{4.9}$$

The first term of equation 4.9 is the linear sinusoidal wave, governed by the linear dispersion relation, $\omega^2 = kd\tanh(kd)$, where d is the water depth. The second term is the second-order correction to the linear wave and has a frequency double that of the linear term. The frequency (2ω) and wave number $(2k)$ pair for this term do not satisfy the linear dispersion relation. This second-order wave is referred to as a 'bound' wave and it travels at the same speed as the linear wave, which is called a 'free' wave.

Linear wave theory gives the surface elevation as

$$\zeta(x,t) = \sum_{n=1}^{N} a_n \cos(k_n x - \omega_n t), \tag{4.10}$$

where N is the number of waves. Thus a combination of two linear wave trains can be expressed as

$$\zeta(x,t) = a_1 \cos(k_1 x - \omega_1 t) + a_2 \cos(k_2 x - \omega_2 t). \tag{4.11}$$

Hunt (2003) cites Baldock (1995)[1] for a second-order Stokes expansion for deep water, given by

$$\zeta(x,t) = \sum_{n=1}^{N} \zeta_{(n)} + \sum_{n=1}^{N} \sum_{m=n+1}^{N} \zeta_{(n,m)}, \tag{4.12}$$

[1]Reference text not available.

which leads to the following expression for the simple case of two waves in deep water:

$$\begin{aligned}
\zeta(x,t) &= \sum_{n=1}^{2}\zeta_{(n)} + \sum_{n=1}^{2}\sum_{m=n+1}^{2}\zeta_{(n,m)} \\
&= \zeta_{(1)} + \zeta_{(2)} + \zeta_{(1,2)} \\
&= \underbrace{a_1\cos(k_1x-\omega_1t)}_{1} + \underbrace{\frac{1}{2}a_1^2k_1\cos 2(k_1x-\omega_1t)}_{2} \\
&\quad + \underbrace{a_2\cos(k_2x-\omega_2t)}_{3} + \underbrace{\frac{1}{2}a_2^2k_2\cos 2(k_2x-\omega_2t)}_{4} \\
&\quad + \underbrace{\frac{1}{2}a_1a_2(k_1+k_2)\cos((k_1+k_2)x-(\omega_1+\omega_2)t)}_{5} \\
&\quad - \underbrace{\frac{1}{2}a_1a_2(k_1-k_2)\cos((k_1-k_2)x-(\omega_1-\omega_2)t)}_{6}.
\end{aligned} \tag{4.13}$$

Terms 1 and 3 in equation (4.13) are the free linear waves which satisfy the linear dispersion relation; terms 2 and 4 are second-order waves with a frequency double that of the corresponding linear terms; term 5 is an additional second-order high frequency harmonic; while term 6 is an additional second-order low frequency harmonic. Terms 2, 4, 5, and 6 are all bound waves and do not satisfy the dispersion relation.

It is possible to isolate the harmonics of the above nonlinear wave group, through judicious addition and subtraction of the original wave group and its inverted form. Thus if equation (4.13) represents the crest focus wave group, ζ_c, the inverted, trough focus wave group ζ_t is given by

$$\begin{aligned}
\zeta_t(x,t) &= -a_1\cos(k_1x-\omega_1t) + \frac{1}{2}a_1^2k_1\cos 2(k_1x-\omega_1t) \\
&\quad - a_2\cos(k_2x-\omega_2t) + \frac{1}{2}a_2^2k_2\cos 2(k_2x-\omega_2t) \\
&\quad + \frac{1}{2}a_1a_2(k_1+k_2)\cos((k_1+k_2)x-(\omega_1+\omega_2)t) \\
&\quad - \frac{1}{2}a_1a_2(k_1-k_2)\cos((k_1-k_2)x-(\omega_1-\omega_2)t).
\end{aligned} \tag{4.14}$$

Adding and subtracting these wave groups provides useful insight into the harmonic

structure. The addition and subtraction series are given by

$$\begin{aligned}\frac{1}{2}(\zeta_c+\zeta_t) =& \frac{1}{2}a_1^2 k_1 \cos 2(k_1 x-\omega_1 t)+\frac{1}{2}a_2^2 k_2 \cos 2(k_2 x-\omega_2 t)\\ &+\frac{1}{2}a_1 a_2(k_1+k_2)\cos((k_1+k_2)x-(\omega_1+\omega_2)t)\\ &-\frac{1}{2}a_1 a_2(k_1-k_2)\cos((k_1-k_2)x-(\omega_1-\omega_2)t),\end{aligned} \tag{4.15}$$

and

$$\frac{1}{2}(\zeta_c-\zeta_t)=a_1\cos(k_1 x-\omega_1 t)+a_2\cos(k_2 x-\omega_2 t). \tag{4.16}$$

It can be seen from equations (4.15) and (4.16) that the addition series contains only second order harmonics, whilst the subtraction series contains only the linear contributions to the wave groups. Thus for higher-order wave groups, the addition series will contain all even harmonics, while the subtraction series contains the odd harmonics.

4.2.2 Application of harmonic analysis to sloshing in a closed basin

Following the method outlined in Section 4.2.1, the problem of sloshing in a closed basin is revisited, and harmonic analysis carried out by considering the propagation of the initial Gaussian hump of water described in Section 4.1, in conjunction with a Gaussian trough, of equal but opposite shape to the hump.

Figure 4.9a shows the subtraction time series at the basin centre-point, non- dimensionalised with respect to the initial hump amplitude. According to the theory outlined above, the subtraction series should contain the odd harmonics only, that is the main linear components and odd, higher order corrections. Figure 4.9b shows the addition time series at the centre-point of the basin, non-dimensionalised with respect to the initial hump amplitude. The addition series contains the even harmonics only, i.e. the second and higher even-order corrections to the main linear components. As can be seen in the Figure, the amplitudes of the even harmonics are small at first, but gradually increase as the simulation progresses, reaching approximately 20% of the initial amplitude H_0, demonstrating the increasing nonlinearity of the evolving waveform.

In addition to the case outlined above, where the ratio of the initial hump amplitude to the still water depth h is 10%, a second case is considered with a H_0 to h ratio of 1%, i.e. $H_0 = 0.0045$ m. Figure 4.10a shows the non-dimensionalised subtraction time-series

at the basin centre-point, which appears identical to the 10% case. However, Figure 4.10b, which shows the corresponding addition time series, reveals that the second and higher even-order contributions for a H_0 to h ratio of 1% are significantly reduced, demonstrating decreasing nonlinearity with decreasing initial amplitude.

The same exercise is carried out for a rectangular basin, where $L_x = 15$ m and $L_y = 7.5$ m, and the ratio of H_0 to h is 10% in a still water depth of $h = 0.45$ m. Figure 4.11 shows the non-dimensionalised subtraction and addition time series at the basin centre-point respectively. By comparing Figure 4.9 with Figure 4.11, it can be seen that the amplitude of the sloshing motions at tank centre are smaller for the rectangular basin, and the nonlinear contributions are significantly diminished.

The component frequencies of the sloshing problem can be analysed by applying a fast-Fourier transform (FFT) to the addition and subtraction time series. Peaks in the resulting amplitude spectra may indicate free-surface resonances occurring in the basin. The fundamental frequencies for the analytical solution of the square basin for each of the (n, m) wave modes, are obtained from

$$f_{n,m} = \frac{1}{T_{n,m}} = \frac{\omega_{nm}}{2\pi}, \tag{4.17}$$

where

$$\omega_{nm} = \sqrt{gh}k_{nm} = \sqrt{gh_0\left(\frac{\pi}{L}\right)^2(n^2+m^2)}, \tag{4.18}$$

in which $L = 7.5$ m is the length of the basin, h is the still water depth and ω_{nm} and k_{nm} are the angular frequency and wave number respectively for the $n-m^{\text{th}}$ mode. Table 4.2 shows the analytical fundamental frequencies calculated using equations (4.17) and (4.18) above. Note that these frequencies apply to the linear analytical solution only, and do not include any nonlinear effects.

Figure 4.12 shows the amplitude spectra for the test case of $H_0/h = 10\%$, obtained by taking the absolute value of the FFT of the subtraction and addition time series at the basin centre-point. Figure 4.12a exhibits a concentration of energy at 0.57 Hz, which may be linked to the fundamental frequencies at $m = 0$, $n = 4$, and at $m = 4$, $n = 1$. Other significant peaks occur at 0.27 Hz , 0.38 Hz, 0.74 Hz and 0.81 Hz, which again may be linked to other linear wave modes given in table 4.2, and modified

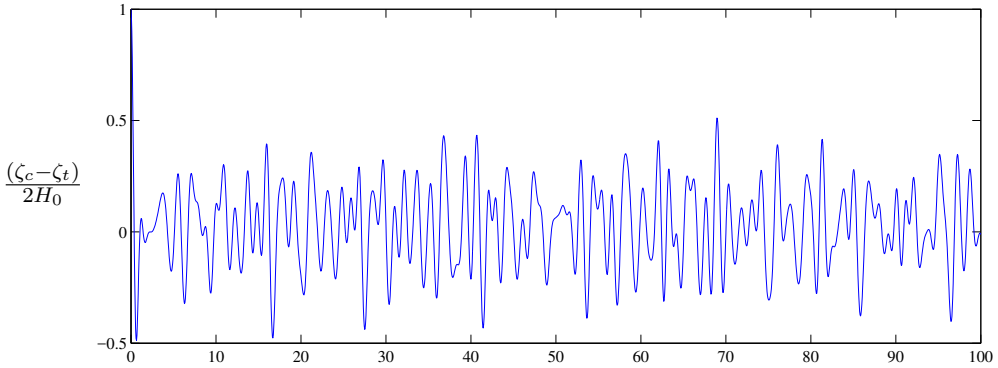

(a)

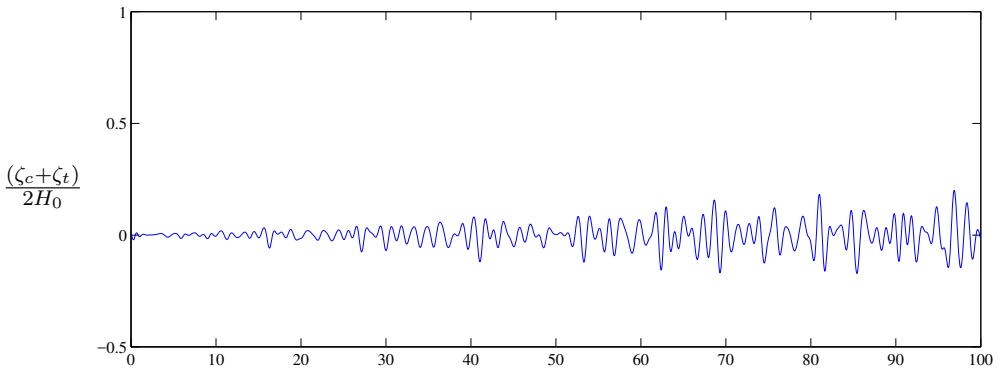

(b)

Figure 4.9: Sloshing in a closed square basin: (a) odd harmonics obtained as the non-dimensionalised subtraction time series at the basin centre-point; and (b) even harmonics obtained as the non-dimensionalised addition time series at the basin centre-point, for H_0/h =10%.

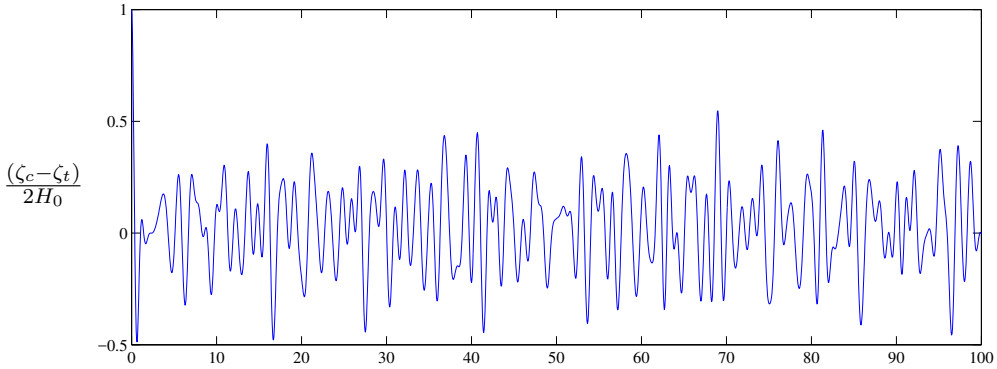

(a)

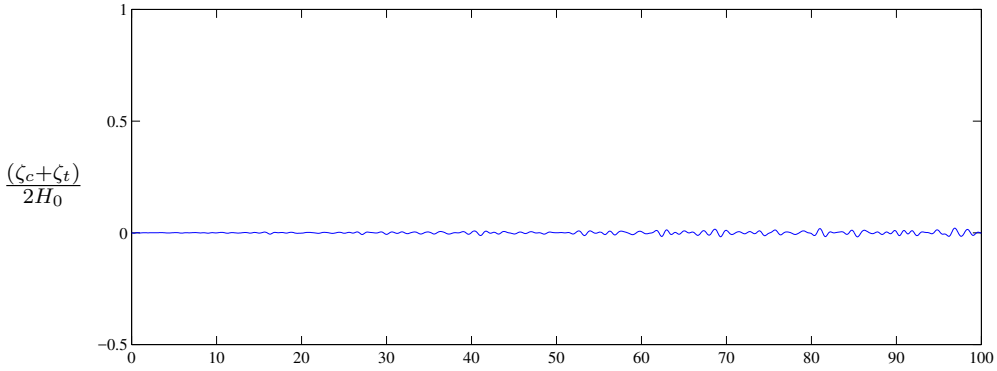

(b)

Figure 4.10: Sloshing in a closed square basin: (a) odd harmonics obtained as the non-dimensionalised subtraction time series at the basin centre-point; and (b) even harmonics obtained as the non-dimensionalised addition time series at the basin centre-point, for H_0/h =1%.

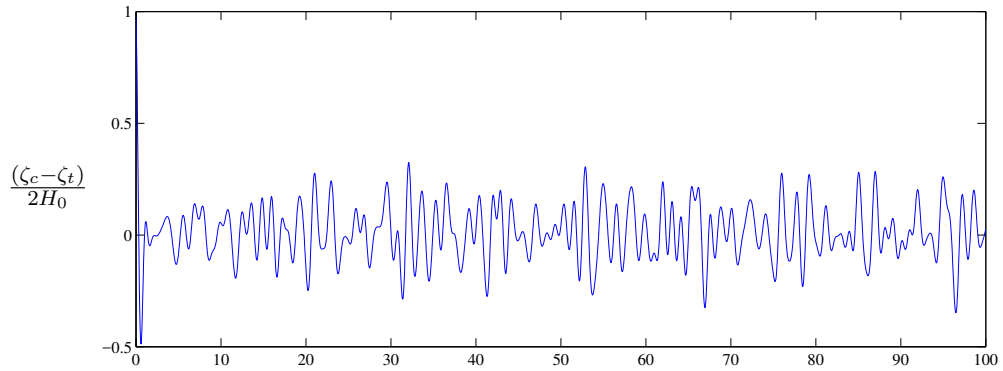

(a)

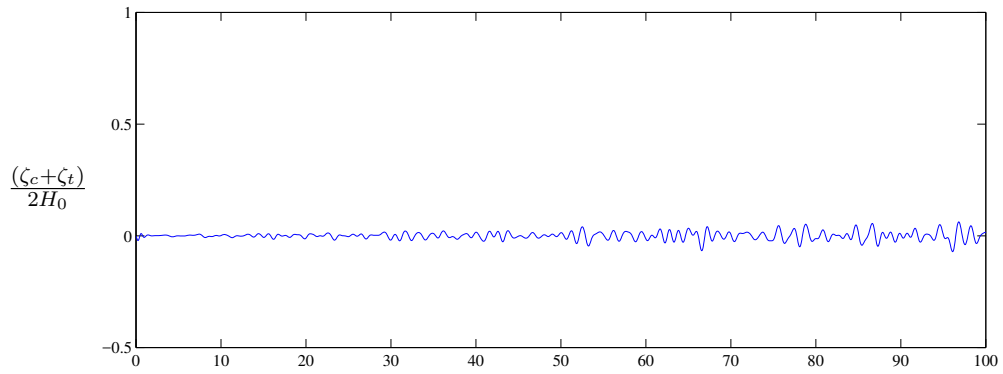

(b)

Figure 4.11: Sloshing in a closed rectangular basin: (a) odd harmonics obtained as the non-dimensionalised subtraction time series at the basin centre-point; and (b) even harmonics obtained as the non-dimensionalised addition time series at the basin centre-point, for H_0/h =10% and basin dimensions 15 m by 7.5 m.

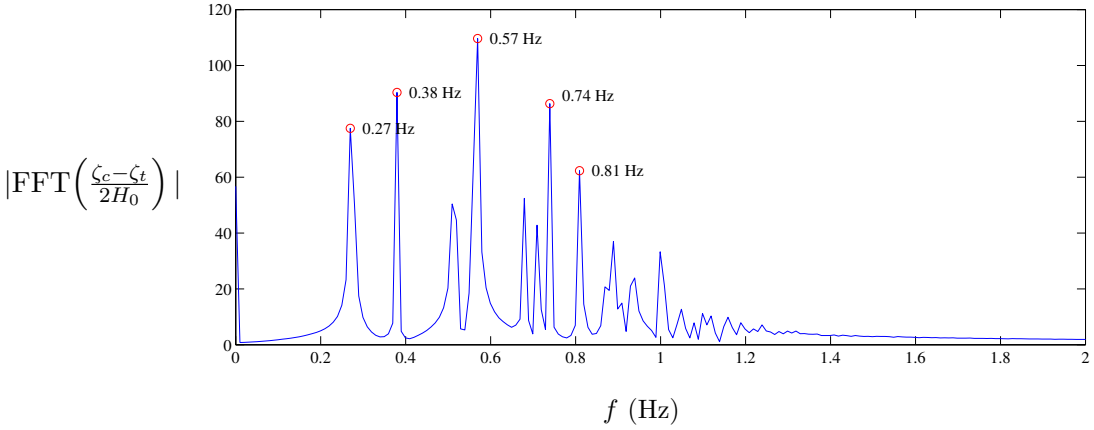

(a)

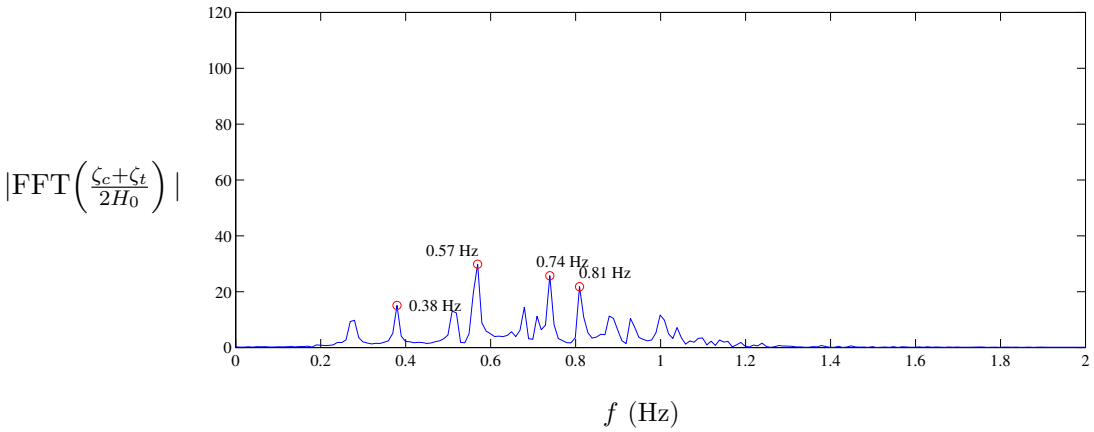

(b)

Figure 4.12: Sloshing in a closed square basin: (a) odd harmonics - amplitude spectrum of non-dimensionalised subtraction time series at the basin centre-point; and (b) even harmonics - amplitude spectrum of non-dimensionalised addition time series at the basin centre-point, for H_0/h =10%

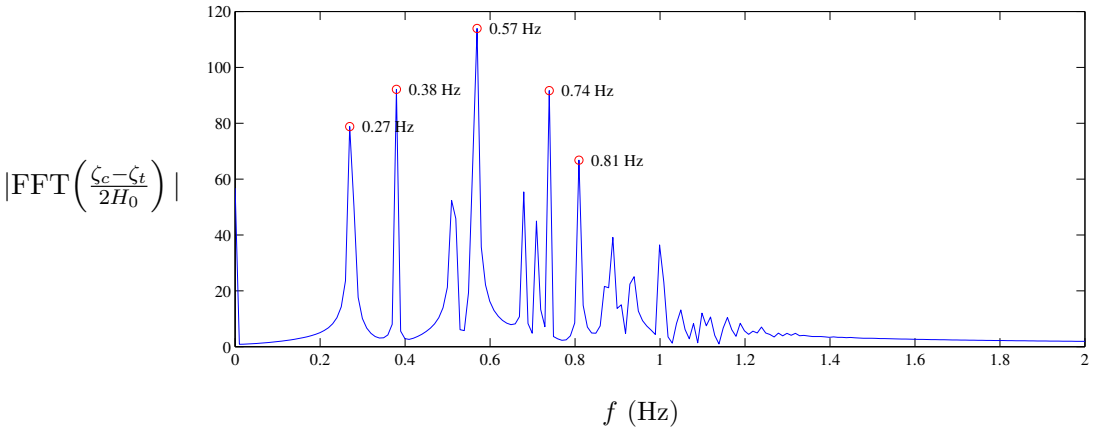

(a)

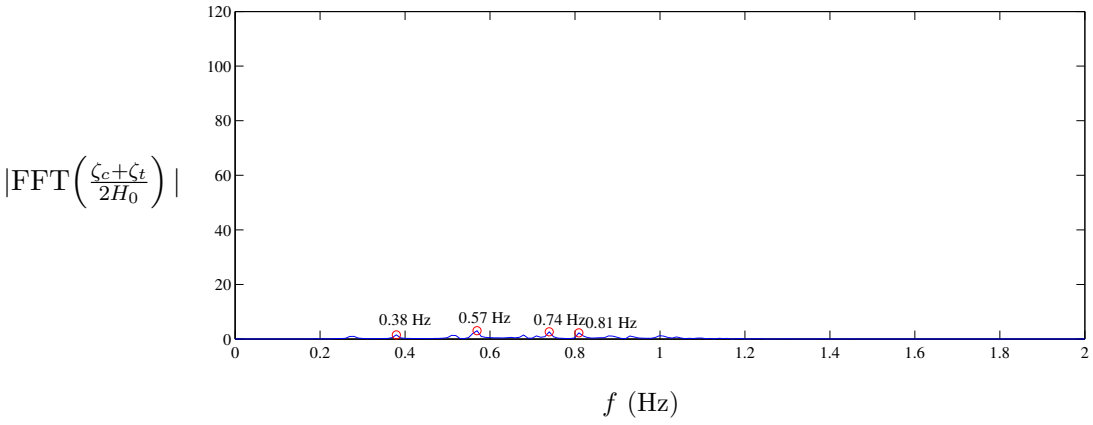

(b)

Figure 4.13: Sloshing in a closed square basin: (a) odd harmonics - amplitude spectrum of non-dimensionalised subtraction time series at the basin centre-point; and (b) even harmonics - amplitude spectrum of non-dimensionalised addition time series at the basin centre-point, for H_0/h =1%

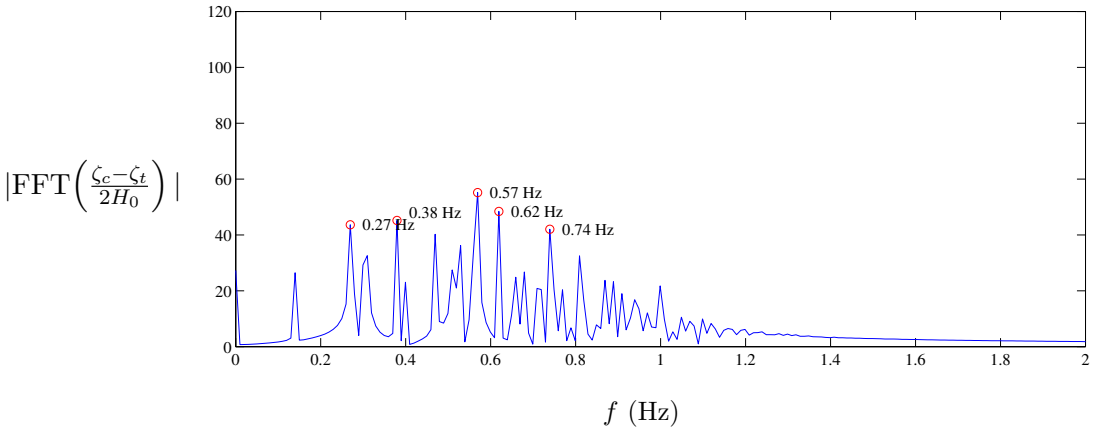

(a)

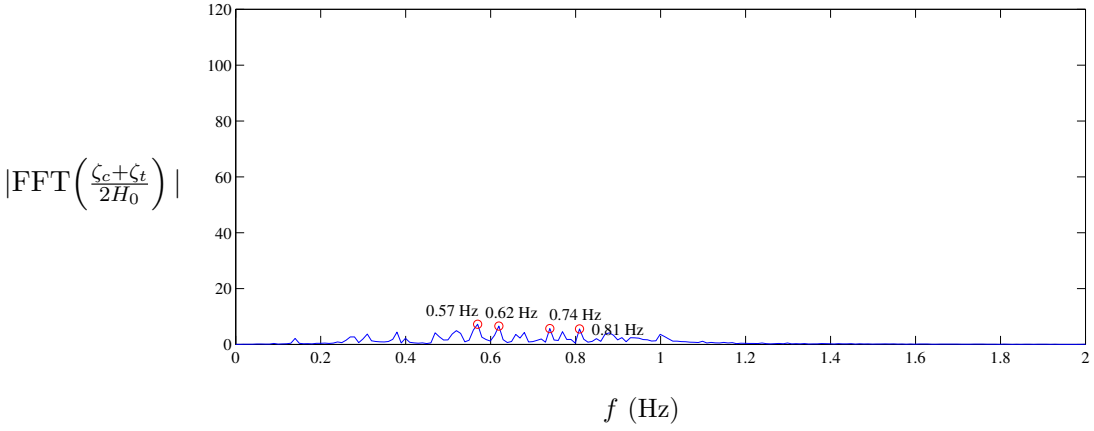

(b)

Figure 4.14: Sloshing in a closed rectangular basin: (a) odd harmonics - amplitude spectrum of non-dimensionalised subtraction time series at the basin centre-point; and (b) even harmonics - amplitude spectrum of non-dimensionalised addition time series at the basin centre-point, for H_0/h =10%, and basin dimensions $L_x = 15$ m and $L_y = 7.5$ m

m \ n	1	2	3	4	5	6	...
0	0.14	0.28	0.42	0.56	0.7	0.84	...
1	0.198	0.313	0.443	0.578	0.714	0.852	
2	0.313	0.396	0.505	0.626	0.754	0.886	
3	0.443	0.505	0.594	0.7	0.817	0.94	
4	0.578	0.626	0.7	0.792	0.897	1.01	
5	0.714	0.754	0.817	0.897	0.99	1.094	
6	0.852	0.886	0.94	1.01	1.094	1.189	
⋮	⋮						⋱

Table 4.2: Analytical fundamental frequencies for sloshing in a square basin (values in Hz)

by the presence of higher order odd harmonics. Figure 4.12b shows the component frequencies of the addition time series, i.e. the even order harmonics. Again, the same frequency wave components as for the subtraction time series are notable, but at a reduced amplitude, indicating the sloshing motion is largely governed by the linear terms. Figure 4.13 shows the amplitude spectra for the test case of $H_0/h = 1\%$. A comparison with Figure 4.12 reveals that the nonlinear components for the smaller initial amplitude have a much smaller relative contribution, than for the $H_0/h = 10\%$ case. This confirms that the test case of sloshing of an initial Gaussian hump in a closed basin becomes increasingly nonlinear, with increasing initial hump amplitude.

Figure 4.14 shows the results of the spectral analysis applied to the case sloshing in a rectangular basin, with $H_0/h = 10\%$. Comparing the results with Figure 4.12, it is immediately obvious that the energy is spread more evenly across a greater number of frequencies. Also apparent is the relatively small contribution of the even harmonics.

4.3 Wetting and drying algorithm check

4.3.1 Sloshing in a parabolic basin

Sampson et al. (2006) build on the work of Thacker (1981) to derive an analytical solution of the nonlinear shallow water equations for sloshing in a parabolic basin. The bed profile of the parabolic basin is given by

$$z_b(x) = \frac{h_0}{a^2}(x - 0.5L_x)^2, \tag{4.19}$$

where z_b is uniform with zero slope in the y-direction, L_x is the length of the domain in the x-direction, h_0 is the still water depth at $x = 0.5L$, and a is the width of the basin at elevation $z = h0$. Sampson et al. give the initial sloping free surface as

$$\eta(x,0) = h_0 + \frac{a^2B^2}{8g^2h_0}\left(\frac{\tau^2}{4} - s^2\right) - \frac{B^2}{4g} - \frac{Bs}{g}(x - 0.5L). \tag{4.20}$$

The analytical solution of the water surface time history is

$$\begin{aligned}\eta(x,t) = h_0 + \frac{a^2B^2\mathrm{e}^{-\tau t}}{8g^2h_0}\left(-s\tau\sin(2st) + \left(\frac{\tau^2}{4} - s^2\right)\cos(2st)\right) \\ - \frac{B^2\mathrm{e}^{-\tau t}}{4g} - \frac{\mathrm{e}^{-\tau t/2}}{g}\left(Bs\cos(st) + \frac{\tau B}{2}\sin(st)\right)(x - 0.5L),\end{aligned} \tag{4.21}$$

where B is a velocity constant and s is a constant given by $s = 0.5\sqrt{8gh_0/a^2 - \tau^2}$. τ is a fixed friction parameter related to the bed friction coefficient by $C_f = h\tau/\sqrt{u^2 + v^2}$. Note that B is unrelated to the Boussinesq dispersion coefficient, but is used here to match the notation used by Sampson et al.

For the numerical simulation, the computational domain has plan dimensions of $L_x = 220$ m and $L_y = 17.6$ m, with $\Delta x = \Delta y = 1.76$ m. The values of the coefficients are $a = 80$ m, $B = 10$ ms^{-1}, $h_0 = 80$ m and $\tau = 0.1$ s^{-1}. The time step $\Delta t = 0.04$ s and the simulation is run for 80 s.

Excellent agreement is obtained between the analytical and numerical solutions, as shown in Figure 4.15. The model accurately predicts the moving wet/dry front, thereby validating the wetting and drying algorithm. The simulation is also run with the basin and initial water surface profile rotated by 90°, i.e. with the bed profile uniform, with zero slope in the x direction, and the parabolic profile occurring in the $y - z$ plane.

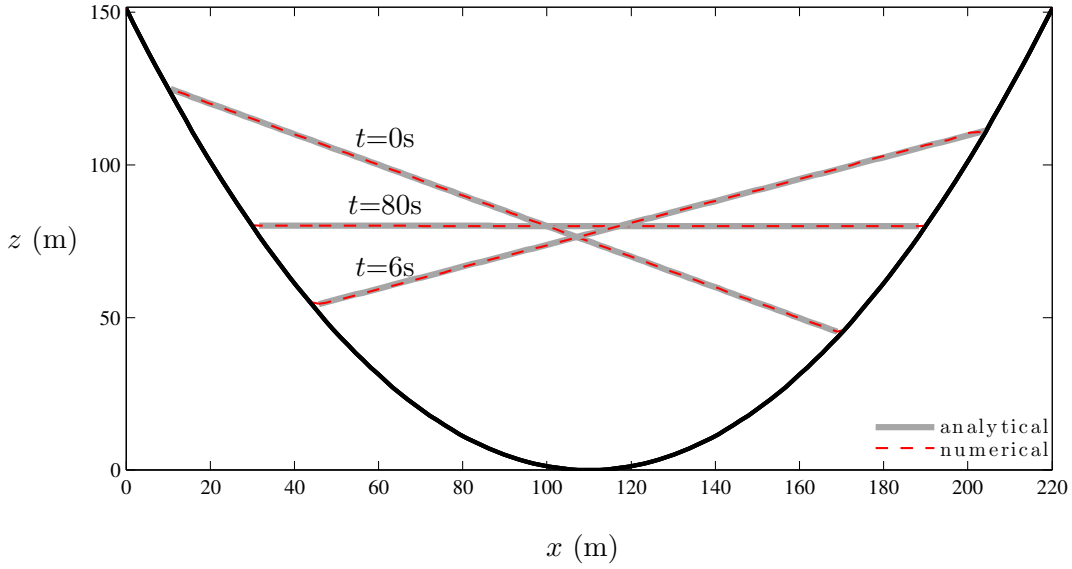

Figure 4.15: Sloshing in a parabolic basin: analytical (Sampson et al. (2006)) and numerical free-surface profiles at times $t = 0$, 6, and 80 s.

The results produced for this orientation are identical to those above, allowing for the changed coordinate axis. This benchmark verification test has also been used by other researchers (see e.g. Orszaghova et al. (2012) and Liang and Borthwick (2009)).

Numerical convergence of the shallow water solver is assessed in a similar manner to Section 4.1.1. Four different grids are again considered, where $\Delta x = \Delta y = 8.8$ m is the coarsest, and $\Delta x = \Delta y = 1.1$ m is the finest. Again, both the grid size and time step are reduced by a factor of 2 for each grid refinement. The L^2-norm is calculated for a singe row of grid points in the direction of sloshing at $t = 72$ s according to Equation (4.5), and the convergence rate is assessed using Equation (4.7). Table 4.3 presents the calculated errors and the associated convergence rate for each grid considered. The table shows that for each grid refinement, the error reduces.

4.3.2 Dam-break wave

A comprehensive test of the wetting and drying capabilities of the finite volume solver is provided using the case of a dam-break wave travelling over a flood plain with three humps. This test case was originally proposed by Kawahara and Umetsu (1986), and

$\Delta x = \Delta y$	Δt	$\|\|\mathbf{E}\|\|_2$	c_r
8.8	2.4	85.9817	-
4.4	1.2	1.3995	5.9411
2.2	0.6	0.7800	0.8434
1.1	0.3	0	-

Table 4.3: Error and convergence rate calculation of the numerical model at $t = 72$ s using the parabolic basin test

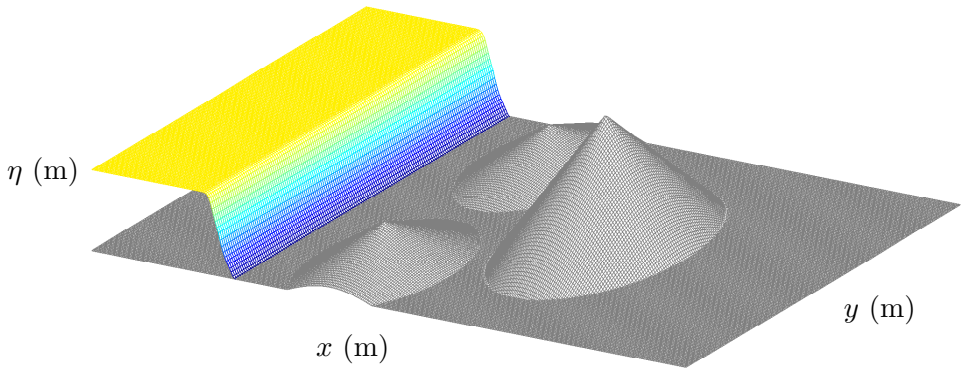

Figure 4.16: Wetting and drying test: flood plain topography and initial water free surface, with dam at $x = 16$m at $t = 0$s.

has also been considered by other researchers, including Brufau et al. (2002) and Liang and Borthwick (2009). The basin under consideration is 75 m long and 30 m wide, with vertical, reflective walls. The flood plain is initially dry and the bed topography is defined by

$$z_b(x,y) = \max\Bigg[0, 1 - \frac{1}{8}\sqrt{(x-30)^2 + (y-6)^2}, \\ 1 - \frac{1}{8}\sqrt{(x-30)^2 + (y-24)^2}, \\ 3 - \frac{3}{10}\sqrt{(x-47.5)^2 + (y-15)^2}\Bigg]. \tag{4.22}$$

Upstream of the dam at $x = 16$ m, the initial still water level is $\eta = 1.875$ m as shown in Figure 4.16. The simulation is run with a computational grid defined by $\Delta x = \Delta y = 0.2$ m and time step $\Delta t = 0.01$ s. The bed roughness is calculated using a value of the Manning coefficient of $n = 0.018$ s m$^{-1/3}$. At $t = 0$ s, the dam collapses and water begins to inundate the flood plain. Figure 4.17 shows various stages of propagation of the flood wave. By $t = 2.4$s, the wave has crested the two small hills, and by $t = 4$s has begun to encroach on the large hill. The momentum of the flood causes the wet/dry front to rush more than two thirds of the way up the large hill as well as spilling around its sides. Reflections from the small hills travel upstream and merge to form an almost straight bore. As the water makes its way down the flood plain, waves also climb the vertical side walls of the basin. At $t \approx 13$ s, the flood wave hits the eastern boundary of the basin, and the reflected wave travels back upstream. Steady state is eventually reached at $t \approx 300$ s. The model successfully simulates complicated wave-wave and wave-wall interactions, as well as the complicated wetting and drying processes resulting from the wave-topography interactions. While no numerical comparisons were carried out, the visualisations presented in Figure 4.17 closely match those produced by Brufau et al. (2002) and Liang and Borthwick (2009).

4.4 Paddle wave generation test

To test whether the numerical model can generate waves of the desired amplitude, a solitary wave is considered. Orszaghova (2011) derives a semi-analytical solution for a solitary wave for the one-dimensional Boussinesq equations of Madsen and Sørensen

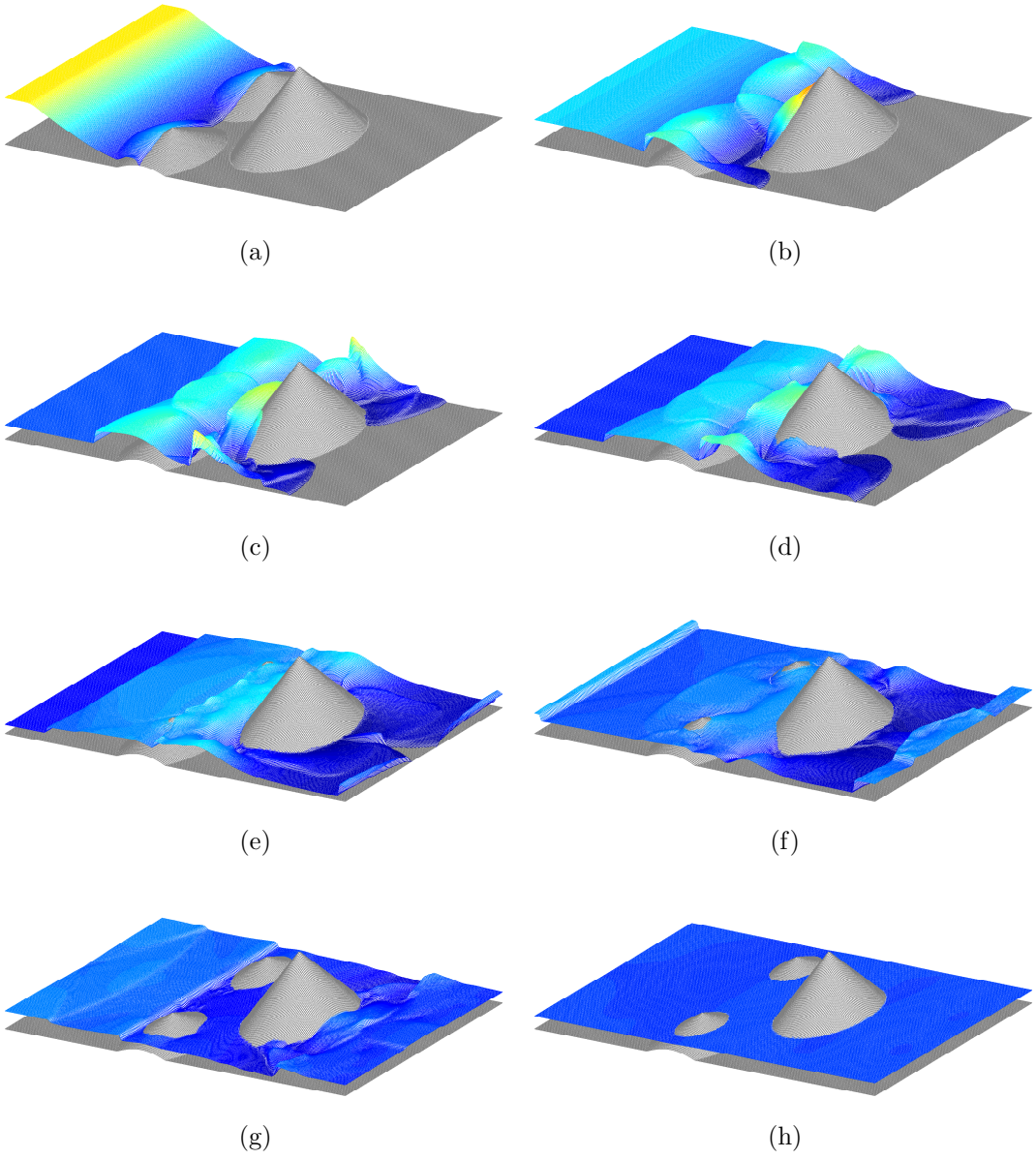

Figure 4.17: Propagation of a dam break wave over a floodplain with three humps: 3D visualisation at (a) $t = 2.4$ s; (b) $t = 6$ s; (c) $t = 9.8$ s; (d) $t = 12$ s; (e) $t = 15$ s; (f) $t = 19.8$ s; (g) $t = 30$ s; (h) $t = 300$ s.

(1992), with a closed form relation between the amplitude of the solitary wave and its celerity. The one-dimensional Madsen and Sørensen equations, for flat bottom topography and no bed friction, can be written as

$$\zeta_t + q_x = 0 \tag{4.23a}$$

and

$$q_t + \left(\frac{q^2}{h+\zeta}\right)_x + g(h+\zeta)\zeta_x = \left(B + \frac{1}{3}\right) h^2 q_{xxt} + Bgh^3\zeta_{xxx}, \tag{4.23b}$$

where q is the one-dimensional flux, and the subscripts denote derivates. A solitary wave satisfies

$$\zeta(x,t) = \zeta(x - Ct) \equiv \zeta(\xi), \qquad \lim_{\xi\to\pm\infty} \zeta^{(n)}(\xi) = 0, \tag{4.24a}$$

and

$$q(x,t) = q(x - Ct) \equiv q(\xi), \qquad \lim_{\xi\to\pm\infty} q^{(n)}(\xi) = 0, \tag{4.24b}$$

where C is the wave celerity, $\xi = x - Ct$ is the moving ordinate and the superscript $^{(n)}$ is the n^{th} derivative with respect to ξ, for $n = 0, 1, 2 \ldots$.

A direct integration method is implemented, which reduces equations (4.23) to

$$-C\zeta + q = 0 \tag{4.25a}$$

and

$$-Cq + \frac{q^2}{h+\zeta} + gh\zeta + \frac{1}{2}g\zeta^2 = -C\left(B + \frac{1}{3}\right) h^2 q'' + Bgh^3\zeta'' \tag{4.25b}$$

where the primes represent the derivative with respect to ξ. Substituting equation (4.25a) into (4.25b) gives the second-order ordinary differential equation

$$q''\left(-C\left(B + \frac{1}{3}\right) h^2 + \frac{Bgh^3}{C}\right) = \left(\frac{gh - C^2}{C}\right) q + \left(\frac{g}{2C^2}\right) q^2 + \frac{Cq^2}{Ch + q}. \tag{4.26}$$

A first-order ordinary differential equation for the flux q is then obtained by Orszaghova by pre-multiplying (4.26) by q' and integrating with respect to ξ:

$$\frac{1}{2}(q')^2\left(-C\left(B + \frac{1}{3}\right) + \frac{Bgh}{C}\right) = \left(-\frac{C^2}{h}\right) q + \left(\frac{g}{2Ch}\right) q^2 + \frac{g}{6C^2h^2} q^3 + C^3 \ln\left(\frac{Ch+q}{Ch}\right), \tag{4.27}$$

which can be rearranged to give

$$q' = \pm\sqrt{\frac{3Cghq^2 + gq^3 - 6C^4hq + 6C^5h^2(\ln(Ch+q) - \ln(Ch))}{Ch^2(-3C^2B - C^2 + 3Bgh)}} \equiv \pm Z(q). \quad (4.28)$$

Setting $q' = 0$ gives the relationship between C and q at the peak flux q_{max}. The relationship between this celerity and the amplitude of the solitary wave A is given by Orszaghova as

$$C = \sqrt{\frac{ghA^2(A+3h)}{6h^2(A - h\ln(\frac{h+A}{h}))}}. \quad (4.29)$$

The paddle displacement series x_p for a solitary wave of amplitude A in still water depth h is generated by solving

$$(x_p)_t = \bar{u}(x_p, t), \quad (4.30)$$

where the depth-averaged velocity is given by

$$\bar{u} = \frac{q}{\zeta + h}, \quad (4.31)$$

and is calculated using the theory outlined above. For a specified A and h, equations (4.25a) and (4.29) give the peak flux q_{max} and the corresponding wave celerity C. To calculate the flux profile of the solitary wave, (4.28) is solved numerically with Matlab's in-built ordinary differential equation solver, *ode113*. The corresponding free-surface profile is determined from (4.25a) and the velocity profile of the solitary wave is calculated from (4.31). The paddle displacement signal is then calculated by applying the ode113 solver to (4.30).

To verify the wave generation by the numerical piston paddles in the model, a paddle displacement signal is calculated by the method outlined above for a solitary wave of amplitude $A = 0.6$ m in still water depth $h = 1.0$ m. The calculated signal, shown in Figure 4.18 is then applied to each paddle in the numerical basin. The basin is 50 m by 5 m in the x- and y-directions respectively, with $imax = 26$ paddles moving as one along the western boundary. The grid spacing is $\Delta x = 0.1$ m and $\Delta y = 0.2$ m, and the time step is set to $\Delta t = 0.006$ s. The bed friction and eddy viscosity parameters are set to zero. Figure 4.19 presents a 3D visualisation of the solitary wave at $t = 10$ s. Figure 4.20 shows a side-on view of the wave as it moves away from the paddle, along

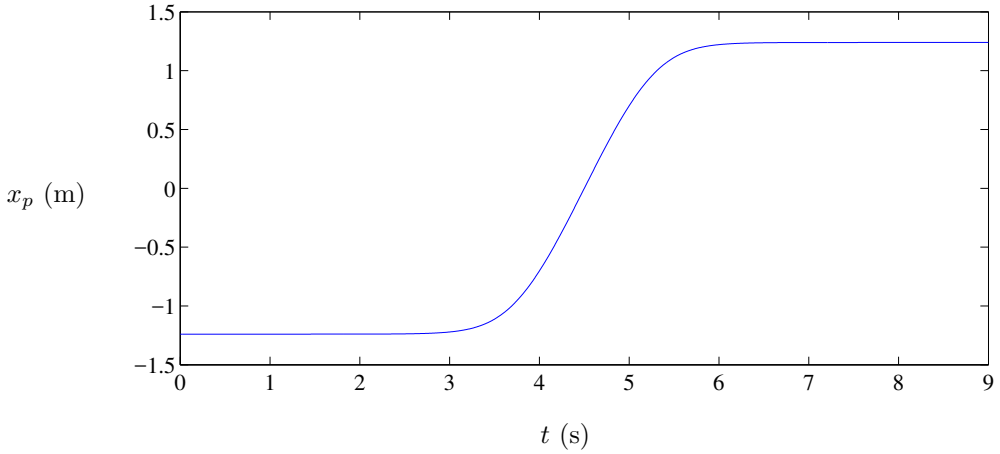

Figure 4.18: Paddle signal for the generation of a 0.6 m amplitude solitary wave

the basin in the $x-$direction at $t = 0$, 4.5, 10 and 15 s. Here the free-surface profiles are stacked with a vertical spacing of 0.6 m to demonstrate that a wave of correct amplitude is generated, and that this amplitude is maintained as the wave propagates. The paddles in both figures are shown in red. This verification test also confirms that the wave is unaffected as it passes from the moving paddle domain into fixed Boussinesq domain. This demonstrates that the non-uniform finite difference stencils at the interface between the moving and fixed domains are implemented correctly.

4.5 Chapter summary

- In this chapter, various key aspects of the numerical model have been verified using benchmark tests. The evolution of sloshing waves in a closed, square basin is used to check the correct handling of the cross-derivative terms in the Boussinesq equations, where the initial wave form is a Gaussian hump of water. The numerical results are compared with an analytical solution and excellent agreement is obtained. A reversibility test, involving the propagation of the Gaussian hump forward and then backward in time confirms the accuracy of the numerical methods applied in the model. A harmonic analysis is carried out to investigate the harmonic structure of the sloshing waves.

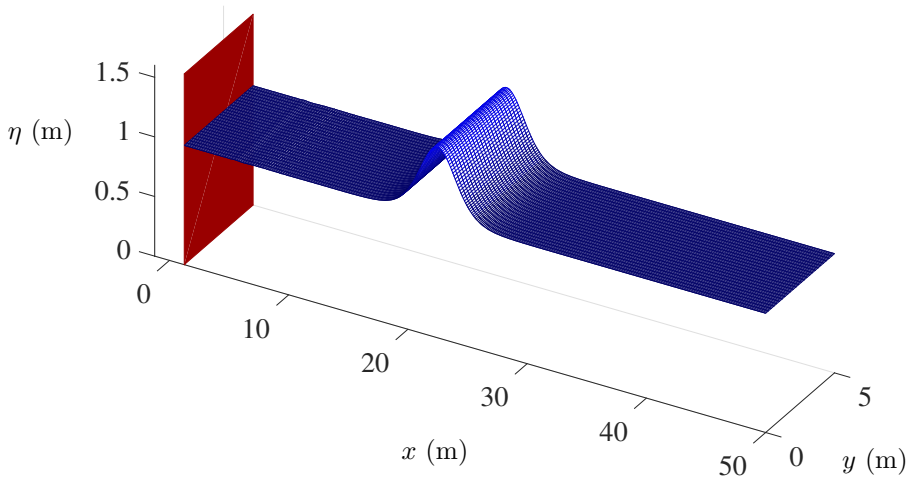

Figure 4.19: Solitary wave generated by numerical piston paddles: 3D visualisation at $t = 10$ s

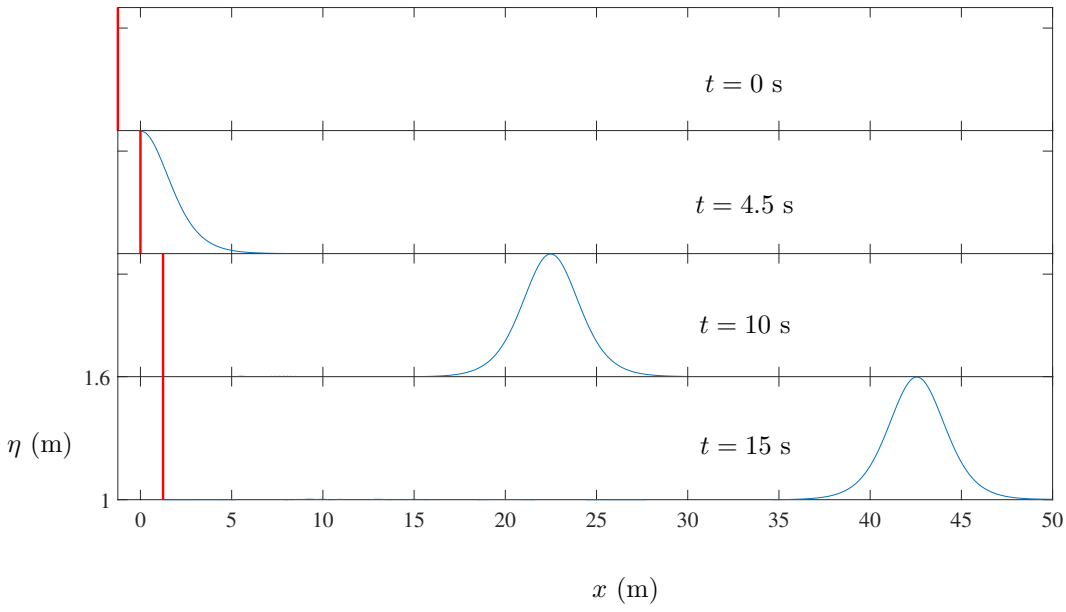

Figure 4.20: Solitary wave generated by numerical piston paddles: side-on view of stacked surface water profiles

- The finite volume solver and the wetting and drying algorithm are verified by considering first the problem of sloshing in a parabolic basin. The numerical results are in excellent agreement with the analytical solution, with the model accurately predicting the moving wet/dry front. The wetting and drying capabilities of the finite volume solver are tested further by considering the propagation of a dam-break wave. The model successfully simulates the complicated wave-wave and wave-wall interactions, and the wetting and drying processes with the results closely matching those of other researchers.

- Implementation of the moving paddle wavemaker is tested by calculating the paddle signal for a solitary wave and confirming that the generated wave matches the specified input amplitude.

- It is noted that the representation of bed friction in the model has not been comprehensively validated.

Chapter 5

Results I: Nearshore circulation

In practice, coastlines are irregular, coastal bathymetries are non-planar, and the interaction of the sea with the coast results in complex hydrodynamic processes. Numerous experiments have been carried out by researchers in the laboratory to model physically these interactions. In this chapter, results are presented from numerical simulations of laboratory experiments involving wave-induced currents and circulation cells arising from the interaction of regular waves with a half-sinusoidal beach and a tri-cuspate beach.

5.1 Nearshore circulation at a sinusoidal beach

In order to determine whether the model is capable of simulating near shore circulation, the laboratory experiment carried out by da Silva Lima (1981) is considered. In his experiment, da Silva Lima constructed a plywood sinusoidal beach in a wave basin and measured the wave heights and currents that resulted from paddle generated regular waves travelling normal to the beach. These data have been used by a number of other researchers to verify numerical models, such as Park and Borthwick (2001) and Rogers et al. (2004).

The still water depth for da Silva Lima's experiment is given by

$$h_s(x,y) = \begin{cases} \left[x - 0.75 \sin\left(\frac{\pi x}{4.36}\right) \sin\left(\frac{2\pi y}{\lambda}\right)\right] s & 0 \leq x \leq 4.36\,\text{m} \\ xs & -0.7\text{m} \leq x \leq 0\,\text{m} \\ h_0 & x > 4.36\,\text{m} \end{cases} \tag{5.1}$$

where x is the distance offshore from the still water line, y is the alongshore distance with a range of 1.5 to 4.5 m, h_0 is the still water depth offshore of the toe, $s = 0.05$ is the slope of the plane beach and $\lambda = 6$ m is a parameter known as the rip current spacing. Applying (5.1) to a 6 m long and 3 m wide numerical basin results in the bathymetry shown in Figure 5.1.

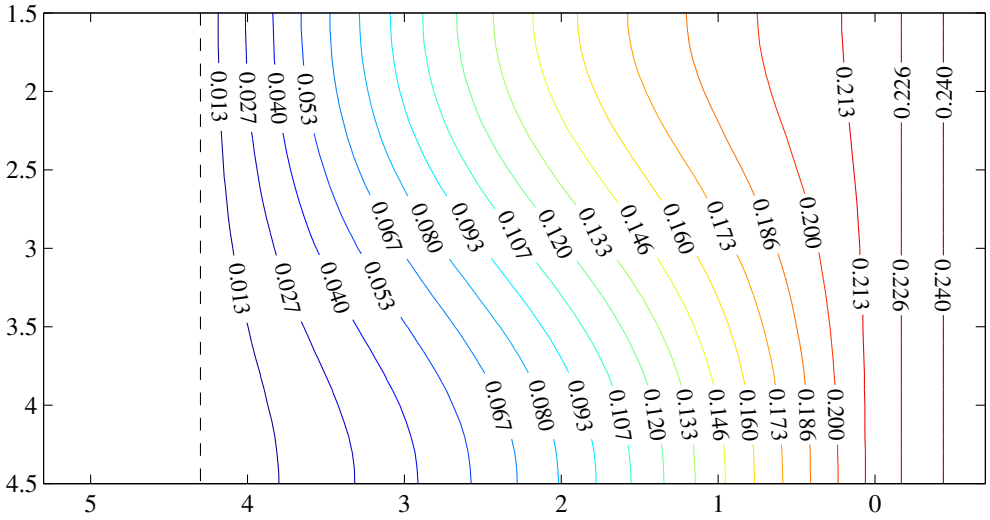

Figure 5.1: Sinusoidal beach bathymetry

5.1.1 Eddy viscosity and bed friction

In addition to the constant eddy viscosity model described in Section 2.3, the non-uniform eddy viscosity model of Thornton (1970) [1], described by Park and Borthwick (2001) and Rogers et al. (2004) is also implemented for comparison. Here, the eddy viscosity is given by

$$\varepsilon = M_T A_b \tilde{u}_{\max} \tag{5.2}$$

[1] Referenced by Rogers et al. (2004) but full text not available

where M_T is a dimensionless mixing parameter, and A_b is the excursion length of the orbital motion at the bed, given by

$$A_b = \frac{a}{\sinh(kh)} = \frac{\tilde{u}_{\max} T}{2\pi}, \tag{5.3}$$

in which a is the wave amplitude and T is the period. The maximum wave particle velocity at the bed is

$$\tilde{u}_{\max} = \frac{2\pi a}{T \sinh(kh)}. \tag{5.4}$$

Here, the bed friction coefficient C_f is calculated following the method of Rogers et al. (2004) who references the formula of Jonsson (1966)[2] which is a function of both wave and current bed friction coefficients, $\tilde{C}_f$ and C_{fcur}:

$$C_f = \frac{\tilde{C}_f + \alpha C_{fcur}}{1 + \alpha}, \tag{5.5}$$

where α is a weighting coefficient given by

$$\alpha = \frac{\sqrt{u^2 + v^2}}{\tilde{u}_{\max}}. \tag{5.6}$$

$\tilde{C}_f$ and C_{fcur} are calculated using empirical expressions based on experimental data. The wave friction factor is determined using Jonsson's formula,

$$\tilde{C}_f = \exp\left(5.213 \left(\frac{A_b}{R_h}\right)^{-0.194} - 6.67\right), \tag{5.7}$$

where R_h is the roughness height. The current friction factor is calculated from the expression obtained by Bijker (1966)[3].

$$C_{fcur} = 0.016 \left(\frac{R_h}{h}\right)^{\frac{1}{3}} \tag{5.8}$$

5.1.2 Numerical simulation

For the numerical simulation, grid convergence is achieved using grid spacings $\Delta x = \Delta y = 0.05$ m and a time step of $\Delta t = 0.005$ s. Regular waves are generated using the paddles with a wave amplitude $a_0 = 0.0309$ m, period $T = 0.76$ s and incident

[2]Referenced by Rogers et al. (2004) but full text not available

[3]Referenced by Rogers et al. (2004) but full text not available

wave angle $\theta = 0°$. h_0, the water depth offshore of the beach toe is $h_0 = 0.218$ m. The minimum water depth is restricted to 1 mm to limit unrealistically high velocities at the shoreline and the simulation is run for 102 s. Three cases are considered: Case A uses a constant eddy viscosity of $\varepsilon = 0.005$ m^2/s with a fixed value of $C_f = 0.025$; Case B implements the variable eddy viscosity model outlined in Section 5.1.1 with $M_T = 1.0$ and $R_h = 0.001$ m; and Case C sets $\varepsilon = 0$ m^2/s and $C_f = 0.025$. The simulation CPU run time is approximately 24 minutes for each case.

For Cases A and B, the circulation pattern is fully developed by $t \approx 20$ s and remains stable for the duration of the simulation. Figures 5.3a and 5.4a show the period-averaged velocity vectors (averaged over a single wave period) for Case A and Case B respectively at $t = 60$ s which illustrate the circulation patterns predicted by the numerical model. Data are plotted at every fourth grid point for ease of visualisation. The corresponding stream-function contours for both cases are shown in Figures 5.3b and 5.4b. Both cases produce broadly similar results - a clockwise rotating primary circulation cell offshore of the middle of the basin. Case A is characterised by high shoreline velocities and a relatively weak primary gyre, whereas the flow in the primary gyre in Case B is significantly stronger while the shoreline velocities are close to zero. The variable viscosity and bed friction model (i.e. Case B) results in relatively high values of ε ($\approx 0.2 - 0.5$ m^2/s) near the shoreline leading to low velocities in this region, while offshore, $\varepsilon \approx 0$ m^2/s.

Setting $\varepsilon = 0$ m^2/s in Case C, while producing reasonable predictions of the evolving water surface profile, results in the current field appearing somewhat chaotic, with no settled circulation pattern developing. In a paper describing Boussinesq modelling of rip currents, Chen et al. (1999) attribute this phenomenon to the absence of a model for sub-grid turbulent processes. They conclude that a turbulence model is necessary to account for the influence wave-generated current fields has on flow patterns, and achieve good results by implementing a Smagorinsky-type turbulence model in their fully nonlinear Boussinesq equation set. The conclusions of Chen et al. are confirmed by this research.

In his experiments, da Silva Lima reports the centroid of the primary gyre as being

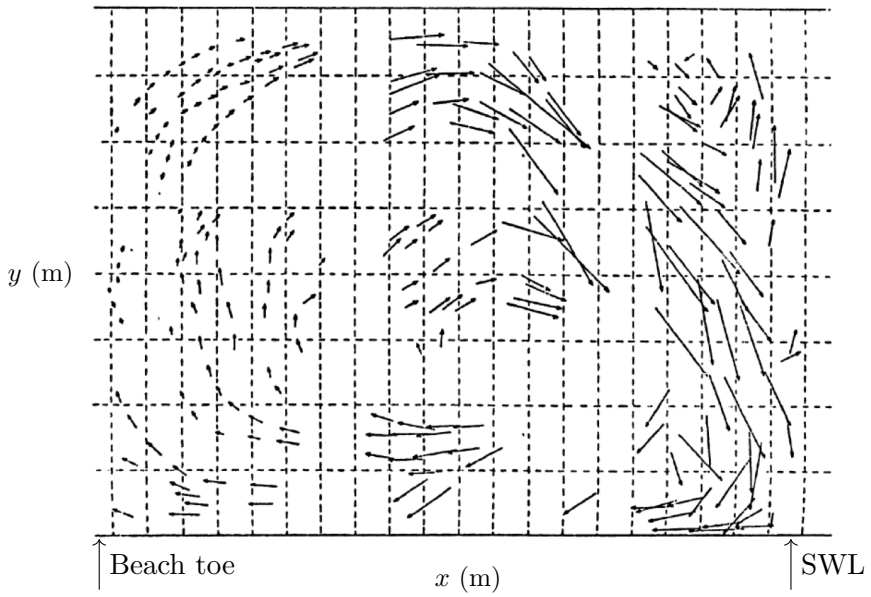

Figure 5.2: Nearshore circulation at a sinusoidal beach: Experimental velocities and measurement grid ($\Delta x = 0.2$ m, $\Delta y = 0.375$ m) from da Silva Lima (1981)

located approximately 1.7 m offshore of the still water line in the $x-$direction, and approximately 2.0 m from the northern boundary in the $y-$direction, as shown in Figure 5.2. While the numerical model predicts the circulation pattern with reasonable accuracy, the location of the main gyre is approximately 1.2 m further offshore compared with the experimental results, for both cases A and B. There are a number of possible reasons for this, including the calibration of the model, and how the switch between the Boussinesq and shallow water equation sets is applied. The equation set switch is triggered by either the slope of the water surface reaching a certain limit, or by the shallowness parameter μ, i.e. the ratio of the water depth to the wavelength. In the numerical simulation, breaking is not observed, so the switch is determined by the most offshore location where $\mu \leq 1/20$, which in this case is located at $x = 3.65$m and $y = 3$ m, along the northern boundary of the basin. As explained in Section 3.5, the switch point from non-breaking Boussinesq waves to broken waves described by the shallow water equations is applied at a given x-coordinate uniformly in the y-direction. Ideally, the switch point would follow the contours of the beach, varying from $x = 1.65$m at the northern boundary, between the 0.16 and 0.17 m contours in Figure 5.1, to $x \approx 0.7$m at

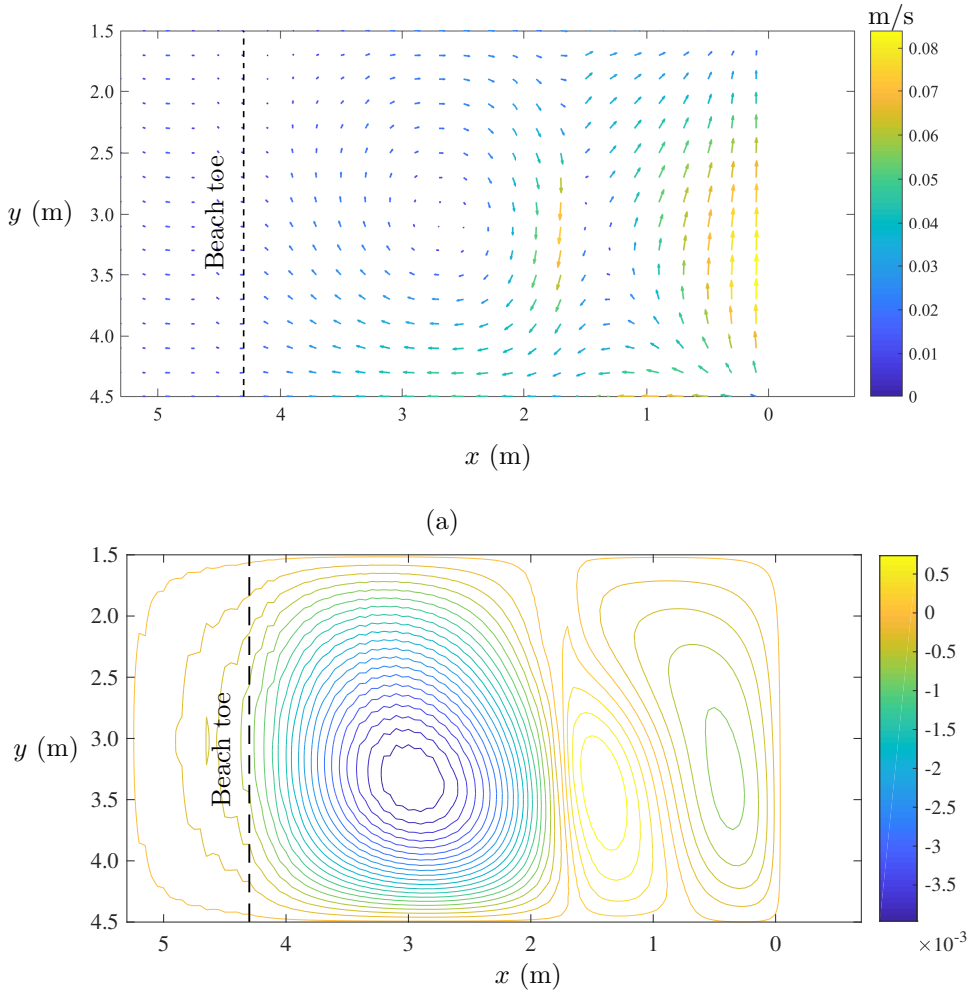

Figure 5.3: Nearshore circulation at a sinusoidal beach: Case A: (a) period-averaged velocity vectors at $t = 60$ s and (b) streamfunction contours at $t = 60$ s.

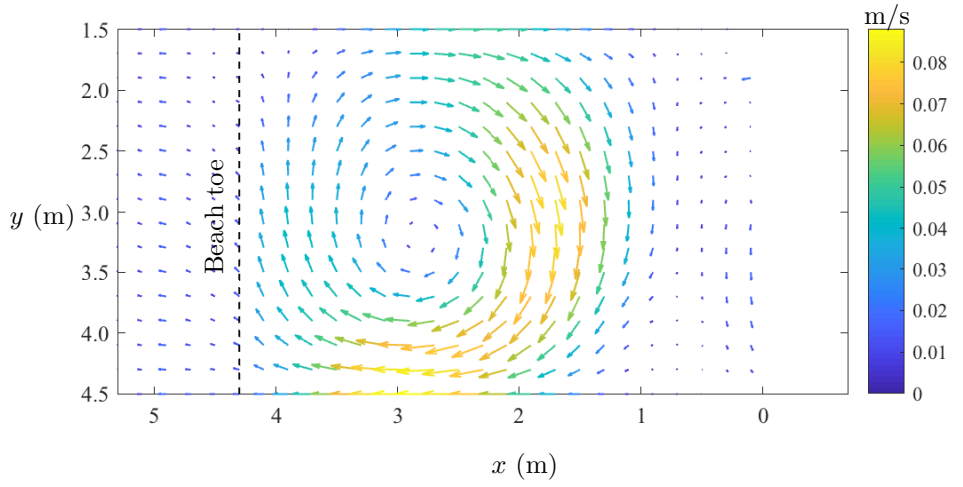

(a)

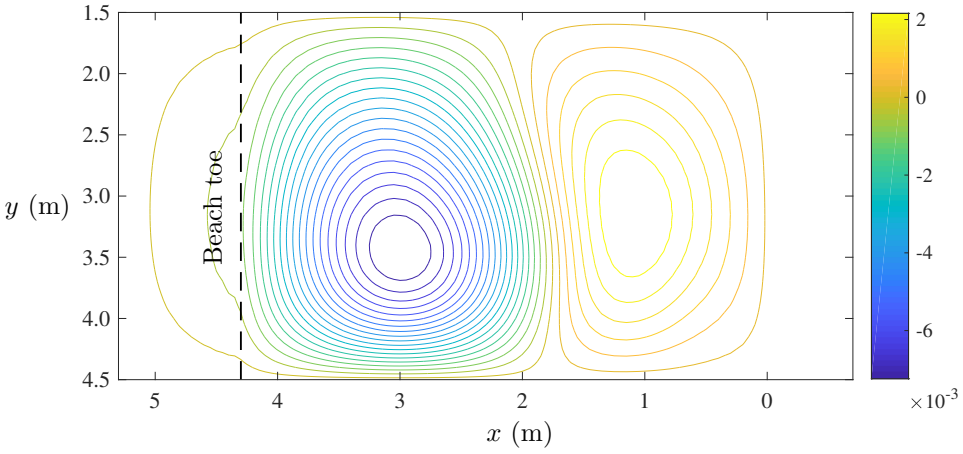

(b)

Figure 5.4: Nearshore circulation at a sinusoidal beach: Case B: (a) period-averaged velocity vectors at $t = 60$ s and (b) stream-function contours at $t = 60$ s.

the southern boundary. However the complexity of implementing this was beyond the scope of this research. Therefore, onshore of $x = 1.65$ m, the shallow water equations are applied uniformly across the numerical domain, despite the area of deeper water between $x = 0.7$ m and $x = 1.65$ m offshore of the still water line, and $y = 2$ m and $y = 4.5$ m. As a result, wave-current interaction is not adequately represented in this region as the governing shallow water equations are unsuited to this purpose. This is most likely the main reason for the shift in the centroid of the main gyre to a position further offshore than what was observed in the laboratory experiments.

The calibration of the model may also be a factor affecting the results. While the parameters, C_f and ε were varied for Case A, and similarly M_T and R_h for Case B, a detailed parameter study was not carried out. Other tunable parameters that may have influenced the numerical results are the local free-surface slope limit (set to $\Theta \geq 0.4$) which governs the equation set switch due to wave breaking, and the distance over which the Boussinesq dispersive terms are ramped down approaching the switch point (0.5λ). Improved results may also be achieved with a more sophisticated turbulence model.

5.2 Nearshore circulation at a tri-cuspate beach

Cuspate beaches represent a category of rhythmic shorelines commonly found at the coast, formed by the interaction between waves, currents and sediment. Borthwick and Foote (2002) present a series of laboratory experiments carried out at the UK Coastal research facility (UKCRF) to investigate the hydrodynamics of regular wave interaction with a fixed cuspate beach. For the experiments, a sinusoidal cuspate beach was constructed on the upper section of an otherwise 1:20 plane beach. Borthwick and Foote investigated the rip currents and circulation cells resulting from regular waves travelling normal to the cuspate beach, and the meandering longshore currents formed when the waves approach the shore at an oblique angle. Digital image analysis of video footage of neutrally buoyant markers was used in the experiments to determine the horizontal spatial patterns of the wave-induced currents, and measurements were also taken of the wave height field and the vertical structure of the rip and nearshore

currents. The experimental data obtained have been used by other researchers to verify numerical models, such as by Park and Borthwick (2001) and Rogers et al. (2004).

To investigate further the present numerical model's ability to simulate nearshore circulation over more complex bed topography, the model is applied to Borthwick and Foote's experiment involving regular waves travelling normal to the cuspate beach (Case B in their paper). The wave basin at the UKCRF has dimensions of 27 m cross-shore and 35 m alongshore with a working area of 20m by 15m. Waves are generated using 72 paddle wave-makers that can vary the angle of incidence from 0°to 30°. The beach toe is located 8.33 m from the paddles. At the cusps, the still water depth is given by

$$h_s(x,y) = s\left((x_L - x) - A\sin\left[\frac{\pi(x_L - x)}{x_L}\right]\left\{1 + \sin\left[\phi + \frac{2\pi y}{R}\right]\right\}\right) \tag{5.9}$$

In the above formula, s is the slope of the underlying plane beach, x_L is the cross-shore length of an individual cusp, x is the distance onshore from the toe of the cusp, A is an amplitude related to the cusp height, ϕ is a phase angle, y is the distance alongshore from the edge of the cusps, and R is the longshore length of an individual cusp. The values ascribed to the parameters for the numerical simulation are $s = 0.05$, $x_L = 5$ m, $A = 0.75$ m, $\phi = 3\pi/2$, and $R = 4$ m. The resulting bathymetry is illustrated in Figures 5.5 and 5.6.

The wave conditions simulated by the numerical model are regular waves with period $T = 1.2$ s, offshore height $H_o = 0.125$ m ramped up over a period of 10 s, and incident wave angle $\theta = 0°$. The numerical basin has dimensions of 20 m by 22 m in the $x-$ and $y-$directions respectively, with $\Delta x = \Delta y = 0.11$ m. The time step is set to $\Delta t = 0.01$ s and the simulation end time is set to 100 s. A constant eddy viscosity model is implemented, with $\varepsilon = 0.007$ m^2/s. The bed friction coefficient C_f is ramped down linearly from $t = 0$ to 10 s from an initially high value of 0.1 to target values of $C_f = 0.001$ at the cusps, and 0.02 elsewhere in the basin, in order to increase the model stability. The total simulation CPU run time is approximately 1 hour 35 minutes.

By $t \approx 20$ s, a circulation pattern begins to emerge, and is properly established by $t \approx 28$ s. Figure 5.8 shows the period averaged velocity vectors at $t = 40$ s, averaged over a single wave period, filtered to show every second point. The circulation pattern described by Borthwick and Foote (2002) and displayed in Figure 5.7 can clearly be

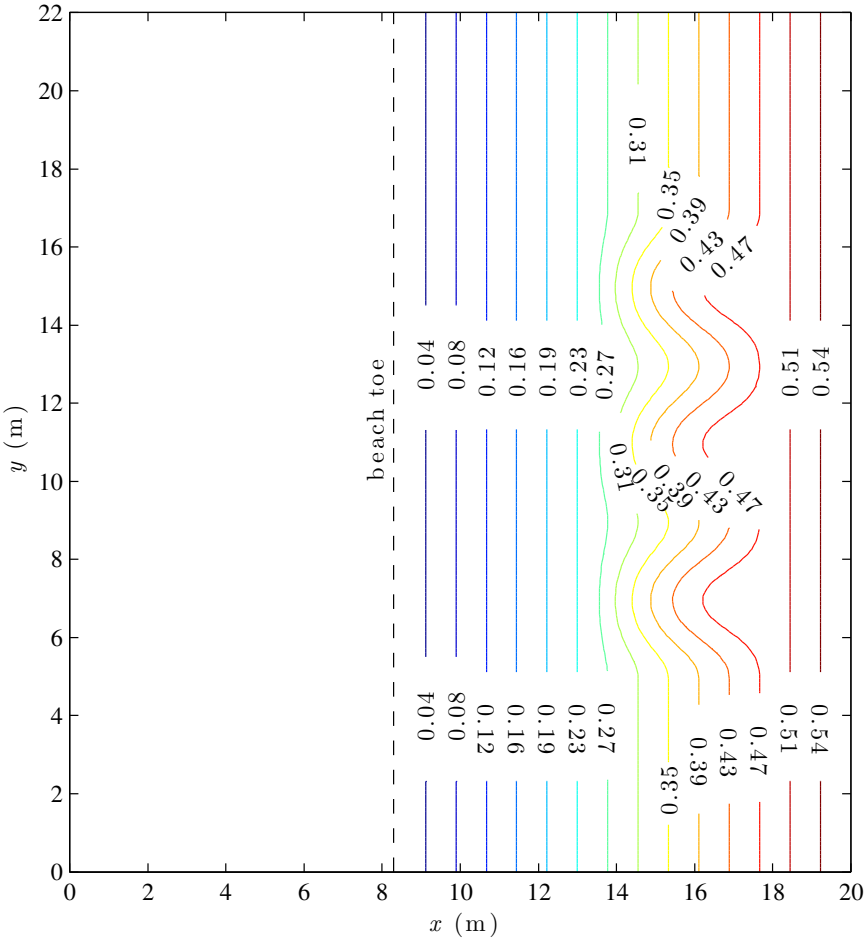

Figure 5.5: Tri-cuspate beach: bed elevation contours, rising from $z_b = 0$ m at the beach toe to 0.57 m at $x = 20$ m.

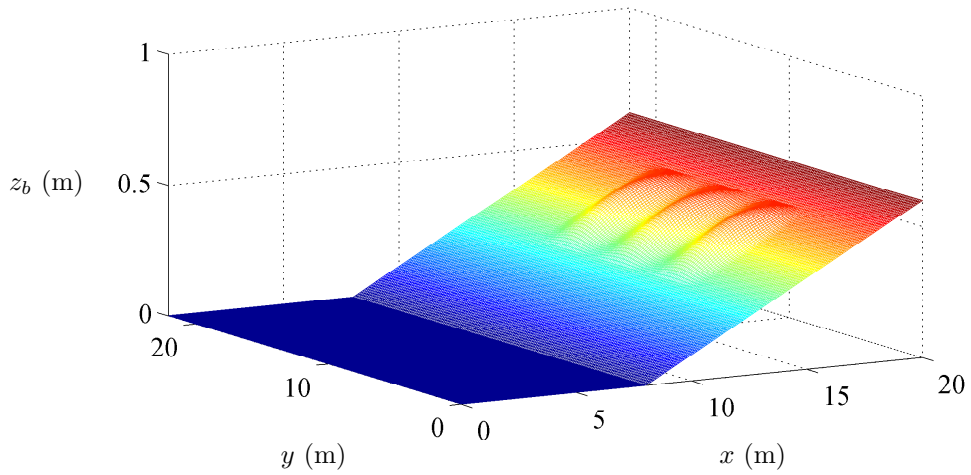

Figure 5.6: Tri-cuspate beach: 3D visualisation of basin bathymetry

observed, i.e. the counter-rotating pairs of circulation cells, as the water flows up over the cusp horns, and circulates back around to form seaward directed rip-currents in the embayments between the cusps. The acoustic Doppler velocimeters (ADVs) used to obtain the experimental velocity measurements could not be used in the very shallow water at the shoreline; however Borthwick and Foote report the presence of secondary circulation cells in this area, which are simulated numerically by Rogers et al. (2004). Figure 5.8 shows some circulation in this area predicted by the numerical model, however the cells are not clearly defined. This feature of the numerical results is most likely due to the shallow water equations governing in this region. The high shoreline velocities which characterise the constant eddy viscosity simulation of circulation at the half-sinusoidal beach in Section 5.1 are again present here, suggesting the need for a more sophisticated method of calculating C_f in this region.

In the numerical simulations, different values of C_f were tested in the range 0.001 to 0.01 at the cusps and between 0.01 and 0.03 in the rest of the domain, based on Borthwick and Foote's description of the construction of the cuspate beach. The eddy viscosity parameter ε was varied from 0 m^2/s to 0.01 m^2/s. For values of ε below 0.007 m^2/s, it was found that a stable circulation pattern failed to develop, again highlighting the need for an adequate representation of turbulent processes in the numerical scheme.

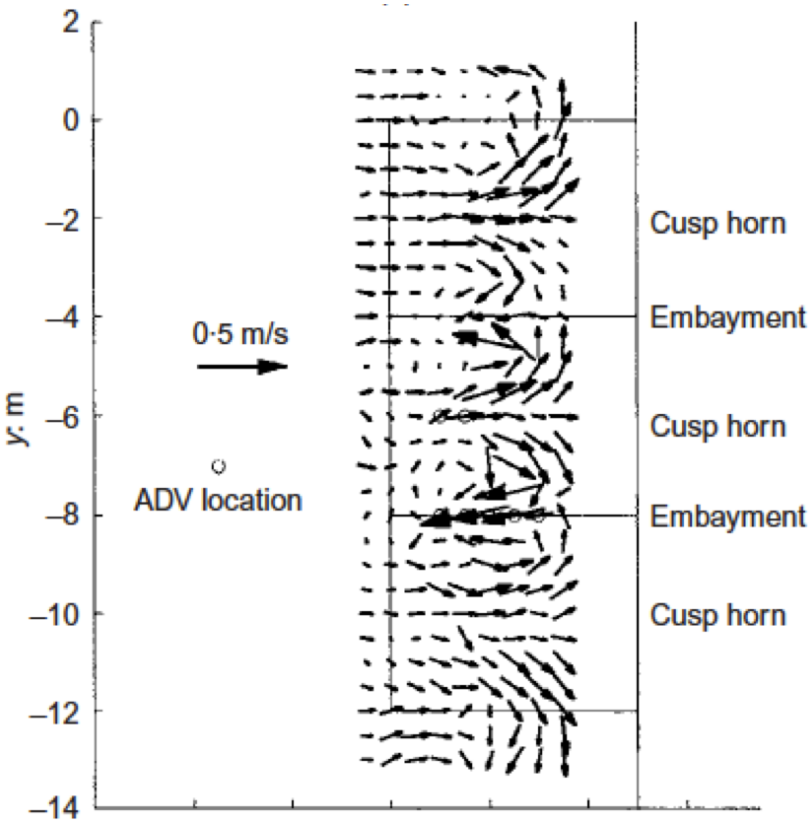

Figure 5.7: Tri-cuspate beach: period-averaged velocity field obtained in vicinity of the three cusps by interpolating measured velocities of floats (Borthwick and Foote (2002)). Offshore conditions are $T = 1.2$ s, $H_o = 0.125$ m and $\theta = 0°$

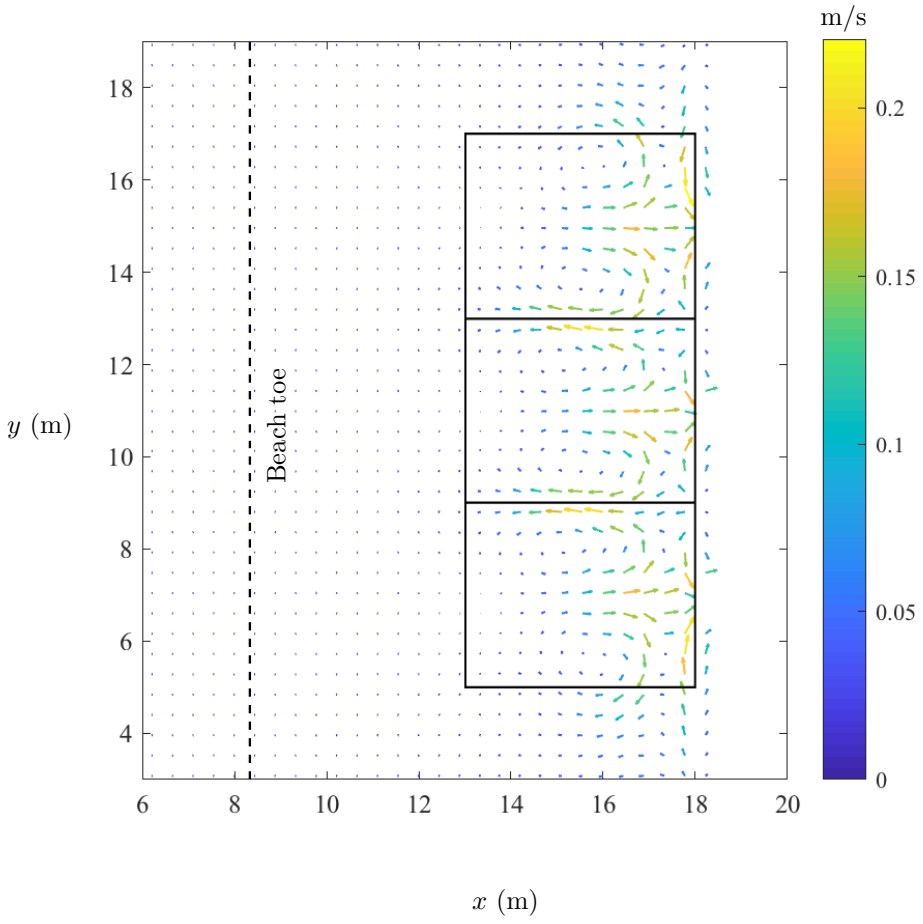

Figure 5.8: Tri-cuspate beach: Numerically predicted period-averaged velocity vector field at $t = 40$ s for offshore waves of $T = 1.2$ s, $H_o = 0.125$ m, and $\theta = 0°$

However, for higher values of ε, it was found that while the stable circulation patterns developed as per Borthwick and Foote's description, the velocities were very low, indicating excessively high energy losses. Attempts were made to implement the variable eddy viscosity model outlined in Section 5.1.1, but failed to achieve a combination of the grid resolution, R_h and M_T that allowed the model to run for a sufficient duration to achieve meaningful results in the time available for this research.

Neither the sinusoidal or tri-cuspate beach numerical simulations predicted wave breaking which was observed in both sets of laboratory experiments. By setting $\varepsilon = 0$ m^2/s, i.e. Case C in the sinusoidal numerical simulation, breaking was observed but as discussed previously, a stable circulation pattern failed to develop. Further research is needed to find a method that can model turbulent processes without excessive energy dissipation that prevents wave breaking from occurring, but produces realistic flow patterns.

5.3 Chapter summary

- In this chapter, numerical simulations are described that test the model's ability to reproduce the nearshore circulation patterns observed in the laboratory experiments of da Silva Lima (1981) and Borthwick and Foote (2002), namely, the interaction of regular waves with a half-sinusoidal beach and a tri-cuspate beach.
- The simulation of the interaction of regular waves with a half-sinusoidal beach demonstrates the numerical model's ability to reproduce the general circulation pattern observed in the experiment, while also revealing the need for a more two-dimensional treatment of the criterion for the switch between the governing equation sets.
- The tri-cuspate beach simulation again demonstrates the model's ability to predict nearshore circulation patterns, this time accurately positioning the counter-rotating primary circulation cells and seaward directed rip-currents.
- The results of the simulations show that the numerical model is capable of reproducing the circulation patterns observed in laboratory experiments involving

waves interacting with beaches with variable bathymetry. However, to become a reliable tool for simulating such behaviour, additional research is required to develop a more sophisticated criterion for the switch between governing equation sets, and to investigate the impact different turbulence models have on the model performance.

Chapter 6

Results II: Focused wave groups

In this chapter, results are presented of numerical simulations of focused wave groups interacting with a plane beach. Two generic types of focused wave group are considered: uni-directional; and multi-directional. Numerical predictions of the free surface motions of both types of wave group are compared to wave gauge data from the laboratory experiments of Hunt (2003) and Hunt-Raby et al. (2011) carried out at the UK Coastal Research Facility (UKCRF).

6.1 NewWave theory

Focused wave groups represent an efficient means for coastal engineers to model realistic large wave events at the coast, either numerically or in the laboratory. Other alternatives are regular waves, which being pure sinusoids do not properly model a realistic sea state, or irregular (random) wave simulations. The major drawback of the latter is the very long simulation duration required to produce an extreme event, which leads to problems of repeated wave reflections in laboratory experiments and a heavy computational load for numerical models.

A focused wave group is comprised of a number of individual sinusoidal wave components that come into phase at one point in time and space to produce a large event. NewWave is a methodology for ensuring the focused wave group corresponds to the average shape of the largest wave event in a Gaussian sea state, which is imperative

for accurate calculations of run-up and overtopping. The theory behind NewWave was first developed by Lindgren (1970) and independently by Boccotti (1983). Tromans et al. (1991) applied the concept to deepwater applications.

Using linear wave theory, the surface elevation at any time and any point in space of a uni-directional focused wave group is given by

$$\zeta(x,t) = \sum_{n=1}^{N} a_n \cos(k_n(x - x_f) - \omega_n(t - t_f) + \phi_n), \tag{6.1}$$

where N is the number of wave components, a_n is the wave amplitude, k_n is the wave number, ω_n is the angular frequency, and ϕ_n is the phase angle of the n-th component, x is distance, x_f is the focus location, t is time and t_f is the focus time.

For a spread sea, where the waves approach the focus location from a range of angles, the water surface elevation is given by

$$\zeta(x,y,t) = \sum_{n=1}^{N} a_n \sum_{m=1}^{M} b_m \cos(k_n((x - x_f)\cos\theta_m + y\sin\theta_m) - \omega_n(t - t_f) + \phi_n), \tag{6.2}$$

where M is the number of spreading angles, θ_m is the angle of the m^{th} component measured from the x-axis, and b_m is a spreading factor which is a function of θ. Different formulations exist for the spreading factor, such as the Gaussian or wrapped-normal function,

$$b(\theta) = \frac{1}{\sqrt{2\pi}\sigma_\theta} \exp\left[-\frac{1}{2}\frac{(\theta - \theta_p)^2}{\sigma_\theta^2}\right], \tag{6.3}$$

where σ_θ is the variance of the angular distribution and θ_p is the mean wave direction. Other formulations include the cosine-squared function,

$$b(\theta) = \begin{cases} \frac{2}{\pi}\cos^2\theta & \text{for } |\theta| \leq \frac{\pi}{2} \\ 0 & \text{for } |\theta| > \frac{\pi}{2}, \end{cases} \tag{6.4}$$

and top hat function,

$$b(\theta) = c, \tag{6.5}$$

where c is a constant. All formulations must meet the requirement

$$\sum_{m=0}^{M} b_m = 1. \tag{6.6}$$

Focused wave groups are created in the laboratory by offsetting individual wave components at the paddles to account for the variation in propagation speeds. At the focus location, constructive interference between the individual wave components produces a large, energetic wave group. Away from the focus location, the wave group is less compact with a smaller amplitude, due to the effects of frequency dispersion.

According to NewWave theory, the surface water profile in the vicinity of an extreme wave matches the normalised autocorrelation function of the underlying sea spectrum, premultiplied by the crest height. Jonathan and Taylor (1997) verified NewWave against large waves in deep water whereas Taylor and Williams (2004) undertook a similar exercise for waves in intermediate depth. Thus for a crest-focused wave, the NewWave time history is given by

$$\zeta(t) = \frac{A_{\mathcal{N}}}{\sum_n S_n(\omega)\Delta\omega_n} \sum_n S_n(\omega)\Delta\omega_n \cos(\omega_n(t - t_f)), \tag{6.7}$$

where $S_n(\omega)$ is the discretised underlying energy spectrum and $\Delta\omega_n$ is the angular frequency resolution. $A_{\mathcal{N}}$ represents the linear amplitude of the largest wave from a sea surface time series of $\mathcal{N}$ waves and is calculated from $A_{\mathcal{N}} = \sqrt{2\sigma^2(\ln(\mathcal{N})}$, where $\mathcal{N}$ is the number of waves and σ^2 is variance of the free-surface time-series.

Thus, the wave component amplitudes necessary to generate NewWave in equation (2.59) are given by

$$a_n = \frac{A_{\mathcal{N}} S_n(\omega)\Delta\omega_n}{\sum_n S_n(\omega)\Delta\omega_n}. \tag{6.8}$$

The underlying energy spectrum, $S_n(\omega)$, represents a mathematical description of a real sea state, which is composed of many different waves with different amplitudes, phases and frequencies, propagating in different directions. It is obtained using the concept of a wave spectrum, which gives the distribution of wave energy density with frequency. The energy density is the total energy within a particular frequency interval, given by $\frac{1}{2}\rho g a^2$ where a is the wave amplitude. There are various spectra used in ocean engineering obtained as fits to ocean data, including the Pierson-Moskowitz (PM) spectrum for a fully developed sea at a particular wind speed, given by

$$S(\omega) = \left(\frac{\omega_p}{\omega}\right)^5 \exp\left(-1.25\left(\frac{\omega_p}{\omega}\right)^4\right), \tag{6.9}$$

where ω is the angular frequency. The peak angular frequency $\omega_p = g/U_{19.5}$, where $U_{19.5}$ is the characteristic wind velocity measured at 19.5 m above still water level.

6.2 NewWave Experiments at the UKCRF

Experiments undertaken at the UKCRF using focused wave groups are described by Hunt (2003) and Hunt-Raby et al. (2011) where NewWave theory was implemented to generate 32 different focused wave groups with varying amplitudes and phases. The experiments involved both uni-directional wave groups (WG1-WG16) and directionally spread wave groups (WG17-WG32) interacting with a plane beach and a sea wall. The uni-directional wave group tests covered both normally incident and oblique wave trains. Crest-focused and trough-focused wave groups were also considered. Focus locations included: the beach toe, 3/4 depth (i.e. 1/4 of the way up the beach), and 1/2 depth. Tables 6.1 and 6.2 summarise details of the selected wave groups considered in this research.

Detailed measurements were made by Hunt and her co-workers of the water surface elevation profile, run-up and overtopping, and wave particle kinematics. The underlying energy spectrum used in the experiments was a Pierson-Moskowitz spectrum, given by equation (6.9) in which the peak angular frequency $\omega_p = 2.91$ rad s^{-1} (0.46 Hz). The truncated spectrum was defined by $\omega_{min} \approx 2.07$ rad s^{-1} (0.33 Hz) and $\omega_{max} \approx 6.06$ rad s^{-1} (0.96 Hz). This spectrum was discretised into $N = 53$ components with a uniform angular frequency resolution of $\Delta\omega \approx 0.077$ rad s^{-1} (0.012 Hz). Paddle signals were calculated according to equation (2.59), with an experimentally derived transfer function used in place of the Biésel transfer function c_0. A detailed explanation of the paddle calibration procedure is given in Chapter 4 of Hunt (2003).

The wave basin at the UKCRF has internal plan dimensions of 20 m x 36 m in the $x-$ and $y-$directions respectively. Waves are generated by a 72 independently operated piston paddles, each 0.5 m wide and 1.5 m high. The toe of a 1:20 plane beach is located 8.33 m from the paddles. The water surface elevation in the UKCRF experiments was measured using wave gauges positioned both offshore and in the surf zone. Details of the paddle and wave gauge calibration procedure are given by Hunt

Uni-directional wave groups (Hunt (2003))				
Name	Input amplitude (mm)	Focus location	Angle of incidence (deg)	Phase of group (rad)
WG1	114	beach toe	0	0
WG2	114	$\frac{3}{4}$ depth	0	0
WG3	90	$\frac{1}{2}$ depth	0	0
WG5	114	beach toe	0	π
WG6	114	$\frac{3}{4}$ depth	0	π
WG7	90	$\frac{1}{2}$ depth	0	π

Table 6.1: Selected uni-directional wave group tests in the UKCRF (Hunt (2003))

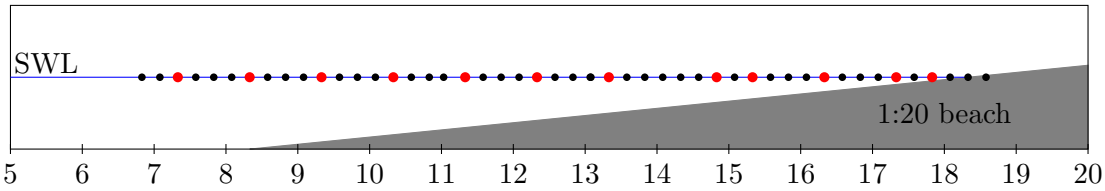

Figure 6.1: Gauge locations for the UKCRF run-up experiments reported by Hunt (2003). The gauge locations highlighted in red are used to compare numerical and measured data in sections 6.2.1 and 6.2.2

(2003). Measurements were made at 250 mm intervals along the centre-line of the basin, from 1.5 m offshore of the beach toe ($x = 6.83$ m) to $x = 18.33$ m. The gauge locations are illustrated in Figure 6.1. The resulting experimental data have been used to verify numerical models described by Borthwick et al. (2006), Orszaghova (2011) and Orszaghova et al. (2012).

6.2.1 Uni-directional focused wave group

The numerical model is used to simulate WG1 of the UKCRF tests: a crest-focused wave group with linear focus amplitude of $A_f = 0.114$m, focus location at the beach toe ($x = 8.33$m) and a plane beach topography with still water depth $h = 0.5$ m. The

Multi-directional wave groups (Hunt (2003))				
Name	Input amplitude (mm)	Focus location	Spread angle (deg)	Phase of group (rad)
WG17	114	beach toe	±30	0
WG18	114	$\frac{3}{4}$ depth	±30	0
WG19	90	$\frac{1}{2}$ depth	±30	0
WG21	114	beach toe	±30	π
WG22	114	$\frac{3}{4}$ depth	±30	π
WG23	90	$\frac{1}{2}$ depth	±30	π
WG25	114	beach toe	±10	0
WG26	114	$\frac{3}{4}$ depth	±10	0
WG27	90	$\frac{1}{2}$ depth	±10	0
WG29	114	beach toe	±10	π
WG30	114	$\frac{3}{4}$ depth	±10	π
WG31	90	$\frac{1}{2}$ depth	±10	π

Table 6.2: Selected multi-directional wave group tests in the UKCRF (Hunt (2003))

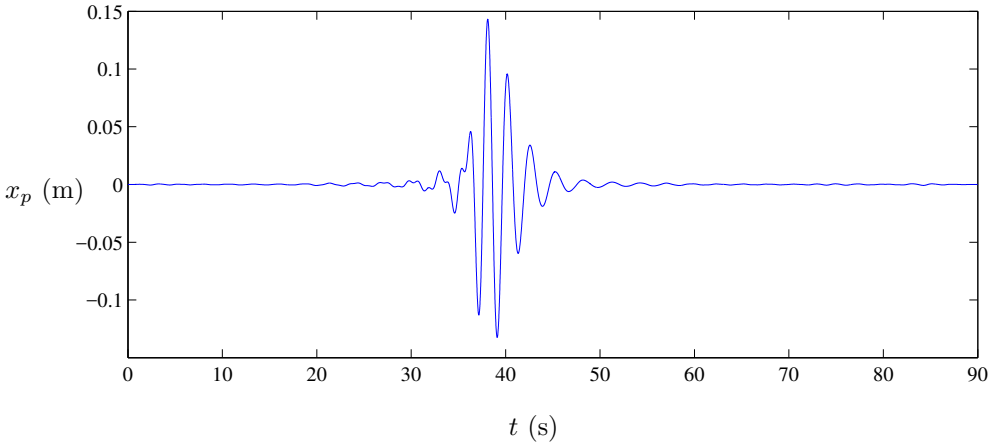

Figure 6.2: Paddle signal time series for uni-directional focused wave group in the UKCRF (WG1)

114 mm wave amplitude is the largest in the series of experiments undertaken at the UKCRF. The wave group is generated numerically using the paddle displacement signal from the laboratory experiments, shown in Figure 6.2. The actual (laboratory) paddle signal was calculated at a temporal resolution of $\Delta t = 0.05$ s, and so it is interpolated to obtain a signal with the desired computational time step of $\Delta t = 0.007$ s. To generate a normally incident wave group, the same signal is applied across all paddles. Although the UKCRF basin has a long-shore dimension of 36 m, the numerical basin is set to 1 m wide to reduce the computational load, while the onshore dimension in the x-direction is set to 22 m. Thus the computational domain is 22m x 1 m and mimics a wave flume rather than the whole basin, which is sufficient for modelling waves travelling normal to the beach. The grid size is set to $\Delta x = \Delta y = 0.04$ m, the time step is $\Delta t = 0.007$ s and the simulation is run for 90 s, which corresponds to the total paddle signal duration. The eddy viscosity ε parameter is set to 0 m^2/s and the bed friction coefficient $C_f = 0.008$. The simulation CPU run time is approximately 1 hour.

Figure 6.3 illustrates the predicted water surface distribution along the numerical flume as the wave group focuses at the toe of the beach at $t = 45.5$ s. Figure 6.4 presents plots of the predicted free-surface profile at four different times, showing the evolution of the focused wave group after focus. The red line indicates the paddle

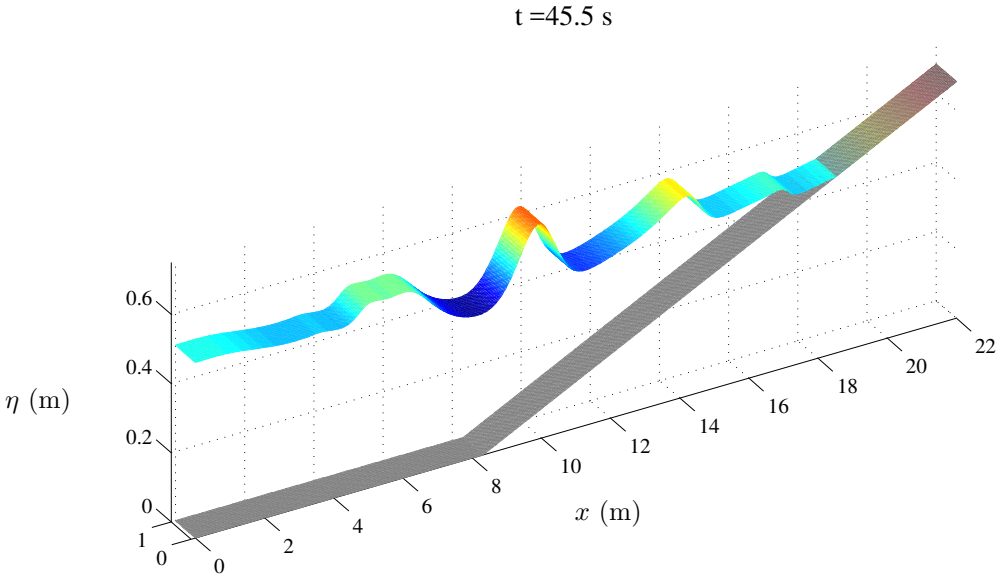

Figure 6.3: 3D visualisation of the predicted surface water elevation profile of the unidirectional focused wave group WG1 in the UKCRF at $t = 45.5$ s

position, while the dashed green line represents the switch point between the governing Boussinesq (BE) and nonlinear shallow water (NSWE) equation sets.

Figures 6.5 and 6.6 compare the experimentally measured and numerically predicted free-surface elevation time series at a total of 12 wave gauge locations. Leading waves in the wave group are predicted to very high accuracy across all the wave gauge locations. In the deeper water, before the waves break, the numerical model under-predicts the height of the central wave crest, and over-predicts the trough depths at either side, in particular the trailing trough, compared with the experimental measurements. The reason for this discrepancy is unknown, but it may be due to nonlinear behaviour that is not adequately represented by the weakly nonlinear governing equations. The wave breaking location, and the propagation of the broken waves is predicted with reasonable accuracy. A slight phase lag in the wave propagation is evident in Figure 6.6, where the numerically predicted bores appear to travel slower than the waves observed in the laboratory. In general, the mismatch between the numerical prediction and the experimental data mirrors that reported by Orszaghova (2011) for the one-dimensional model, and may be attributed to limitations in the underlying shallow

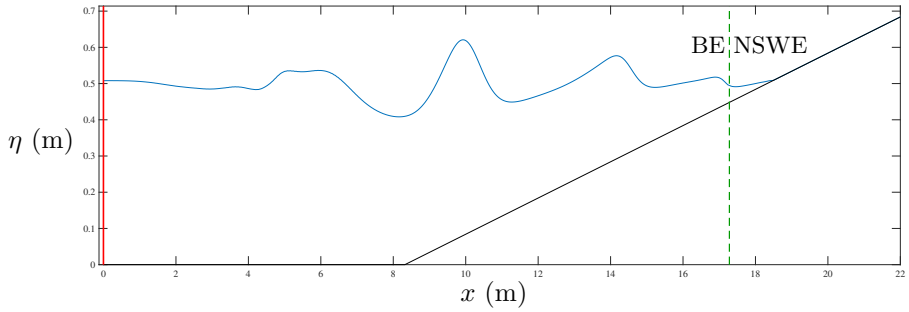

(a)

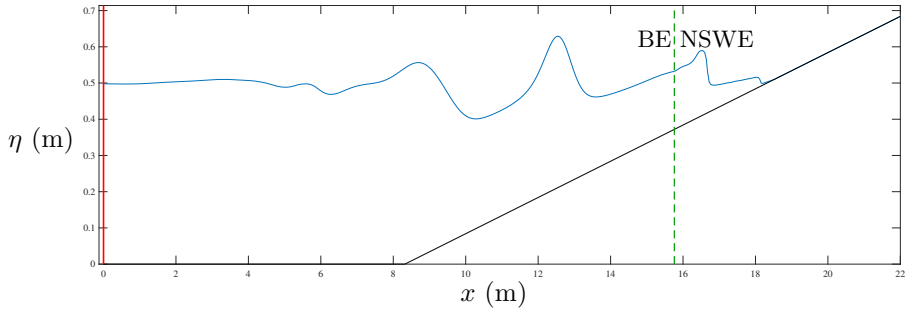

(b)

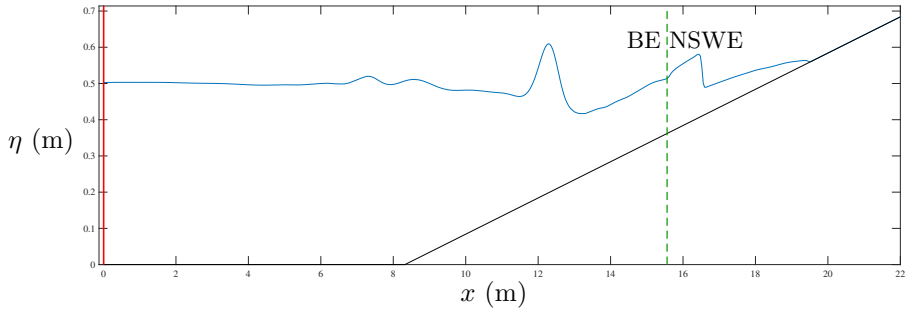

(c)

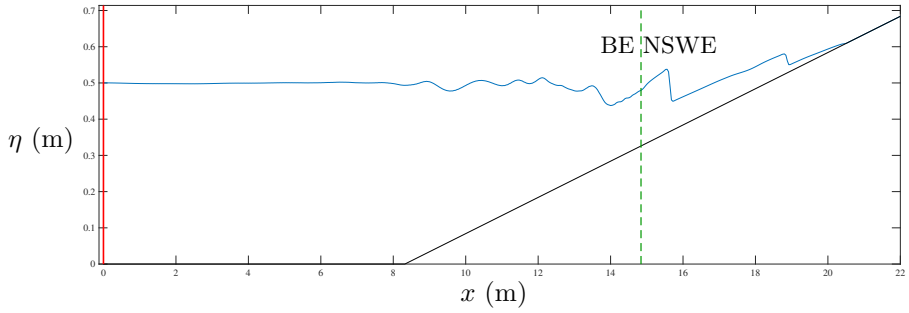

(d)

Figure 6.4: Numerically predicted water surface elevation profiles (side-on view) in the UKCRF at (a) $t = 45.5$ s; (b) $t = 46.9$ s; (c) $t = 49$ s; and (d) $t = 51.1$ s.

water equations (discussed further in section 6.2.2). Overall, the numerical model performs well, capturing the evolution of the wave group from the paddle face through to wave breaking and formation of bores.

6.2.2 Multi-directional focused wave group

The directionally spread wave group experiments at the UKCRF reported by Hunt (2003) included waves with a top-hat spread angle of ±10°and ±30°. The test case of a multi-directional focused wave group with spread angle ±30°, linear focus amplitude of $A_f = 0.114$ m and focus location at the beach toe, is now considered (WG17 in Hunt (2003)). In the UKCRF experiments, the number of spreading angles in equation (6.2) was $M = 81$, and the number of wave components $N = 53$. A top-hat spreading factor was used, where $b(\theta) = 1/M$. As with the uni-directional case, the waves are generated in the numerical model using the paddle displacement signals from the laboratory experiments. Here, the computational domain matches the internal basin measurements of 20 m x 36 m, with the grid spacing in the x-direction set to $\Delta x = 0.05$ m. As there are 72 paddles in the UKCRF basin, each paddle is modelled with 10 grid points in the y-direction, giving $\Delta y = 0.0501$m. The simulation is run for 90 s to match the laboratory experiment, with a time step of $\Delta t = 0.01$ s. Linear interpolation is again performed on the experimental paddle signal to produce signals with a time step matching that of the numerical model. The eddy viscosity parameter is set to $\varepsilon = 0$ m^2/s, and the bed friction coefficient $C_f = 0.008$. The simulation CPU run time is approximately 17 hours 45 minutes (compiled using gfortran with -O3 optimisation on a late 2011 MacBook Pro with 2.3 GHz Intel Core i5 processor executing 3 threads).

In early stages of the simulation, the amplitudes of the paddle motions are low, sending small waves across the basin. The paddle amplitudes gradually increase, producing larger amplitude wave components, with all waves coming into phase at the beach toe at $t \approx 46$ s, producing a large wave event. Figure 6.7 illustrates the evolution of the free-surface profile during the simulation.

Figures 6.8 and 6.9 compare the laboratory measurements and numerical predictions of the free-surface elevation time series at 12 gauge locations in the UKCRF for

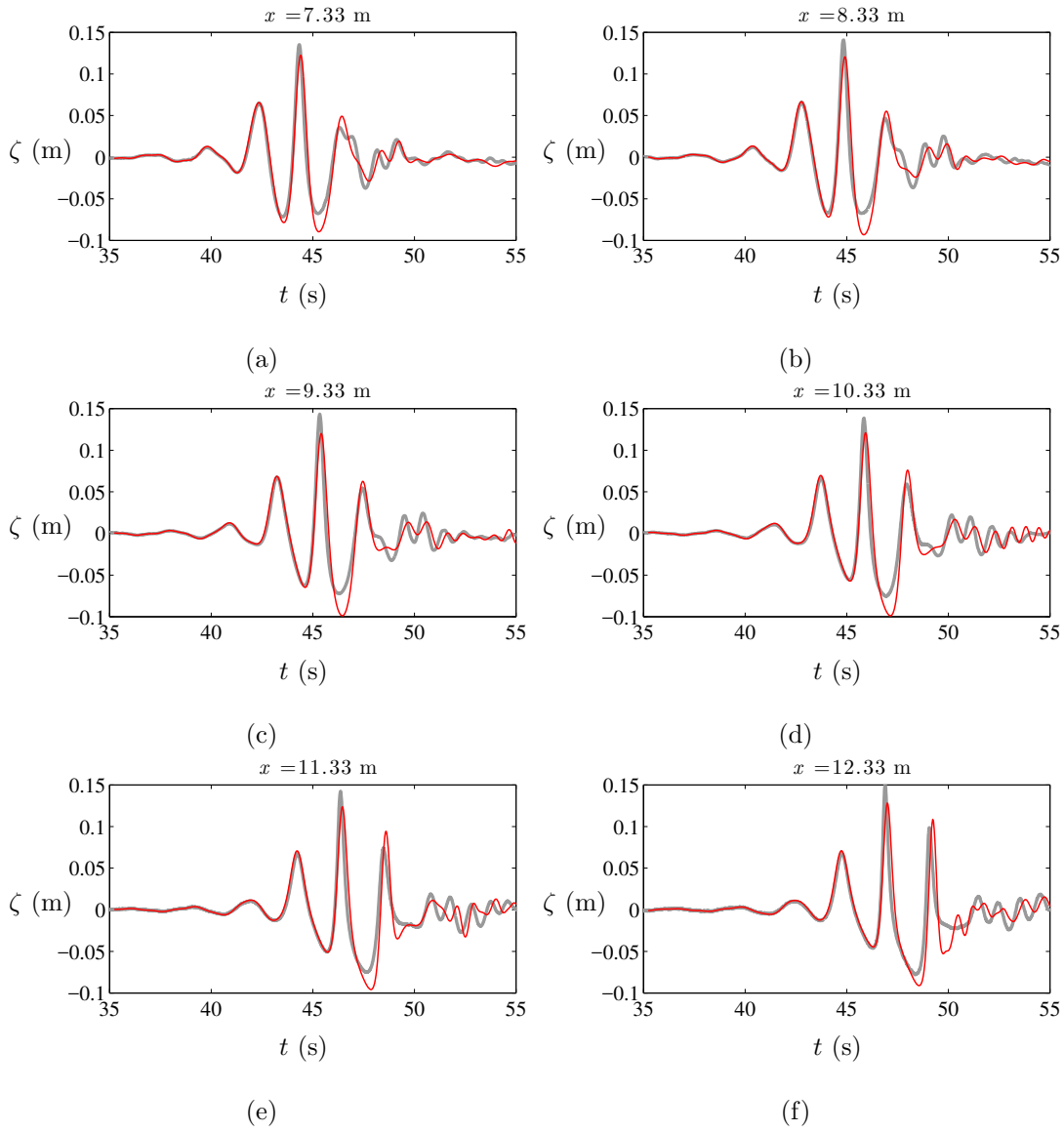

Figure 6.5: WG1 - Crest focused uni-directional wave group time series in the UKCRF: Comparison between measured wave gauge data (thick grey line) and numerical prediction (red line) at selected gauge locations

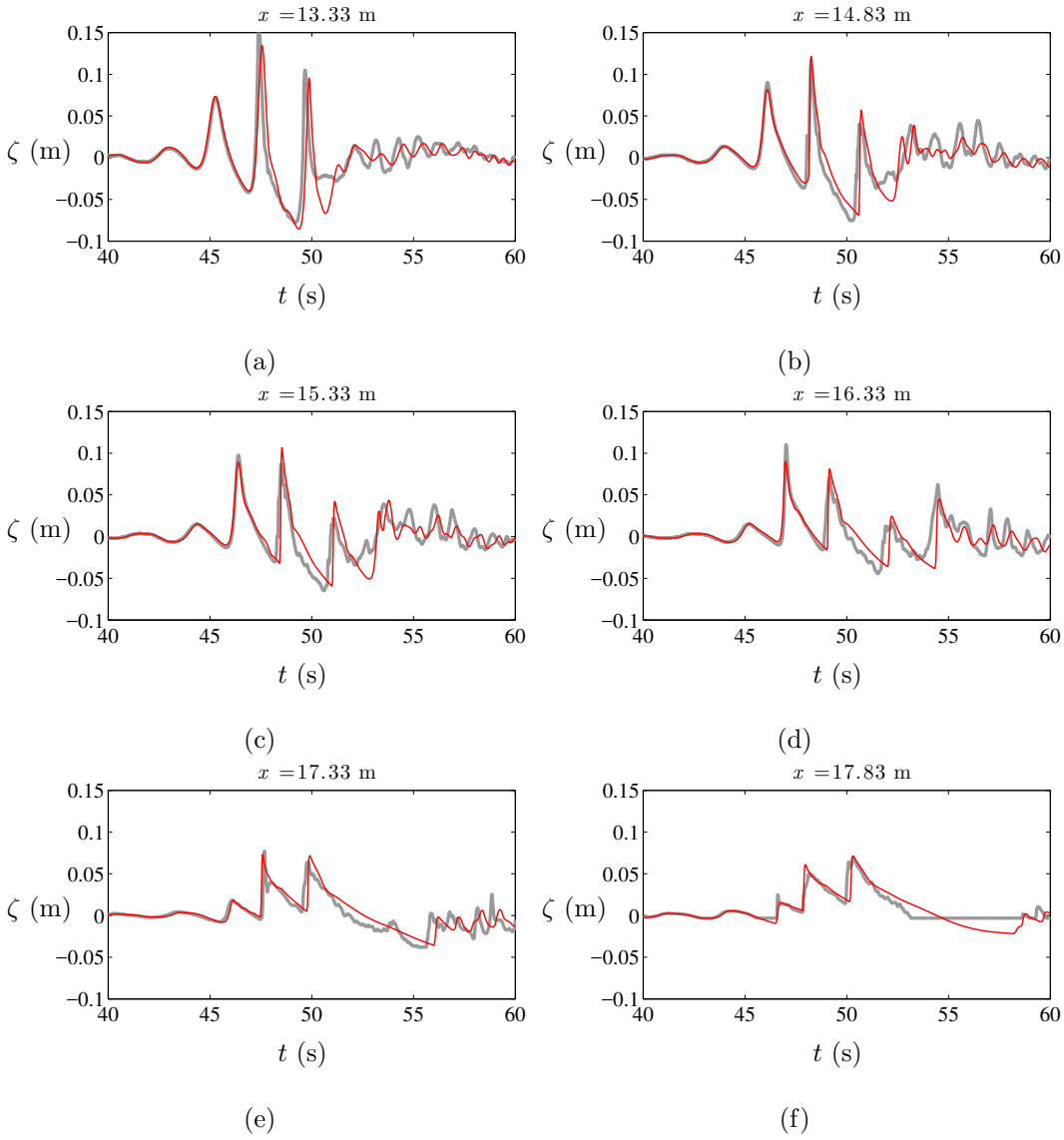

Figure 6.6: WG1 - Crest focused uni-directional wave group time series in the UKCRF: Comparison between measured wave gauge data (thick grey line) and numerical prediction (red line) at selected gauge locations

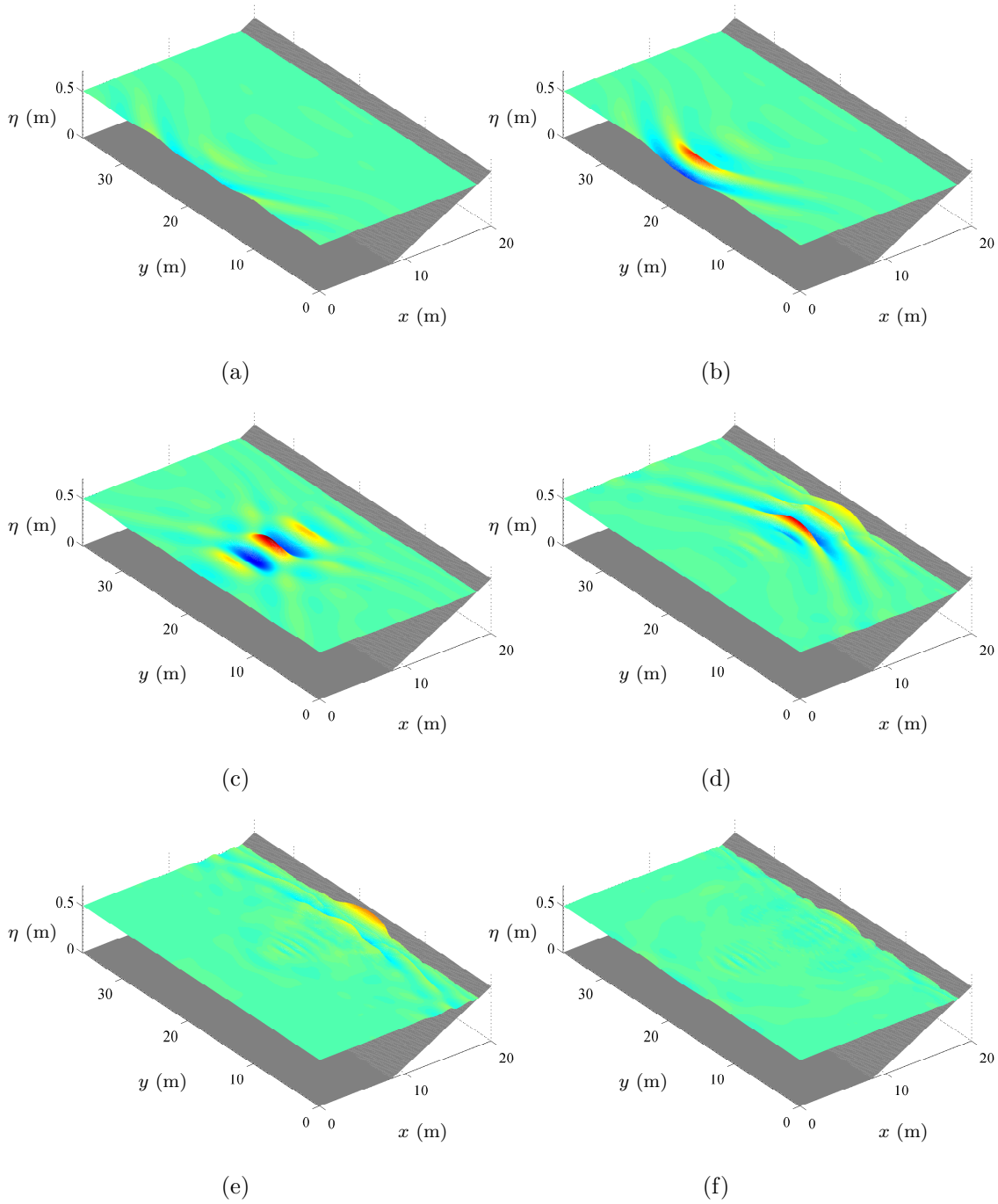

Figure 6.7: Numerically predicted water surface elevation for ±30°spread multi-directional focused wave group (WG17) in the UKCRF at: (a) $t = 38$ s; (b) $t = 40$ s; (c) $t = 45$ s; (d) $t = 50$ s; (e) $t = 55$ s; and (f) $t = 60$ s.

the crest-focused wave group WG17. The performance of the model for the multi-directional wave group is very similar to the uni-directional case: again the leading waves of the wave group are predicted with excellent accuracy, while pre-breaking, the height of the central wave crest in the group is under-predicted, and the trough following this crest is over-predicted. The transformation to a steep-fronted bore is captured very well, as shown in Figure 6.9, while the slight phasing mismatch is again present in the bore propagation in very shallow water. Figures 6.10 and 6.11 present similar comparisons for the trough-focused wave group WG21.

The phasing mismatch for both the uni-directional and multi-directional wave groups may be attributed to use of the shallow water equations to model the propagation of waves in the surf zone. Linear wave theory relates the speed of propagation (phase speed or celerity) of surface gravity waves to the wave number and angular frequency by

$$c^2 = \frac{\omega^2}{k^2} = \frac{g}{k}\tanh(kh). \tag{6.10}$$

In shallow water ($kh < \pi/10$), equation (6.10) reduces to

$$c = \sqrt{gh}. \tag{6.11}$$

However research has shown that this shallow water approximation under-predicts the observed phase speed of waves in the surf zone in both the field (e.g. Inman et al. (1971), Thornton and Guza (1982), Martins et al. (2015)) and in laboratory experiments (e.g. Svendsen et al. (1978), Stive (1980), Catálan and Haller (2008)). Several researchers (e.g. Schäffer et al. (1993) and Madsen et al. (1997)) have used a modified shallow water approximation of the phase speed in the surf zone given by

$$c = a\sqrt{gh}, \tag{6.12}$$

where a is a constant to be determined and typically has a value of $a = 1.3$. This value is consistent with surf zone measurements made in the laboratory by Stive (1980).

6.2.3 Run-up analysis of focused wave groups

Run-up is defined as the instantaneous elevation of the water surface above still water level (Figure 6.12). It is thus a vertical rather than a horizontal measure. Accurate

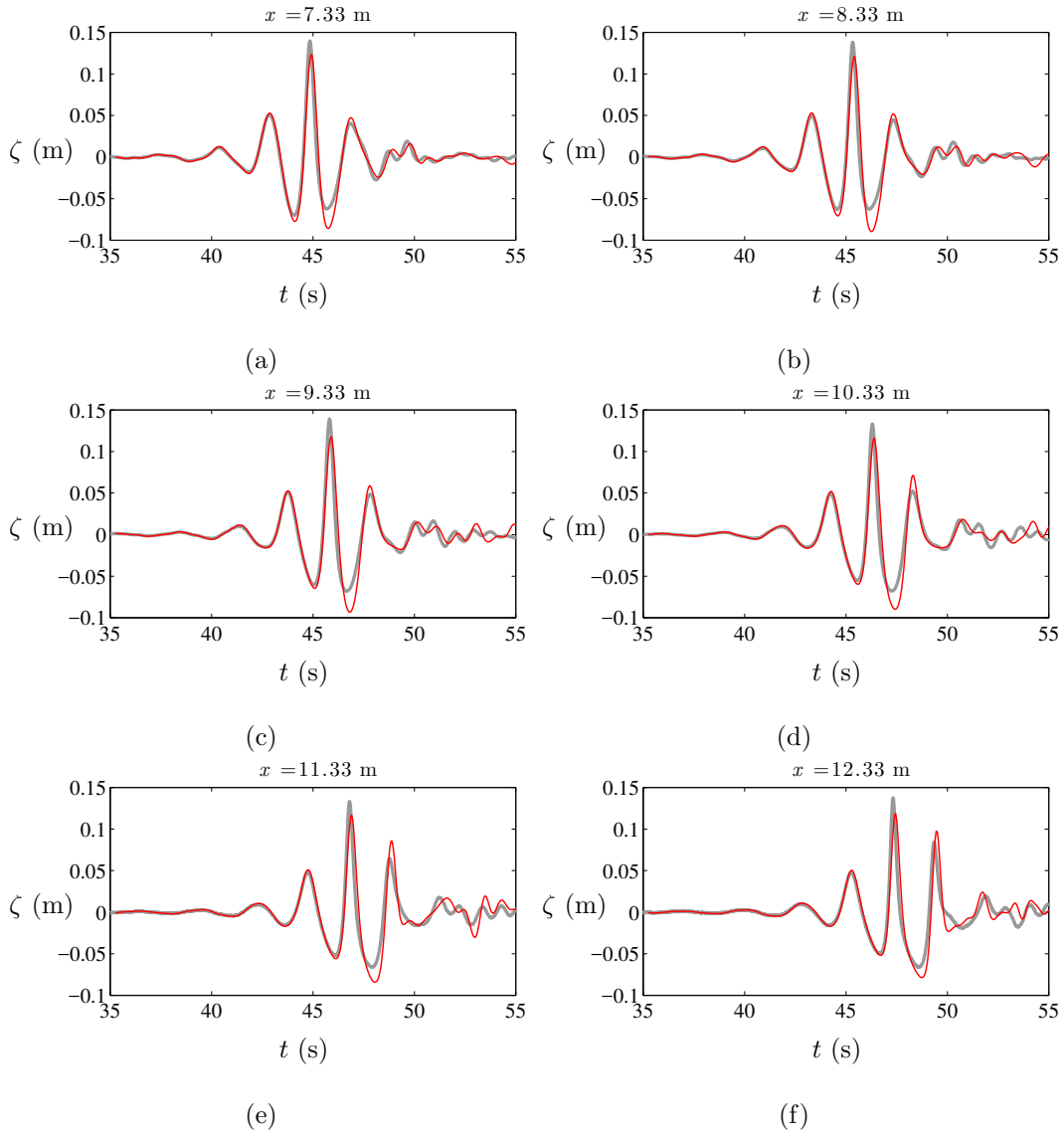

Figure 6.8: WG17 - Crest focused multi-directional wave group (±30°spread) in the UKCRF: comparison between deep water gauge measured (thick grey line) and numerically predicted (red line) free-surface elevation time series at six gauge locations from $x = 7.33$ to $x = 12.33$ m.

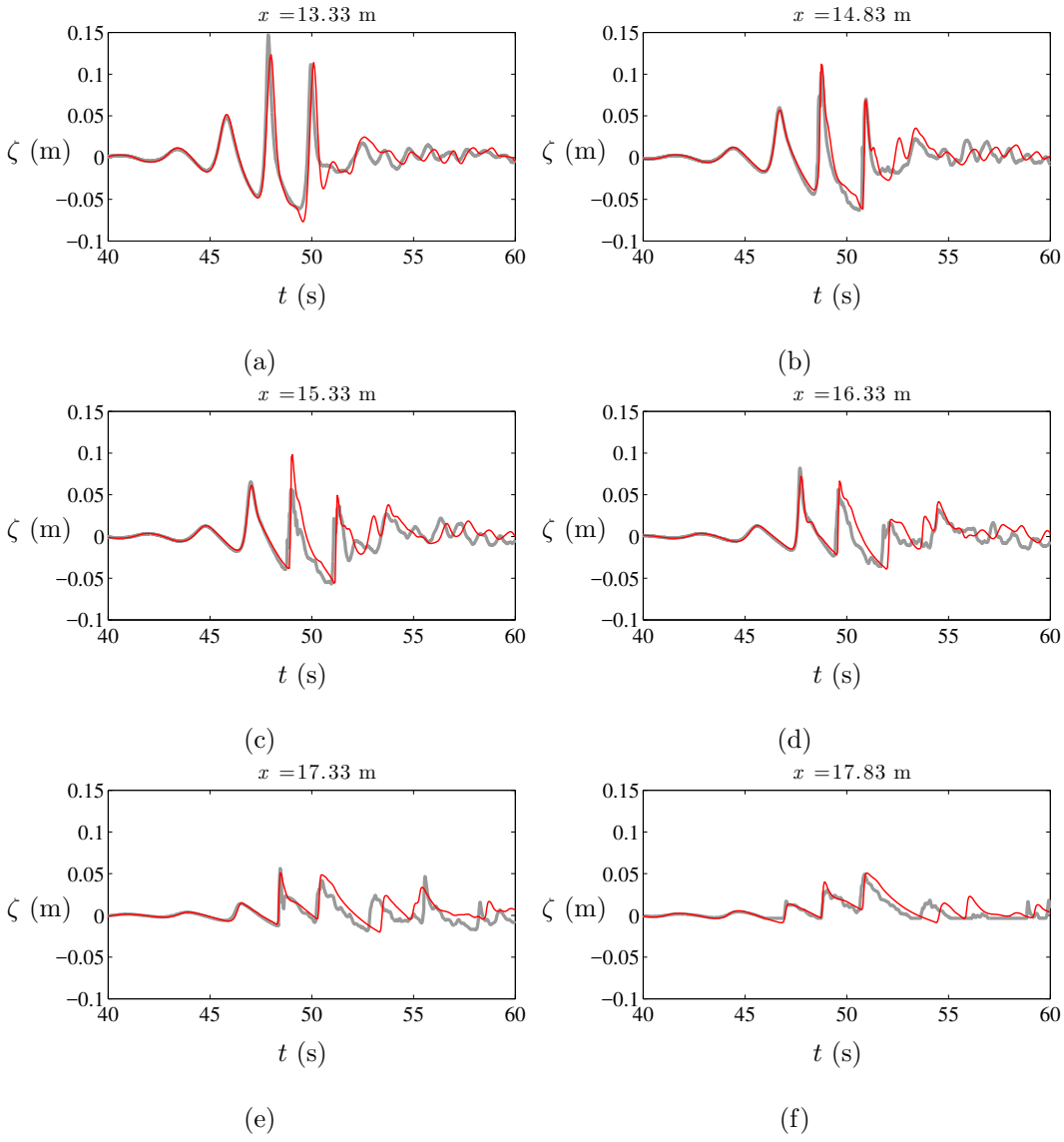

Figure 6.9: WG17 - Crest focused multi-directional wave group (±30°spread) in the UKCRF: comparison between shallow water gauge measured (thick grey line) and numerically predicted (red line) free-surface elevation time series at six gauge locations from $x = 13.33$ to $x = 17.83$ m.

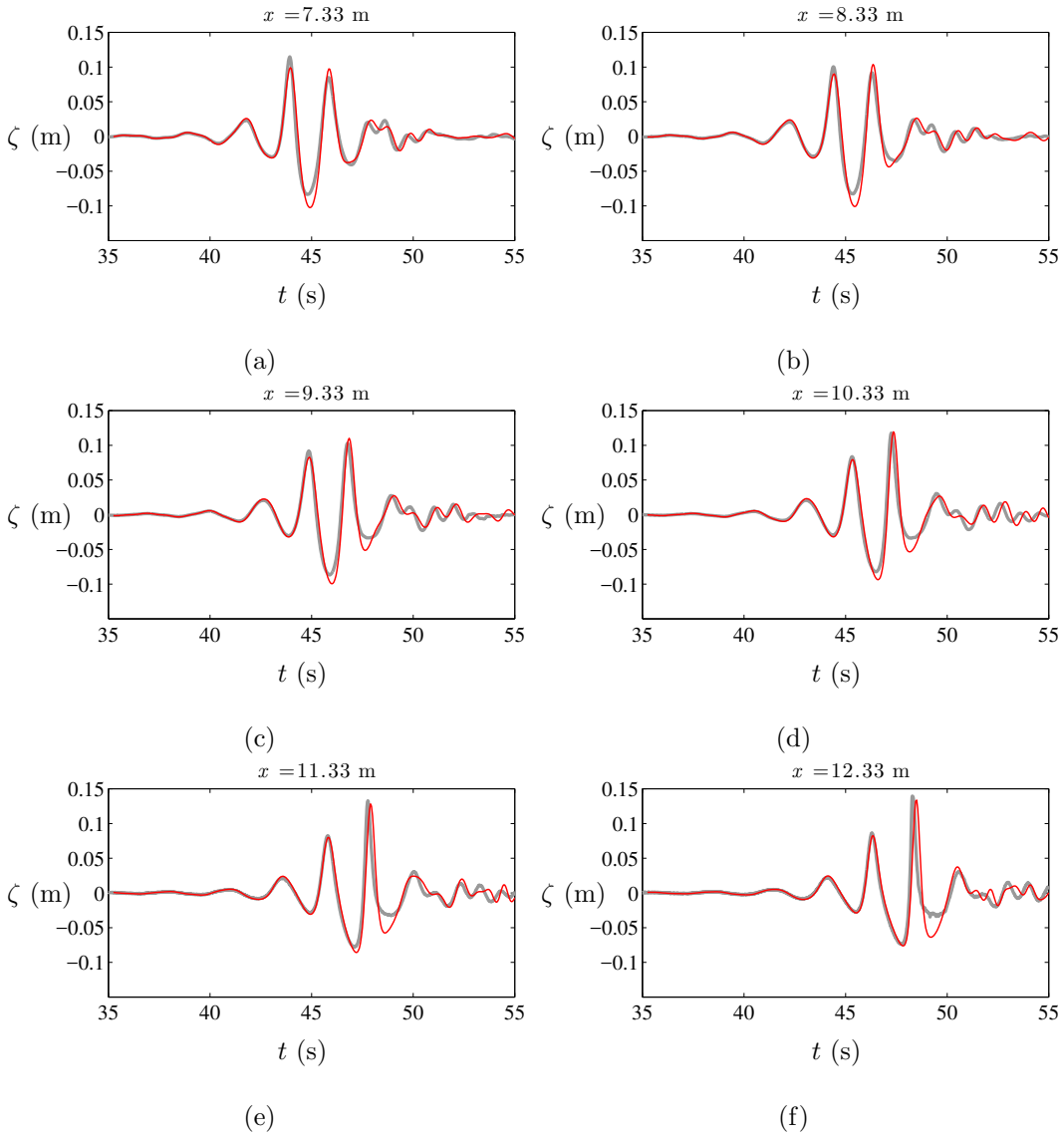

Figure 6.10: WG21 - Trough focused multi-directional wave group (±30°spread) in the UKCRF: comparison between deep water gauge measured (thick grey line) and numerically predicted (red line) free-surface elevation time series at six gauge locations from $x = 7.33$ to $x = 12.33$ m.

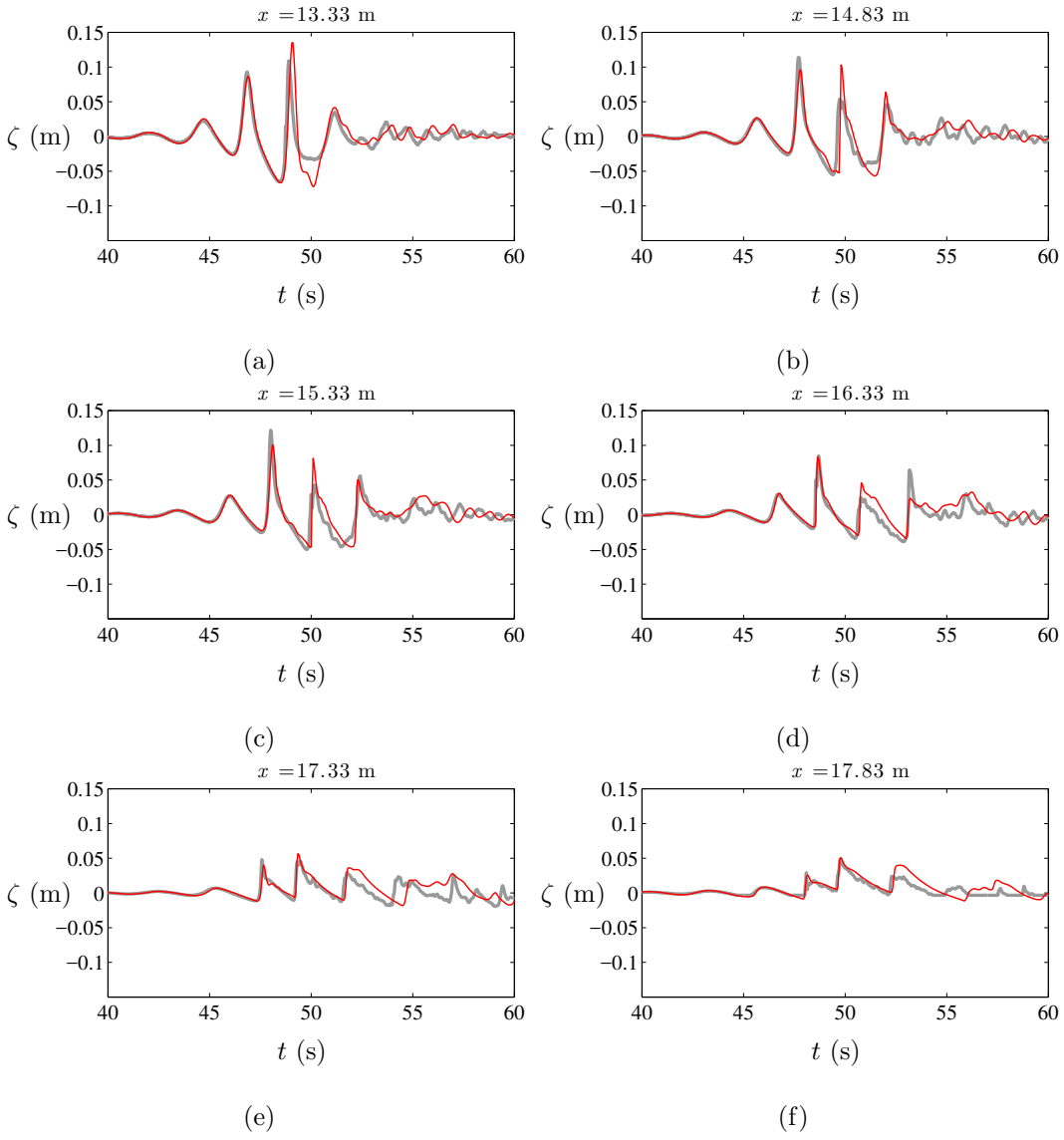

Figure 6.11: WG21 - Trough focused multi-directional wave group (±30°spread) in the UKCRF: comparison between shallow water gauge measured (thick grey line) and numerically predicted (red line) free-surface elevation time series at six gauge locations from $x = 13.33$ to $x = 17.83$ m.

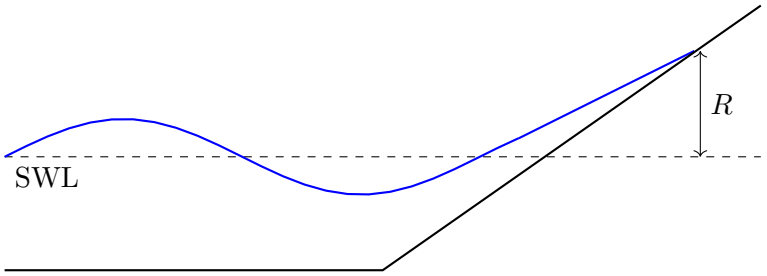

Figure 6.12: Definition of wave run-up

calculation of run-up caused by extreme waves is essential for the safe siting of new developments at the coast, or to assess flood risk posed to existing development. In the UKCRF tests described above, run-up was measured visually by filming the swash zone. Hunt (2003) estimates the error in these measurements to be ±10 cm along the slope, which corresponds to a vertical measurement of ±5 mm for a 1:20 beach.

The numerical model is now used to simulate several of the UKCRF wave group experiments used to estimate the maximum run-up. The wave groups chosen are those with the largest linear focus amplitude (A_f) for each focus location, namely the beach toe, $\frac{3}{4}$ depth, and $\frac{1}{2}$ depth. Multiple spread angles are considered. Table 6.3 summarises the measured and predicted run-up results for each of the wave groups. As expected, the largest run-up events are produced by the uni-directional wave groups, the largest of all being WG2, the trough focused wave group focusing at $\frac{3}{4}$ depth. In all cases, both numerical and experimental, the trough-focused wave groups produce larger run-up than their crest-focused counterparts. As the spread angle of the incident wave group increases, the maximum run-up decreases. For a given spread angle, with a linear focus amplitude $A_f = 114$ mm, the maximum run-up is generally very similar when the focus location is the beach toe or $\frac{3}{4}$ depth. The only major departure from this is for uni-directional wave groups WG1 and WG2, where the $\frac{3}{4}$ depth focus location produces a significantly larger run-up event in both the laboratory test and numerical simulation.

In general, there is good agreement between the UKCRF measurements and the numerically predicted values. The largest magnitude error is for wave group WG17 at 16.9%, followed by WG30 at -15%. A closer examination of Table 6.3 reveals that the numerical model tends to over-predict the run-up of crest-focused wave groups,

whereas the trough-focused wave group run-up is generally under-predicted. Table 6.4 calculates the percentage bias of the run-up results. The percentage bias measures the average tendency of the predicted values to be larger or smaller that the corresponding observations. It is given by

$$\%\,\mathrm{BIAS} = 100\left(\frac{\sum(R_m - R_p)}{\sum R_m}\right), \tag{6.13}$$

where R_m is the measured run-up, and R_p is the predicted run-up from Table 6.3. Whereas the total percentage bias of all wave groups is 1.2%, individual calculations for both crest- and trough-focused wave groups reveal +8.2% bias for the crest-focused groups, and -4.2% bias for the trough-focused groups.

Table 6.5 shows the run-up for the directionally spread wave groups predicted by the numerical model, expressed as a percentage of the run-up of the corresponding uni-directional wave group with the same linear focus amplitude and focus location. Grouping the main wave group types together (by spread angle and phase), and calculating the average percentage leads to Table 6.6, which presents a comparison with Table 6.4 of Hunt (2003). Hunt reports an approximate 20% reduction in run-up for a $\pm 10°$spread sea, and a 40% reduction for a $\pm 30°$spread sea. The reductions in run-up predicted by the numerical model for the $\pm 30°$spread crest and trough-focused seas, and the $\pm 10°$spread crest-focused seas are in general agreement with Hunt's figures. However, the large under-prediction by the numerical model of the run-up of wave groups WG29 and WG30 leads to a significant discrepancy in this metric for the $\pm 10°$spread trough-focused seas.

The values of the tuning parameters used in model calibration are likely to play a part in controlling the accuracy of the results obtained using the present model, particularly the value of C_f in the swash zone; this warrants further research. A higher resolution computational grid may also lead to improved results, however achieving this for the spread-sea case would require more computational power than was available for the present research study.

Wave group ref.	A_f (mm)	Spread angle	Phase (rad)	Focus location	Measured R (mm)	Predicted R (mm)	% error
WG1	114	0°	0	beach toe	98	109	11.2
WG2	114	0°	0	$\frac{3}{4}$ depth	110	117	6.4
WG3	90	0°	0	$\frac{1}{2}$ depth	90	97	7.8
WG5	114	0°	π	beach toe	135	138	2.2
WG6	114	0°	π	$\frac{3}{4}$ depth	136	137	0.7
WG7	90	0°	π	$\frac{1}{2}$ depth	115	113	-1.7
WG17	114	±30°	0	beach toe	59	69	16.9
WG18	114	±30°	0	$\frac{3}{4}$ depth	60	65	8.3
WG19	90	±30°	0	$\frac{1}{2}$ depth	51	56	9.8
WG21	114	±30°	π	beach toe	76	72	-5.3
WG22	114	±30°	π	$\frac{3}{4}$ depth	75	74	-1.3
WG23	90	±30°	π	$\frac{1}{2}$ depth	65	63	-3.1
WG25	114	±10°	0	beach toe	79	84	6.3
WG26	114	±10°	0	$\frac{3}{4}$ depth	85	86	1.2
WG27	90	±10°	0	$\frac{1}{2}$ depth	70	76	8.6
WG29	114	±10°	π	beach toe	106	91	-14.2
WG30	114	±10°	π	$\frac{3}{4}$ depth	107	91	-15.0
WG31	90	±10°	π	$\frac{1}{2}$ depth	86	84	-2.3

Table 6.3: Measured and predicted run-up of focused wave groups at a plane beach in the UKCRF.

Wave groups	% BIAS
All	1.2
Crest-focused	8.2
Trough-focused	-4.2

Table 6.4: % bias of run-up results

WG	Spread	Phase	% of uni-directional R_p	Ref. WG
WG17	±30°	0	63.3	WG1
WG18	±30°	0	55.6	WG2
WG19	±30°	0	57.7	WG3
WG21	±30°	π	52.2	WG5
WG22	±30°	π	54.0	WG6
WG23	±30°	π	55.8	WG7
WG25	±10°	0	77.1	WG1
WG26	±10°	0	73.5	WG2
WG27	±10°	0	78.4	WG3
WG29	±10°	π	65.9	WG5
WG30	±10°	π	66.4	WG6
WG31	±10°	π	74.3	WG7

Table 6.5: Run-up of directionally spread wave groups expressed as a percentage of the run-up of the corresponding uni-directional wave groups with the same linear focus amplitude and focus location (Ref. WG) at a plane beach in the UKCRF.

	mean % predicted	mean % measured (Hunt (2003))
±10°crest focus	76.3	80.2
±10°trough focus	68.9	78.3
±30°crest focus	58.9	59.8
±30°trough focus	54.0	56.3

Table 6.6: Ratio of spread sea run-up to uni-directional run-up: predicted versus measured

6.3 Multi-directional focused wave group harmonic structure

Following the method summarised in section 4.2.1, Hunt (2003) analysed the harmonic structure of focused wave groups, by isolating individual harmonics through judicious combination of the surface elevation data on crest- and trough-focused wave groups from the UKCRF experiments. Orszaghova (2011) performed a similar exercise using data from the one-dimensional numerical model. The purpose of the exercise is to find evidence of bound and parasitic waves that may contaminate the results, in particular those for wave run-up. Waves were generated in the UKCRF experiments by supplying paddle signals derived from linear wave theory, outlined in section 2.5. However, paddle generated waves, except for very small amplitudes, will always contain nonlinearities. Mismatch between the nonlinear paddle generated waves and the desired linear waves results in extra components that create free parasitic or error waves, that are not bound to the wave group. The largest parasitic waves are those associated with the second-order bound Stokes terms. Such waves have the same high and low frequencies, but different wave numbers. Table 6.7 shows the bound second-order terms for Hunt's deep water example of the combination of two regular wave trains described in Section 4.2.1, and the associated parasitic free waves. The primes indicate the wave numbers of the free parasitic waves and can be obtained using linear dispersion. These waves cancel out at the paddle, but nowhere else in the basin.

The first three parasitic waves are high-frequency waves, and thus travel slower than the main wave group. However the fourth is a low-frequency wave that travels ahead of the main wave group, and thus has an impact on the transformation of the wave group. The associated low-frequency bound wave is called the set-down term as it represents a lowering of the water surface underneath the wave group. The corresponding parasitic wave is of opposite sign and therefore manifests itself as a hump of water that travels ahead of the wave group. As the addition time-series contains the even harmonics, it will contain all of the four parasitic terms listed in Table 6.7. The subtraction time-series contains the odd harmonics, and thus the largest parasitic waves in this series

Bound waves	Parasitic free waves
$+\frac{1}{2}a_1^2 k_1 \cos 2(k_1 x - \omega_1 t)$	$-\frac{1}{2}a_1^2 k_1 \cos 2(k_1' x - \omega_1 t)$
$+\frac{1}{2}a_2^2 k_2 \cos 2(k_2 x - \omega_2 t)$	$-\frac{1}{2}a_2^2 k_2 \cos 2(k_2' x - \omega_2 t)$
$+\frac{1}{2}a_1 a_2 (k_1 + k_2) \cos((k_1 + k_2)x - (\omega_1 + \omega_2)t)$	$-\frac{1}{2}a_1 a_2 (k_1 + k_2) \cos(k_{12}' x - (\omega_1 + \omega_2)t)$
$-\frac{1}{2}a_1 a_2 (k_1 - k_2) \cos((k_1 - k_2)x - (\omega_1 - \omega_2)t)$	$+\frac{1}{2}a_1 a_2 (k_1 - k_2) \cos(k_{12}'' x - (\omega_1 - \omega_2)t)$

Table 6.7: Pairs of second-order bound and parasitic free waves arising from linear paddle signals Hunt (2003)

will be third-order. It should be noted that generating waves with a piston-paddle wavemaker is further complicated by the presence of evanescent waves (described in section 2.5). However, as these decay away from the paddle, evanescent waves are not considered further here.

Hunt (2003) and Orszaghova (2011) analysed the harmonic structure of wave groups travelling normal to the beach. In the present thesis, a similar exercise is performed, but for multi-directional wave groups, namely wave groups WG17 and WG21 which are crest- and trough-focused wave groups respectively, with a spread angle of $\pm 30°$. Applying a fast-Fourier-transform (FFT) to the surface elevation data from the numerical model for WG17 and WG21 at the beach toe, leads to the amplitude spectra shown in Figure 6.13. Analysis of the amplitude spectra reveals that both the crest and trough-focused time series (sub-figures (a) and (b)) have a concentration of energy at 0.46 Hz, at the peak frequency of the linear components. Secondary peaks are visible at approximately half and double this peak frequency. Figures 6.13 (c) and (d) present the addition and subtraction time series respectively at the beach toe, and can be used to identify suitable cut-off frequencies to isolate bound and parasitic higher order waves. The amplitude spectrum of the addition time series which contains even-order harmonics, reduces to zero at 0.5 Hz, which suggests that this would be a suitable cut-off point to isolate low and high frequency second-order harmonics. For the subtraction time series, a cut-off frequency of 1 Hz is used to separate the linear, first-order terms from the higher-order harmonics.

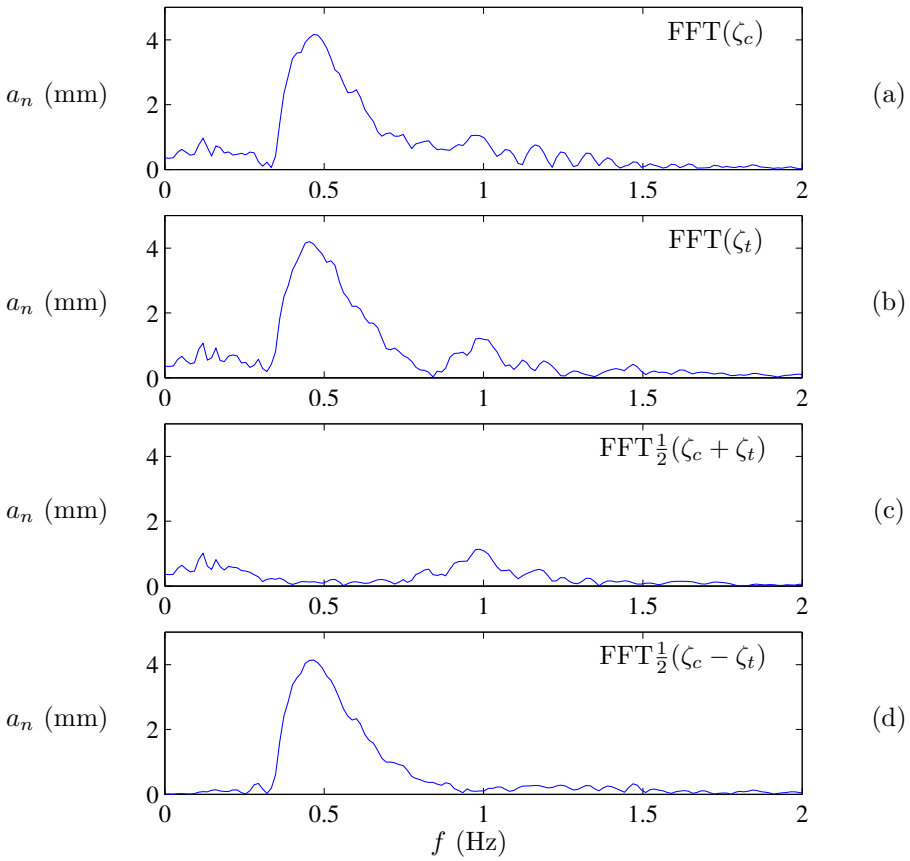

Figure 6.13: Amplitude spectra at the beach toe for (a) crest-focused wave group time series (WG17); (b) trough-focused wave group time series (WG21); (c) addition time series and (d) subtraction time-series

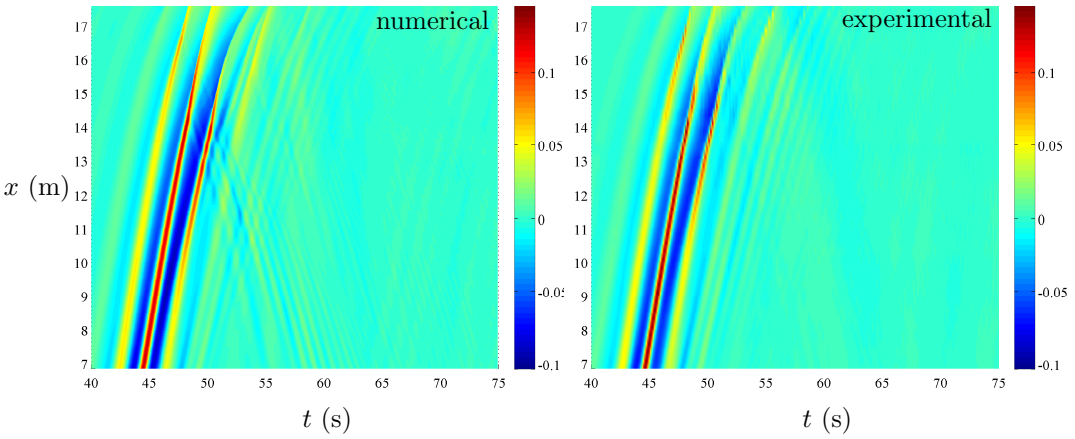

(a) (b)

Figure 6.14: Space-time plots of NewWave propagation at a plane beach for a crest-focused wave group (WG17): (a) numerical prediction; and (b) measured free-surface elevation data, along basin centreline

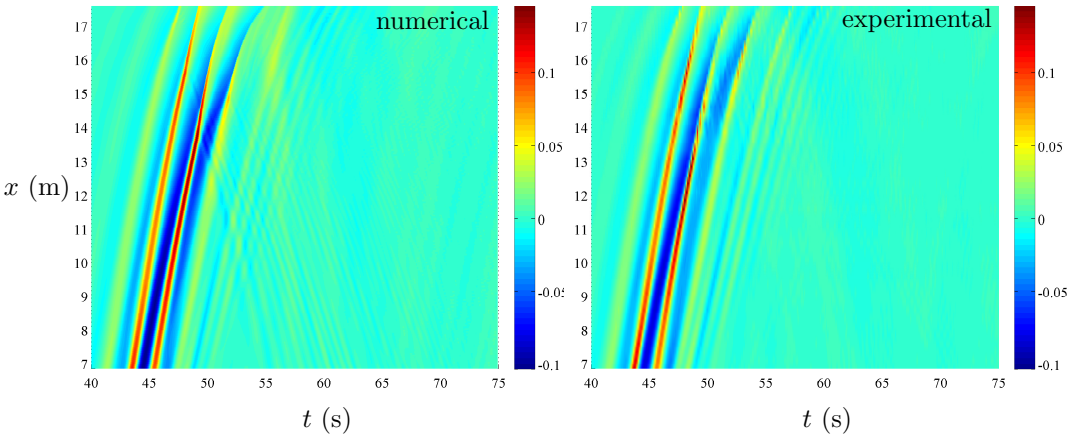

(a) (b)

Figure 6.15: Space-time plots of NewWave propagation at a plane beach for a trough-focused wave group (WG21): (a) numerical prediction; and (b) measured free-surface elevation data, along basin centreline

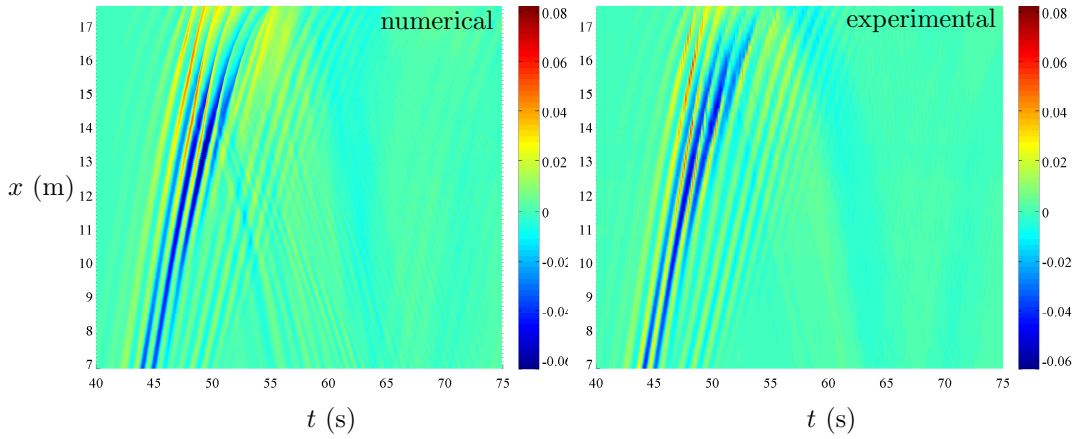

Figure 6.16: Space-time plots of addition free-surface elevation time series (WG17 and WG21) for NewWave propagation at a plane beach in the UKCRF: (a) numerical prediction, and (b) measured data, along basin centreline

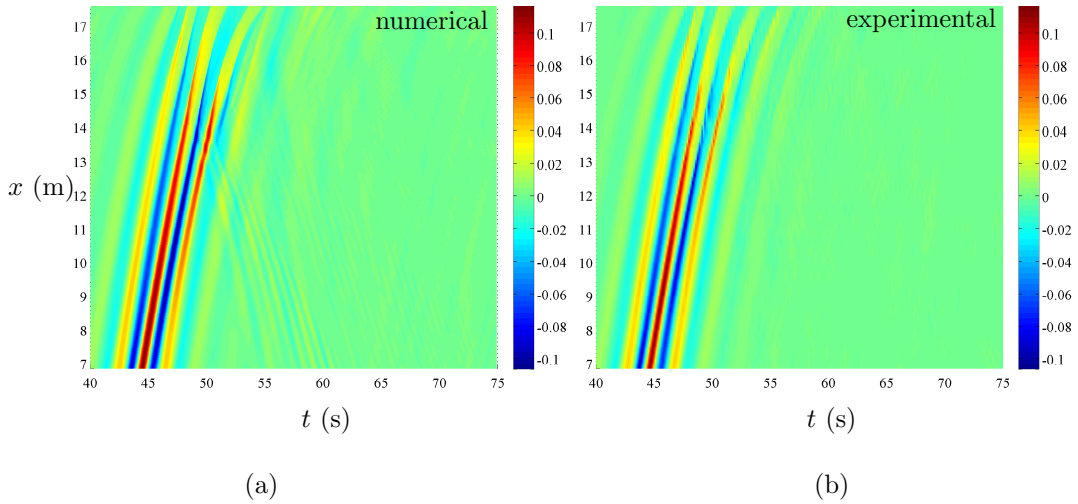

Figure 6.17: Space-time plots of subtraction free-surface elevation time series (WG17 and WG21) for NewWave propagation at a plane beach in the UKCRF: (a) numerical prediction, and (b) measured data, along basin centreline

Figures 6.14 and 6.15 present $x-t$ visualisations of the propagation of the crest- and trough-focused wave groups WG17 and WG21 along the centreline of the basin. Both the numerical model output and the experimental gauge data are shown. Presentation of the data in this way allows an overall comparison to be made between the numerical results and the gauge data, as well as revealing features such as wave reflections, which are not obvious in the individual gauge comparisons shown in Figures 6.8 to 6.11. In Figure 6.14, the central crest (shown in red) of WG17 and the troughs on either side (shown in blue) are clearly visible. The wave group focuses at $x \approx 8.33$ m, when the crests on either side of the main crest (shown in yellow/orange) are approximately the same size. Dispersion is evident as the wave group propagates up the beach and becomes less well defined. Breaking can be identified by a sharp drop in amplitude, for example at $x \approx 16$ m for the central crest, and at $x \approx 15$ m for the trailing crest. In both the numerical and experimental results, there is evidence of long-wave reflections. However the numerical plot also shows some high-frequency reflections from $x \approx 12$ m. These are also present in the one-dimensional numerical results of Orszaghova (2011) who attributes the presence of such reflections to the switch between governing equation sets. The $x-t$ plots of the trough-focused wave group WG21 in Figure 6.15 exhibit similar features. Again there is some evidence of low frequency reflections in both the numerical and experimental results.

Figure 6.16 presents an $x-t$ visualisation of the addition time series for wave groups WG17 and WG21. Following the theory outlined above, the addition time-series should show only the even harmonics. High frequency even harmonics are immediately obvious, while long wave reflections provide evidence of low frequency harmonics. The subtraction time series shown in Figure 6.17 contain the odd harmonics: the linear components of the wave group, and high frequency noise.

Individual low and high frequency, odd and even harmonics are investigated further by applying the cut-off frequencies identified above using Figure 6.13. Figure 6.18 shows the linear components of wave groups WG17 and WG21, which are obtained by applying a low-pass filter at 1 Hz to the subtraction time series. As in Figure 6.17, the odd harmonics are present, but with the high frequency noise removed, leaving only the

linear components. Steep-fronted waves that characterise the unfiltered time series are not present here. Unmodified by the higher-order components, the wave crests remain centrally positioned as the waves propagate into shallower water. The experimental $x - t$ plot shows no reflections, i.e. all the linear components are absorbed by the beach, whereas the numerical plot shows some reflections from $x \approx 12$ m. A high-pass filter at 1 Hz is applied to the subtraction series in Figure 6.19, revealing the third-order harmonics. Again, reflections are evident from $x \approx 12.5$ m in the numerical results, unlike the experimental data. These reflections are primarily due to implementation of the transition zone to the shallow water equations at wave breaking.

Figure 6.20 shows the addition time series, low-pass filtered at 0.5 Hz to reveal the low frequency second-order harmonics. The blue depression in these plots represents the bound second-order wave travelling beneath the main wave group, or the 'set-down'. The orange hump is the low frequency parasitic or error wave generated as a result of the first-order paddle signal. This is a free wave, travelling independently of the main wave group. The darker blue bound wave in Figure 6.20 (a) indicates that the numerical model predicts a larger set-down beneath the main wave group than was observed in the laboratory. The numerical results also indicate a larger low-frequency error wave, which increases in amplitude with respect to the experimental data as the wave group approaches the shore. The picture becomes more complicated once the waves break. It is unclear whether the reflected waves, in both the numerical and experimental results, are due to the error wave, the bound wave, or some combination of the two. What is clear however is that the initial long wave reflection is more severe in the numerical simulation. This reflection, coupled with the larger incoming error wave, may be the reason for the 16.9 % error in the run-up calculation of WG17. Figure 6.21 presents a visualisation of the high frequency second-order harmonics, obtained by applying a high-pass filter at 0.5 Hz to the addition time series. These double-frequency harmonics include both bound and parasitic components. Again there are reflections evident from $x \approx 13$ m in the numerical results, whereas the experimental data show full absorption of these components by the beach.

The above analysis of the harmonic structure of the multi-directional focused wave

groups provides similar results to those obtained by Hunt (2003) and Orszaghova (2011) for uni-directional wave groups, in particular the presence of a low frequency error wave travelling ahead of the main wave group. However, the magnitude of this wave for a spread sea is smaller than for the corresponding uni-directional case, echoing the experimental findings of Hunt (2003), so the impact is not likely to be as severe. Orszaghova (2011) presents a detailed investigation into the impact the error wave has on the calculation of run-up and overtopping for the uni-directional case, by applying a second-order correction to the paddle, which effectively eliminates the error wave. Orszaghova found that by implementing second-order wave generation, predicted values of run-up are on average 40% smaller, than when first-order paddles signals are used. This has implications for the design of coastal protection, as structures may be significantly over-engineered if the calculations are based on first-order paddle theory. It is recommended that future research effort is directed toward carrying out a similar exercise on the paddle signals for the spread sea case; by analysing the resulting harmonic structure of the generated wave groups, useful insight would be provided into the influence of the low frequency error wave on the interaction of multi-directional wave groups with the shore.

6.4 Chapter summary

- This chapter has presented the results of numerical simulations of focused wave groups propagating up a plane beach at laboratory scale. Numerical predictions of both uni-directional and multi-directional focused wave groups are compared with experimental data from the UKCRF.

- Both sets of numerically predicted free-surface profiles compare very well with the corresponding experimental measurements. The leading waves of the wave groups are predicted to a high level of accuracy across all wave gauge locations. The numerical model generally under-predicts the height of the main crest in the wave groups, while predicting larger trough depths either side of the main crest than the laboratory measurements. The wave breaking location and the

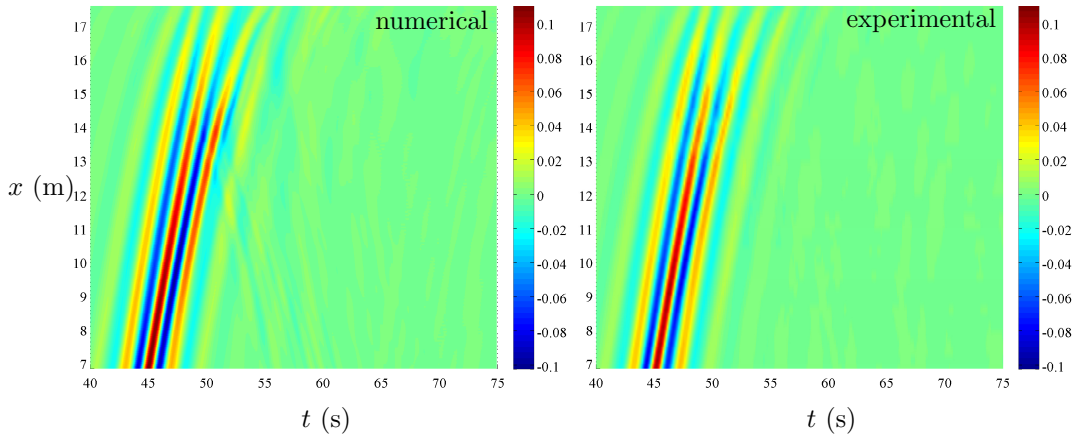

(a) (b)

Figure 6.18: Space-time plots of NewWave run-up at a plane beach - Linear terms only, subtraction time series low-pass filtered at 1 Hz (WG17 and WG21): (a) numerical prediction, and (b) experimental gauge data, along basin centreline

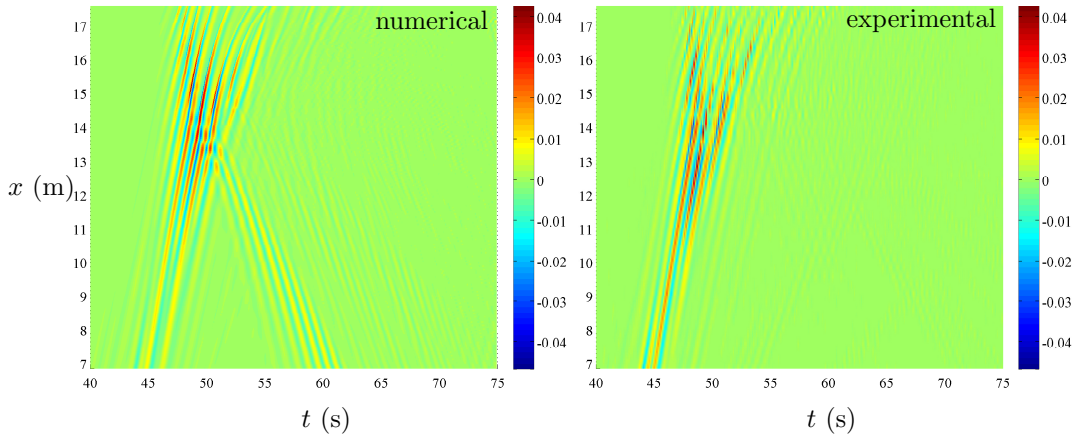

(a) (b)

Figure 6.19: Space-time plots of NewWave run-up at a plane beach - Odd higher order harmonics only, subtraction time series high-pass filtered at 1 Hz (WG17 and WG21): (a) numerical prediction, and (b) experimental gauge data, along basin centreline

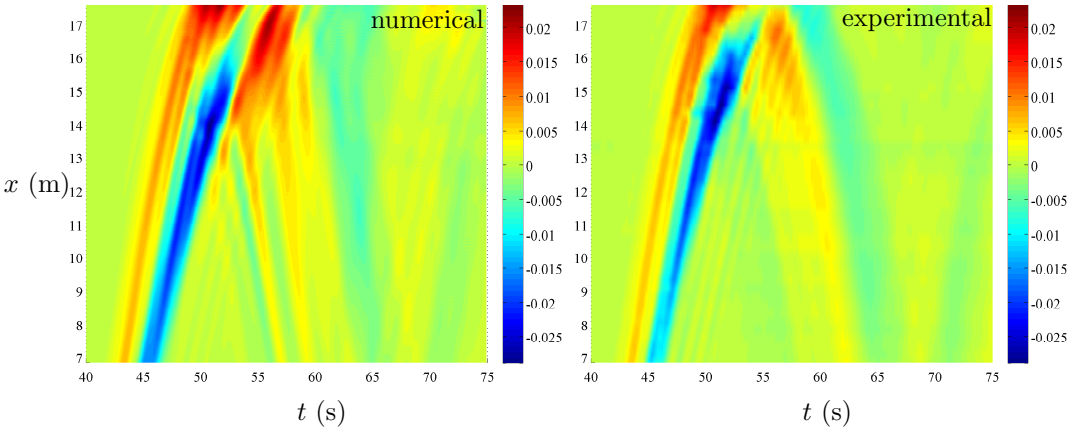

(a) (b)

Figure 6.20: Space-time plots of NewWave run-up at a plane beach - Even, low frequency components only (i.e. long waves), addition time series low-pass filtered at 0.5 Hz (WG17 and WG21): (a) numerical prediction, and (b) experimental gauge data, along basin centreline

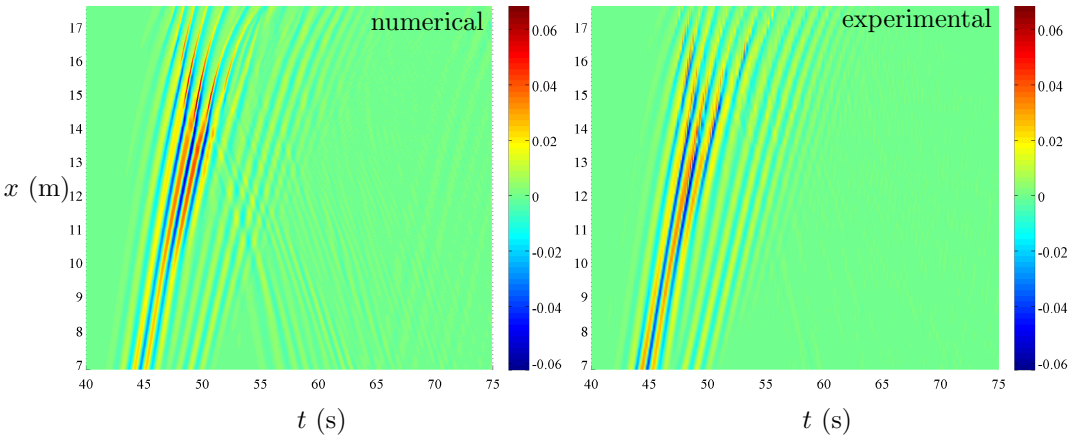

(a) (b)

Figure 6.21: Space-time plots of NewWave run-up at a plane beach - Even, high frequency components only, addition time series high-pass filtered at 0.5 Hz (WG17 and WG21): (a) numerical prediction, and (b) experimental gauge data, along basin centreline

propagation of bores is predicted to reasonable accuracy, with a slight lag in phase speed evident between the predicted and observed data in the surf zone.

- Numerical predictions of run-up are generated for a wide range of wave groups, with varying focus locations, phase and spread angles. The numerical results are in general agreement with the UKCRF experimental data. The numerical model tends to over-predict the run-up of crest-focused wave groups, and under-predict the run-up due to trough-focused wave groups.

- Judicious addition and subtraction of the ±30°crest- and trough-focused wave groups (WG17 and WG21) has provided insight into the harmonic structure of these wave groups. Applying filters at appropriate frequencies reveals the presence of a low frequency error wave travelling ahead of the main wave group, as well as high frequency higher-order components trailing the wave group.

Chapter 7

Conclusions and recommendations

This chapter provides a summary of the work undertaken in this thesis. Recommendations for future research are also made.

7.1 Conclusions

This thesis has presented a two-horizontal-dimension (2DH) numerical flow solver for modelling the propagation of waves in the coastal zone, from intermediate to zero depth. Waves are generated in the model by numerical piston paddle wavemakers, capable of creating both long- and short-crested seas. The model is capable of simulating the transformation of unbroken waves to broken waves propagating as bores. It provides satisfactory estimates of run-up due to extreme wave events, as well as reproducing nearshore circulation patterns caused by the interaction of waves with non-planar bathymetry.

2DH model summary

Pre-breaking, the numerical model is based on the enhanced Boussinesq equation set derived by Madsen and Sørensen (1992). Broken waves propagate as bores and are represented in the hybrid model by the non-linear shallow water equations. Both equa-

tion sets are formulated in term of (η, $\mathbf{Q}$), where η represents the free-surface elevation above a prescribed horizontal datum, and $\mathbf{Q}$ is the vector of horizontal fluxes, (q_x, q_y). This formulation facilitates straightforward simulation of the moving wet/dry front. The switch between the governing equation sets is determined by the magnitude of the slope of the free surface. The switch is applied equally across the domain in the $y-$direction, with the shallow water equations solved at all points onshore of the switch point in the $x-$direction, and the Boussinesq equations solved offshore of the switch point. Dispersive terms in the Boussinesq equations are ramped down over half a wavelength approaching the switch point to ensure a smooth transition. The switch point is recalculated at every time-step, and thus tracks the breaking waves onshore.

The Boussinesq equations are discretised using second-order finite differences, and solved using the conjugate gradient method. The equations are integrated forward in time using fourth-order Runge-Kutta time-stepping. The deformation of the underlying grid due to the motion back and forth of the paddles is dealt with by applying a domain-mapping technique in the region adjacent to the paddles. This moving, physical domain is mapped onto a fixed computational grid to facilitate the solution of the Boussinesq equations in this zone. The mapping results in a transformed Boussinesq equation set, which is solved in the same way as the untransformed equations. The shallow water equations are solved using a finite volume MUSCL-Hancock scheme, with an HLLC approximate Riemann solver (capable of dealing with steep-fronted bores). The solver incorporates an in-built wetting and drying algorithm to model the moving wet/dry front. Waves are generated by feeding a time-series of displacements to each of the paddles in the numerical model.

Model verification

Different aspects of the numerical model have been verified using a series of benchmark tests. The evolution of sloshing waves, produced by an initial Gaussian hump in a closed, square basin is used to check the correct handling of the cross-derivative terms in the Boussinesq equations. Excellent agreement is obtained with the corresponding analytical solution of the long wave equation. A reversibility check on the evolution of

the Gaussian hump confirms the accuracy of the numerical methods implemented in the model, and demonstrates the model's conservation properties. A harmonic analysis of the sloshing waves provides insight into their harmonic structure, as well as providing a template for a similar exercise later applied to focused wave groups.

Simulation of sloshing in a parabolic basin and comparison of the numerical prediction with the analytical solution of Sampson et al. (2006) confirm the accuracy of the finite-volume solver and its ability to model the moving wet/dry front. Propagation of a dam break wave over a floodplain with three conical hills is simulated to provide a robust test of the wetting and drying algorithm. This test also demonstrates the model's ability to replicate complicated interactions between the waves, the topography, and the basin walls.

Correct implementation of the numerical piston-paddle wavemaker is tested by calculating the paddle signal for a solitary wave using a semi-analytical method derived by Orszaghova (2011), and confirming the generated wave matches the specified input amplitude.

Simulation of nearshore circulation

The numerical model has been used to predict nearshore circulation patterns resulting from the interaction of regular waves with non-planar beaches, obtained previously in the laboratory by da Silva Lima (1981) and Borthwick and Foote (2002). da Silva Lima's experiment involved regular waves interacting with a half-sinusoidal beach. The circulation pattern generated in the laboratory experiment is reasonably well reproduced by the numerical model, which predicts the main, clockwise-rotating primary gyre, and a weaker, anti-clockwise rotating, secondary gyre closer to the shore. Discrepancies between the numerical prediction and the laboratory measurements occur regarding the position of the gyres, with the numerical model predicting the main gyre to be centred further offshore than observed in the laboratory. This discrepancy can be attributed to a number of factors, including the uniform application of the switch point between equation sets across the basin. While the implementation of the switch point between the governing equation sets is reasonable with planar bathymetry, the asymmetric na-

ture of the half-sinusoidal beach causes the non-dispersive shallow water equations to be applied in a region where dispersion is still significant; this demonstrates the desirability of a more sophisticated criterion for the switch between equation sets. Other factors that are likely to affect the results include the calibration of the tunable parameters in the model, such as the bed friction coefficient C_f, and the surface elevation gradient limit, set to $\Theta \geq 0.4$.

The numerical simulation of the laboratory experiment of Borthwick and Foote (2002) involves regular waves interacting with a tri-cuspate beach located in the UK Coastal Research Facility. The model's ability to predict nearshore circulation patterns is again demonstrated, with the pairs of counter-rotating circulation cells and seaward directed rip-currents correctly positioned.

Simulation of focused wave groups

The numerical model has also been applied to the interaction of focused wave groups with a plane beach. Both uni-directional and multi-directional wave groups are considered, and the results compared to wave gauge data from the laboratory experiments of Hunt (2003) carried out in the UKCRF. The numerically predicted free-surface profiles of both the uni-directional and multi-directional wave groups compare very well with the corresponding experimental measurements. The leading wave groups are predicted with excellent accuracy across all wave gauge locations. The numerical model generally under-predicts the height of the main wave crest in the wave groups, and over-predicts the trough depths either side of the main crest compared with the laboratory measurements. The wave breaking location and the propagation of bores is predicted to reasonable accuracy, with a slight lag in phase speed evident between the predicted and observed data in the surf zone.

Run-up predictions have been generated with the numerical model for a wide range of wave groups, with varying focus locations, phase and spread angles. The numerical results are in general agreement with experimental data from the UKCRF tests. The model tends to over-predict the run-up of crest-focused wave groups, whereas the run-up due to trough-focused wave groups is generally under-predicted.

The harmonic structure of multi-directional wave groups is analysed through judicious addition and subtraction of crest-focused and trough-focused time series. Focused wave groups with a spread angle of $\pm 30°$, linear focus amplitude $A_f = 114$ mm, and focused at the beach toe are used for this exercise. Application of filters at appropriate frequencies reveals the presence of a low frequency error wave travelling ahead of the main wave group, as well as high frequency higher-order components trailing the wave group. This is a similar finding to that obtained by Hunt (2003) and Orszaghova (2011) for uni-directional wave groups. However, the magnitude of the long error wave for a spread sea is smaller than for the corresponding uni-directional case, so its impact on run-up is not likely to be as severe.

7.2 Recommendations for future work

Second-order wave generation

Orszaghova (2011) presents a detailed investigation into the impact the long error wave generated by a first-order paddle signal has on wave run-up and overtopping. Orszaghova found that by applying a second order correction to the paddle signal, the error wave is effectively eliminated and run-up values are on average 40% smaller than when first-order paddle signals are used. Applying second-order correction to the paddles in the present numerical model, and repeating the analysis of the harmonic structure of the multi-directional focused wave groups would provide useful insight into the impact of the low-frequency error wave on the run-up and overtopping due to a spread sea.

Activation of the breaking criterion

The predictions of nearshore circulation presented in Chapter 5 indicate a more sophisticated two-dimensional breaking criterion would be of benefit in domains with an asymmetric and/or variable bathymetry. This would also be important for modelling waves approaching the shore at steeper angles than the maximum of 30° simulated in this research, and may indeed improve the accuracy of the multi-directional cases

considered herein.

Turbulence modelling

The results in Chapter 5 also suggest that increased accuracy may be achieved through the implementation of a more sophisticated turbulence model. Such a model may include alternative methods of calculating the eddy viscosity ε. The evaluation of different turbulence models could perhaps be achieved by validation against laboratory tests where measurements are made of water surface elevation profiles, nearshore currents and circulation patterns. In this way, the numerical prediction of the effect wave-current interaction has on both the free-surface profile and circulation patterns can be evaluated with greater confidence. Comparison with the predictions of other numerical models, such as the fully nonlinear model of Chen et al. (2003), may also prove insightful.

Two-dimensional domain mapping

The mapping technique implemented in the present model is essentially one dimensional, but has proven adequate for the generation of short-crested seas with a spread angle of up to $\pm 30°$. As this angle of spread represents the approximate limit for wave basins with paddles along one wall only, the present numerical model is an acceptable tool for modelling these facilities. In order to model a wave basin capable of generating waves at a steeper angle, for example where paddles are located on two adjacent walls, such as the shallow water basin at the Lir National Ocean Testing Facility in Cork, an adaption of the present mapping technique would be required.

Sponge layers

Absorption of reflected waves at the wavemaker is essential when carrying out long duration experiments or simulations in either a laboratory or a numerical wave basin. Inclusion of numerical absorption within the present model would be very desirable, as it would extend its capabilities to wave basins that incorporate active absorption at the paddles, as well as simulations involving unbounded domains. Fitzgerald et al.

(2016) successfully implements a generating-absorbing sponge layer in the 1DH model of Orszaghova (2011). A 2DH implementation would necessitate an absorbing sponge layer along the lateral boundaries, as well as a generating-absorbing layer front of the paddles.

Improved efficiency

Although computationally efficient compared to CFD tools, use of the model developed in this research as a tool for the prediction of wave propagation is still hampered by lengthy simulation run-times for certain cases, i.e. for spread sea simulation or where the physical domain under consideration is large. While partial parallelisation of the code was carried out, i.e. in the implementation of the conjugate gradient algorithm, further improvements could be made to the model performance by applying PETSc routines, or similar, to the code at large. A fully parallelised code would mean the model could be run with high efficiency across a number of cores on a high performance computer. Other devices have appeared in recent years, most notably graphics processing units (GPUs) and field programmable gate arrays (FGPAs) which offer a low-energy, cheap and viable approach to accelerating simulations. In terms of the laboratory test cases considered in this research, improved computational speeds would facilitate numerous runs enabling better calibration, more extensive parameter studies, and higher resolution computations.

Investigation of a second-order time integration technique for the Boussinesq equations may be worthwhile in order to increase computational efficiency. Shiach and Mingham (2009) present a hybrid finite volume/finite difference scheme that uses a second-order time marching method to solve the one-dimensional extended Boussinesq formulations of both Madsen and Sørensen (1992) and Nwogu (1993). They found that the results for the second-order time marching method, were indistinguishable from a fourth-order Adams-Moulton method, but 2-3 times faster.

Improved robustness

Implementation of a finite volume rather than finite difference approach to solving the Boussinesq equations is also worth considering. The finite volume scheme used in this research to solve the shallow water equations could be extended to include the Boussinesq portion of the model. As the shock-capturing abilities of finite volume solvers mean they can naturally deal with any sharp fronted flows (such as the steep waves reflected by a sea wall reported by Orszaghova (2011)), they are very robust compared to their finite-difference counterparts. Such a scheme may also facilitate the more sophisticated two-dimensional breaking criterion discussed above.

Dedicated wave basin model

The model developed in this research has proven capable of simulating wave basin experiments. With some further validation and calibration, the model could be tuned to become an excellent numerical representation of an individual wave basin or flume. Having a numerical model of laboratory facilities is an extremely useful asset for a research institution, because proposed physical experiments can first be modelled numerically to help guide the programme of laboratory tests. A variety of bathymetry profiles or sea wall configurations for example, can be easily implemented in the numerical model and numerous test runs carried out, before physical construction takes place. The positioning of wave gauges and other instrumentation can also be optimised with a numerical model as a guide. Time and personnel constraints associated with laboratory testing do not apply to a numerical model, and so such a model could also be used to carry out additional simulations that cannot be accommodated within the experimental programme.

Tsunami modelling

Due to their extremely long wavelengths, tsunamis can be considered shallow water waves even in the open ocean, and can thus be modelled by depth-integrated equations. While modelling tsunamis in the nearshore region is possible in the laboratory, the limited length of most facilities means the propagation of such waves from the open

ocean can only be modelled numerically. The present model would provide the means of modelling tsunamis with different angles of approach.

Coastal morphology

The numerical model could be coupled with depth-integrated sediment transport and bed morphology models to capture the evolution of the sea bed. While coastal morphology generally takes place over very long timescales, making Boussinesq-type models unsuitable for this type of sediment transport problem, they can be used to model the morphological changes caused by shorter time scale events such as storms and tsunamis. Kim (2015) obtains good results using a fully nonlinear Boussinesq model for morphological evolution due to a storm, a tsunami and a dam break wave.

Nested 3D model

In the present hybrid model, the shallow water equations predict the propagation of broken waves with good accuracy over slowly varying bathymetry. However, the underlying assumptions of predominantly horizontal flow and hydrostatic pressure are violated when waves interact with steeply sloped or vertical structures. In such instances, depth-resolving models are necessary to model the physics with good accuracy. Application of 3D models over a large physical domain carries a high computational cost and can be susceptible to numerical dissipation when waves are propagating over long distances. An alternative approach would be to nest SPH or another 3D solver within the present numerical model. This would facilitate the detailed modelling of waves interacting with more complex coastal structures, for example a recurved sea wall, as well as accurately resolving near-shore flow features. Pringle et al. (2016) obtain promising results for a 1DH solver that couples the non-linear shallow water equations with a RANS model.

Appendices

Appendix A

Transformed derivative operators

$$\frac{\partial^2}{\partial x^2} = \frac{4}{b_i^2}\frac{\partial^2}{\partial \tilde{x}^2} \tag{A.1a}$$

$$\frac{\partial^2}{\partial y^2} = \frac{\partial^2}{\partial \tilde{y}^2} \tag{A.1b}$$

$$\frac{\partial^3}{\partial x^3} = \frac{8}{b_i^3}\frac{\partial^3}{\partial \tilde{x}^3} \tag{A.1c}$$

$$\frac{\partial^3}{\partial y^3} = \frac{\partial^3}{\partial \tilde{y}^3} \tag{A.1d}$$

$$\frac{\partial^2}{\partial x \partial y} = \frac{2}{b_i}\frac{\partial^2}{\partial \tilde{x} \partial y} \tag{A.1e}$$

$$\frac{\partial^3}{\partial x \partial y^2} = \frac{2}{b_i}\frac{\partial^3}{\partial \tilde{x} \partial y^2} \tag{A.1f}$$

$$\frac{\partial^3}{\partial x^2 \partial y} = \frac{4}{b_i^2}\frac{\partial^3}{\partial \tilde{x}^2 \partial y} \tag{A.1g}$$

$$\frac{\partial^2}{\partial x \partial t} = \frac{2}{b_i}\frac{\partial^2}{\partial \tilde{x} \partial \tilde{t}} + \frac{2}{b_i^2}\frac{\partial b_i}{\partial \tilde{t}}\left((1-\tilde{x})\frac{\partial^2}{\partial \tilde{x}^2} - \frac{\partial}{\partial \tilde{x}}\right) \tag{A.1h}$$

$$\frac{\partial^2}{\partial y \partial t} = \frac{\partial^2}{\partial y \partial \tilde{t}} + \frac{1}{b_i}\frac{\partial b_i}{\partial \tilde{t}}(1-\tilde{x})\frac{\partial^2}{\partial \tilde{x} \partial y} \tag{A.1i}$$

$$\frac{\partial^3}{\partial x^2 \partial t} = \frac{4}{b_i^2}\frac{\partial^3}{\partial \tilde{x}^2 \partial \tilde{t}} + \frac{4}{b_i^3}\frac{\partial b_i}{\partial \tilde{t}}\left((1-\tilde{x})\frac{\partial^3}{\partial \tilde{x}^3} - 2\frac{\partial^2}{\partial \tilde{x}^2}\right) \tag{A.1j}$$

$$\frac{\partial^3}{\partial y^2 \partial t} = \frac{\partial^3}{\partial y^2 \partial \tilde{t}} + \frac{1}{b_i}\frac{\partial b_i}{\partial \tilde{t}}(1-\tilde{x})\frac{\partial^3}{\partial \tilde{x}\partial y^2} \tag{A.1k}$$

$$\frac{\partial^3}{\partial x \partial y \partial t} = \frac{2}{b_i}\frac{\partial^3}{\partial \tilde{x}\partial y \partial \tilde{t}} + \frac{2}{b_i^2}\frac{\partial b_i}{\partial \tilde{t}}\left((1-\tilde{x})\frac{\partial^3}{\partial \tilde{x}^2 \partial y} - \frac{\partial^2}{\partial \tilde{x}\partial y}\right) \tag{A.1l}$$

Appendix B

Finite difference approximations

B.1 Higher-order mixed derivative stencils

$$f_{xxy}(p_{i,j}) = \frac{1}{2\Delta x^2 \Delta y}\left(f_{i+1,j+1} - 2f_{i+1,j} + f_{i+1,j-1} - f_{i-1,j+1} + 2f_{i-1,j} - f_{i-1,j-1}\right) + O(\Delta x^2, \Delta y^2) \tag{B.1a}$$

$$f_{xyy}(p_{i,j}) = \frac{1}{2\Delta x \Delta y^2}\left(f_{i+1,j+1} - 2f_{i,j+1} + f_{i-1,j+1} - f_{i+1,j-1} + 2f_{i,j-1} - f_{i-1,j-1}\right) + O(\Delta x^2, \Delta y^2) \tag{B.1b}$$

B.2 Higher-order and mixed derivative non-uniform stencils

The following non-uniform stencils are derived using the formulas presented by Bowen and Smith (2005).

$$\begin{aligned} f_{\tilde{x}\tilde{x}\tilde{x}}(p_{i,j=\tilde{B}-1}) = &- \frac{1}{\Delta\tilde{x}^3}\left(\frac{b_i + b0}{3b_i + b0}\right) f_{i,\tilde{B}-3} \\ &+ \frac{1}{\Delta\tilde{x}^3}\left(\frac{3b0}{2b_i + b0}\right) f_{i,\tilde{B}-2} \\ &+ \frac{3}{\Delta\tilde{x}^3}\left(\frac{b_i - b0}{b_i + b0}\right) f_{i,\tilde{B}-1} \\ &- \frac{1}{\Delta\tilde{x}^3}\left(\frac{2b_i - b0}{b0}\right) f_{i,\tilde{B}} \end{aligned} \tag{B.2a}$$

$$+\frac{1}{\Delta\tilde{x}^3}\left(\frac{12b_i^4}{b0(b_i+b0)(2b_i+b0)(3b_i+b0)}\right)f_{i,\tilde{B}+1}$$

$$\begin{aligned}f_{\tilde{x}\tilde{x}\tilde{x}}(p_{i,j=\tilde{B}}) =& \frac{3b_i}{\Delta\tilde{x}^3}\left(\frac{b_i-3b0}{2(2b_i+b0)(b_i+b0)}\right)f_{i,\tilde{B}-2}\\ &-\frac{6b_i}{\Delta\tilde{x}^3}\left(\frac{2b_i-3b0}{(b_i+b0)(b_i+2b0)}\right)f_{i,\tilde{B}-1}\\ &+\frac{9b_i}{\Delta\tilde{x}^3}\left(\frac{b_i-b0}{2b0^2}\right)f_{i,\tilde{B}}\\ &-\frac{6b_i^3}{\Delta\tilde{x}^3}\left(\frac{3b_i-2b0}{b0^2(2b_i+b0)(b_i+b0)}\right)f_{i,\tilde{B}+1}\\ &+\frac{3b_i^3}{\Delta\tilde{x}^3}\left(\frac{3b_i-b0}{2b0^2(b_i+b0)(b_i+2b0)}\right)f_{i,\tilde{B}+2}\end{aligned} \tag{B.2b}$$

$$\begin{aligned}f_{\tilde{x}\tilde{x}\tilde{x}}(p_{i,j=\tilde{B}+1}) =& -\frac{12}{\Delta\tilde{x}^3}\left(\frac{b0^4}{b_i(b_i+b0)(b+2b0)(b_i+3b0)}\right)f_{i,\tilde{B}-1}\\ &-\frac{1}{\Delta\tilde{x}^3}\left(\frac{b_i-2b0}{b_i}\right)f_{i,\tilde{B}}\\ &+\frac{3}{\Delta\tilde{x}^3}\left(\frac{b_i-b0}{b_i+b0}\right)f_{i,\tilde{B}+1}\\ &-\frac{3}{\Delta\tilde{x}^3}\left(\frac{b_i}{b_i+2b0}\right)f_{i,\tilde{B}+2}\\ &+\frac{1}{\Delta\tilde{x}^3}\left(\frac{b_i+b0}{b_i+3b0}\right)f_{i,\tilde{B}+3}\end{aligned} \tag{B.2c}$$

$$\begin{aligned}f_{\tilde{x}\tilde{x}y}(p_{i,j=\tilde{B}}) =& \frac{1}{\Delta\tilde{x}^2\Delta y}\left(\frac{b_i}{b_i+b0}\right)(f_{i+1,\tilde{B}-1}-f_{i-1,\tilde{B}-1})\\ &-\frac{1}{\Delta\tilde{x}^2\Delta y}\left(\frac{b_i}{b0}\right)(f_{i+1,\tilde{B}}-f_{i-1,\tilde{B}})\\ &+\frac{1}{\Delta\tilde{x}^2\Delta y}\left(\frac{b_i^2}{b0(b_i+b0)}\right)(f_{i+1,\tilde{B}+1}-f_{i-1,\tilde{B}+1})\end{aligned} \tag{B.2d}$$

$$\begin{aligned}f_{\tilde{x}yy}(p_{i,j=\tilde{B}}) =& -\frac{1}{\Delta\tilde{x}\Delta y^2}\left(\frac{b0}{b_i+b0}\right)(f_{i+1,\tilde{B}-1}-2f_{i,\tilde{B}-1}+f_{i-1,\tilde{B}-1})\\ &-\frac{1}{\Delta\tilde{x}\Delta y^2}\left(\frac{b_i-b0}{b0}\right)(f_{i+1,\tilde{B}}-2f_{i,\tilde{B}}+f_{i-1,\tilde{B}})\\ &+\frac{1}{\Delta\tilde{x}\Delta y^2}\left(\frac{b_i^2}{b0(b_i+b0)}\right)(f_{i+1,\tilde{B}+1}-2f_{i,\tilde{B}+1}+f_{i-1,\tilde{B}+1})\end{aligned} \tag{B.2e}$$

Bibliography

Agnon, Y., Madsen, P. A., and Schäffer, H. A. (1999). A new approach to high-order Boussinesq models. *Journal of Fluid Mechanics*, *399*, 319–333.

Altomare, C., Crespo, A. J. C., Rogers, B. D., Domínguez, J. M., Gironella, X., and Gómez-Gesteira, M. (2014). Numerical modelling of armour block sea breakwater with smoothed particle hydrodynamics. *Computers & Structures*, *130*, 34–45.

Baldock, T. E. (1995). *Non-linear transient water waves*. Ph.D. thesis, Imperial College London (University of London).

Battjes, J. A. (1974). Surf similarity. In *Proceedings of the 14th Coastal Engineering Conference*, (pp. 466–480). American Society of Civil Engineers.

Bellotti, G., and Brocchini, M. (2002). On using Boussinesq-type equations near the shoreline: a note of caution. *Ocean Engineering*, *29*(12), 1569–1575.

Berkhoff, J. C. W. (1972). Computation of combined refraction-diffraction. In *Coastal Engineering 1972*, (pp. 471–490). ASCE.

Bijker, E. W. (1966). The increase of bed shear in a current due to wave motion. *Proc. 10th Int. Conf. on Coastal Engineering, ASCE*, (pp. 746–765).

Boccotti, P. (1983). Some new results on statistical properties of wind waves. *Applied Ocean Research*, *5*(3), 134–140.

Booij, N. (1981). *Gravity waves on water with non-uniform depth and current*. Ph.D. thesis, Delft University of Technology.

Borthwick, A. G. L., and Barber, R. W. (1992). River and reservoir flow modelling using the transformed shallow water equations. *International Journal for Numerical Methods in Fluids*, *14*, 1193 – 1217.

Borthwick, A. G. L., and Foote, Y. L. M. (2002). Wave-induced nearshore currents at a tri-cuspate beach in the UKCRF. *Proceedings of the Institution of Civil Engineers: Water and Maritime Engineering*, *154*(4), 251–263.

Borthwick, A. G. L., Ford, M., Weston, B. P., Taylor, P. H., and Stansby, P. K. (2006). Solitary wave transformation, breaking and run-up at a beach. *Proceedings of the Institution of Civil Engineers: Maritime Engineering*, *159*(MA3), 97–105.

Boussinesq, J. (1872). Théorie des ondes et des remous qui se propagent le long d'un canal rectangulaire horizontal, en communiquant au liquide contenu dans ce canal des vitesses sensiblement pareilles de la surface au fond. *Journal de Mathématiques Pures et Appliquées*, (pp. 55–108).

Bowen, M. K., and Smith, R. (2005). Derivative formulae and errors for non-uniformly spaced points. In *Proceedings of the Royal Society of London A: Mathematical, Physical and Engineering Sciences*, vol. 461, (pp. 1975–1997). The Royal Society.

Bradford, S. F., and Sanders, B. F. (2002). Finite volume schemes for the Boussinesq equations. In B. L. Edge, and J. M. Hemsley (Eds.) *Ocean Wave Measurement and Analysis (2001)*, vol. 273, (pp. 953–962). ASCE.

Brufau, P., Vzquez-Cendon, M. E., and Garca-Navarro, P. (2002). A numerical model for the flooding and drying of irregular domains. *International Journal for Numerical Methods in Fluids*, *39*(3), 247–275.

Catálan, P. A., and Haller, M. C. (2008). Remote sensing of breaking wave phase speeds with application to non-linear depth inversions. *Coastal Engineering*, *55*(1), 93–111.

Chen, Q., Dalrymple, R., Kirby, J., Kennedy, A., and Haller, M. (1999). Boussinesq

modeling of a rip current system. *Journal of Geophysical Research*, *104*(C9), 20,617–20,637.

Chen, Q., Kirby, J. T., Dalrymple, R. A., Kennedy, A. B., and Chawla, A. (2000). Boussinesq modeling of wave transformation, breaking, and runup. II: 2D. *Journal of Waterway, Port, Coastal, and Ocean Engineering*, *126*(1), 48–56.

Chen, Q., Kirby, J. T., Dalrymple, R. A., Shi, F., and Thornton, E. B. (2003). Boussinesq modeling of longshore currents. *Journal of Geophysical Research: Oceans*, *108*(C11).

da Silva Lima, S. (1981). *Wave-induced nearshore currents*. Ph.D. thesis, Liverpool University.

Dalrymple, R. A., and Rogers, B. D. (2006). Numerical modeling of water waves with the SPH method. *Coastal Engineering*, *53*(2), 141–147.

De Rouck, J., Verhaeghe, H., and Geeraerts, J. (2009). Crest level assessment of coastal structures—general overview. *Coastal Engineering*, *56*(2), 99–107.

Dean, R. G., and Dalrymple, R. (1991). *Water Wave Mechanics for Engineers and Scientists*, vol. Advanced Series on Ocean Engineering, Volume 2. World Scientific.

Dodd, N. (1998). Numerical model of wave run-up, overtopping, and regeneration. *Journal of Waterway, Port, Coastal, and Ocean Engineering*, *124*(2), 73–81.

Falconer, R. A. (1993). An introduction to nearly horizontal flows. *Coastal Estuarial and Harbour Engineers, E and FN Spon Ltd, London*, (pp. 27–36).

Fenton, J. D. (1990). Nonlinear wave theories. *Ocean Engineering Science: The Sea*, *9*(Part A), 3–25.

Fitzgerald, C. J., Taylor, P. H., Orszaghova, J., Borthwick, A. G. L., Whittaker, C., and Raby, A. C. (2016). Irregular wave runup statistics on plane beaches: Application of a Boussinesq-type model incorporating a generating–absorbing sponge layer and second-order wave generation. *Coastal Engineering*, *114*, 309–324.

Fraccarollo, L., and Toro, E. F. (1995). Experimental and numerical assessment of the shallow water model for two-dimensional dam-break type problems. *Journal of Hydraulic Research*, *33*(6), 843–864.

Gobbi, M. F., Kirby, J. T., and Wei, G. E. (2000). A fully nonlinear Boussinesq model for surface waves. Part 2. Extension to $O(kh)^4$. *Journal of Fluid Mechanics*, *405*, 181–210.

Guza, R. T., and Thornton, E. B. (1982). Swash oscillations on a natural beach. *Journal of Geophysical Research: Oceans*, *87*(C1), 483–491.

Harten, A., Lax, P., and van Leer, B. (1983). On upstream differencing and godunov-type schemes for hyperbolic conservation laws. *Journal of Computational Physics*, *50*, 235–269.

Hestenes, M. R., and Stiefel, E. (1952). Methods of conjugate gradients for solving linear systems. *Journal of Research of the National Bureau of Standards*, *49*(6).

Hunt, A. (2003). *Extreme Waves , Overtopping and Flooding at Sea Defences*. Ph.D. thesis, University of Oxford.

Hunt, I. A. (1959). Design of sea-walls and breakwaters. *Transactions of the American Society of Civil Engineers*, *126*(4), 542–570.

Hunt-Raby, A. C., Borthwick, A. G. L., Stansby, P. K., and Taylor, P. H. (2011). Experimental measurement of focused wave group and solitary wave overtopping. *Journal of Hydraulic Research*, *49*(4), 450–464.

Inman, D. L., Tait, R. J., and Nordstrom, C. E. (1971). Mixing in the surf zone. *Journal of Geophysical Research*, *76*(15), 3493–3514.

Jalali, M. R., and Borthwick, A. G. L. (2017). One-dimensional and two-dimensional Green–Naghdi equations for sloshing in shallow basins. *Proceedings of the Institution of Civil Engineers-Engineering and Computational Mechanics*, (pp. 1–22).

Jonathan, P., and Taylor, P. H. (1997). On irregular, nonlinear waves in a spread sea. *Transactions-American Society of Mechanical Engineers: Journal of Offshore Mechanics and Arctic Engineering*, *119*, 37–41.

Jonsson, I. (1966). The friction factor for a current superimposed by waves. Tech. Rep. 11, Coastal Engineering an dHydraulic Laboratory, Technical University of Denmark.

Karambas, T. V., and Koutitas, C. (1992). A breaking wave propagation model based on the Boussinesq equations. *Coastal Engineering*, *18*(1-2), 1–19.

Kawahara, M., and Umetsu, T. (1986). Finite Element Method for Moving Boundary Problems in River Flow. *International Journal for Numerical Methods in Fluids*, *6*, 365–386.

Kim, D.-H. (2015). H2D morphodynamic model considering wave, current and sediment interaction. *Coastal Engineering*, *95*, 20–34.

Kinsman, B. (1965). *Wind waves: their generation and propagation on the ocean surface*. Courier Corporation.

Kirby, J. T. (1984). A note on linear surface wave-current interaction over slowly varying topography. *Journal of Geophysical Research: Oceans*, *89*(C1), 745–747.

Kobayashi, N. (1999). Wave runup and overtopping on beaches and coastal structures. *Advances in Coastal and Ocean Engineering*, *5*, 95–154.

Lepelletier, T. G., and Raichlen, F. (1987). Harbor oscillations induced by nonlinear transient long waves. *Journal of Waterway, Port, Coastal, and Ocean Engineering*, *113*(4), 381–400.

Liang, Q., and Borthwick, A. G. L. (2009). Adaptive quadtree simulation of shallow flows with wet-dry fronts over complex topography. *Computers and Fluids*, *38*, 221–234.

Lin, P., and Liu, P. L.-F. (1998). A numerical study of breaking waves in the surf zone. *Journal of Fluid Mechanics*, *359*(1), 239–264.

Lindgren, G. (1970). Some properties of a normal process near a local maximum. *The Annals of Mathematical Statistics*, (pp. 1870–1883).

Longuet-Higgins, M. S., and Stewart, R. (1960). Changes in the form of short gravity waves on long waves and tidal currents. *Journal of Fluid Mechanics*, *8*(4), 565–583.

Lynett, P. J., and Liu, P. L.-F. (2004). Linear analysis of the multi-layer model. *Coastal Engineering*, *51*(5), 439–454.

Madsen, P. A., Bingham, H. B., and Schäffer, H. A. (2003). Boussinesq-type formulations for fully nonlinear and extremely dispersive water waves: derivation and analysis. In *Proceedings of the Royal Society of London A: Mathematical, Physical and Engineering Sciences*, vol. 459, (pp. 1075–1104). The Royal Society.

Madsen, P. A., Fuhrman, D. R., and Wang, B. (2006). A Boussinesq-type method for fully nonlinear waves interacting with a rapidly varying bathymetry. *Coastal Engineering*, *53*(5), 487–504.

Madsen, P. A., and Schäffer, H. A. (1998). Higher-order boussinesq-type equations for surface gravity waves: Derivation and analysis. *Philosophical Transactions: Mathematical, Physical and Engineering Sciences*, *356*(1749), 3123–3184.

Madsen, P. A., and Schäffer, H. A. (1999). A review of boussinesq-type equations for surface gravity waves. *Advances in Coastal and Ocean Engineering*, *5*, 1–94.

Madsen, P. A., and Sørensen, O. R. (1992). A new form of the boussinesq equations with improved linear dispersion characteristics. Part 2. A slowly-varying bathymetry. *Coastal Engineering*, *18*, 183–204.

Madsen, P. A., Sørensen, O. R., and Schäffer, H. A. (1997). Surf zone dynamics simulated by a boussinesq type model. Part I. Model description and cross-shore motion of regular waves. *Coastal Engineering*, *32*(4), 255–287.

Martins, K., Blenkinsopp, C. E., and Zang, J. (2015). Monitoring individual wave characteristics in the inner surf with a 2-dimensional laser scanner (lidar). *Journal of Sensors*, *2016*.

McCabe, M. V., Stansby, P. K., and Apsley, D. D. (2013). Random wave runup and overtopping a steep sea wall: Shallow-water and boussinesq modelling with generalised breaking and wall impact algorithms validated against laboratory and field measurements. *Coastal Engineering*, *74*, 33–49.

McGranahan, G., Balk, D., and Anderson, B. (2007). The rising tide: assessing the risks of climate change and human settlements in low elevation coastal zones. *Environment and Urbanization*, *19*(1), 17–37.

Monaghan, J. J. (1994). Simulating free surface flows with sph. *Journal of Computational Physics*, *110*(2), 399–406.

Munk, W. H. (1949). Surf beats. *Trans. American Geophysical Union*, *30*(6), 849–854.

Nwogu, O. (1993). Alternative form of boussinesq equations for nearshore wave propagation. *Journal of Waterway, Port, Coastal, and Ocean Engineering*, *119*(6), 618–638.

Orszaghova, J. (2011). *Solitary waves and wave groups at the shore*. Ph.D. thesis, University of Oxford.

Orszaghova, J., Borthwick, A. G. L., and Taylor, P. H. (2012). From the paddle to the beach – A Boussinesq shallow water numerical wave tank based on Madsen and Sørensen's equations. *Journal of Computational Physics*, *231*(2), 328–344.

Park, K.-Y., and Borthwick, A. G. L. (2001). Quadtree grid numerical model of nearshore wave–current interaction. *Coastal Engineering*, *42*(3), 219–239.

Peregrine, D. H. (1967). Long waves on a beach. *Journal of Fluid Mechanics*, *27*(04), 815–827.

Pringle, W. J., Yoneyama, N., and Mori, N. (2016). Two-way coupled long wave-rans model: Solitary wave transformation and breaking on a plane beach. *Coastal Engineering*, *114*, 99–118.

Radder, A. C., and Dingemans, M. W. (1985). Canonical equations for almost periodic, weakly nonlinear gravity waves. *Wave Motion*, *7*(5), 473–485.

Rogers, B. D., Borthwick, A. G. L., and Taylor, P. H. (2004). Godunov-type adaptive grid model of wave-current interaction at cuspate beaches. *International Journal for Numerical Methods in Fluids*, *46*, 569–606.

Rogers, B. D., Fujihara, M., and Borthwick, A. G. L. (2001). Adaptive q-tree godunov-type scheme for shallow water equations. *International Journal for Numerical Methods in Fluids*, *35*(3), 247–280.

Sampson, J., Easton, A., and Singh, M. (2006). Moving boundary shallow water flow above parabolic bottom topography. *ANZIAM J.*, *47*, C373–C387.

Sarpkaya, T., and Isaacson, M. (1981). *Mechanics of wave forces on offshore structures*. New York: Van Nostrand Reinhold.

Schäffer, H. A., Madsen, P. A., and Deigaard, R. (1993). A boussinesq model for waves breaking in shallow water. *Coastal Engineering*, *20*(3-4), 185–202.

Shewchuk, J. R. (1994). An introduction to the conjugate gradient method without the agonizing pain. Tech. rep., School of Computer Science, Carnegie Mellon University.

Shi, F., Kirby, J. T., Harris, J. C., Geiman, J. D., and Grilli, S. T. (2012). A high-order adaptive time-stepping tvd solver for boussinesq modeling of breaking waves and coastal inundation. *Ocean Modelling*, *43*, 36–51.

Shiach, J. B., and Mingham, C. G. (2009). A temporally second-order accurate godunov-type scheme for solving the extended boussinesq equations. *Coastal Engineering*, *56*(1), 32 – 45.

Stive, M. J. F. (1980). Velocity and pressure field of spilling breakers. In *Coastal Engineering 1980*, (pp. 547–566).

Svendsen, I. A. (1984). Mass flux and undertow in a surf zone. *Coastal Engineering*, *8*(4), 347–365.

Svendsen, I. A., Madsen, P. Å., and Burh Hansen, J. (1978). Wave characteristics in the surf zone. In *Coastal Engineering 1978*, (pp. 520–539).

Taylor, P. H., and Williams, B. A. (2004). Wave statistics for intermediate depth water-newwaves and symmetry. *Transactions-American Society of Mechanical Engineers: Journal of Offshore Mechanics and Arctic Engineering*, *126*(1), 54–59.

Thacker, W. C. (1981). Some exact solutions to the nonlinear shallow-water wave equations. *Journal of Fluid Mechanics*, *107*, 499–508.

Thornton, E. B. (1970). Variation of longshore current across the surf zone. *Proc. 12th Conf. Coastal Engineering, ASCE*, (pp. 291–308).

Thornton, E. B., and Guza, R. T. (1982). Energy saturation and phase speeds measured on a natural beach. *Journal of Geophysical Research: Oceans*, *87*(C12), 9499–9508.

Tonelli, M., and Petti, M. (2009). Hybrid finite volume–finite difference scheme for 2dh improved boussinesq equations. *Coastal Engineering*, *56*(5), 609–620.

Tonelli, M., and Petti, M. (2012). Shock-capturing boussinesq model for irregular wave propagation. *Coastal Engineering*, *61*, 8–19.

Troch, P. (1998). Mildwave–a numerical model for propagation and transformation of linear water waves. *Department of Civil Engineering, Ghent University, Ghent*.

Tromans, P. S., Anaturk, A. R., Hagemeijer, P., et al. (1991). A new model for the kinematics of large ocean waves-application as a design wave. In *The First International Offshore and Polar Engineering Conference*. International Society of Offshore and Polar Engineers.

van der Meer, J. W. (1998). Wave run-up and overtopping. *Dikes and Revetments: Design, Maintenance and Safety Assessment, ed. KW Pilarczyk (AA Balkema, Rotterdam, The Netherlands)*, (pp. 145–159).

van der Meer, J. W., Allsop, N. W. H., Bruce, T., De Rouck, J., Kortenhaus, A., Pullen, T., Schüttrumpf, H., Troch, P., and Zanuttigh, B. (2016). Eurotop: Manual on wave overtopping of sea defences and related sturctures-an overtopping manual largely based on european research, but for worlwide application.

Wei, G., and Kirby, J. T. (1995). Time-Dependent Numerical Code for Extended Boussinesq Equations. *Journal of Waterway, Port, Coastal, and Ocean Engineering*, *121*(October), 251–261.

Wei, G., Kirby, J. T., Grilli, S. T., Subramanya, R., et al. (1995). A fully nonlinear boussinesq model for surface waves. Part 1. Highly nonlinear unsteady waves. *Journal of Fluid Mechanics*, *294*(13), 71–92.

Yoo, D. (1986). *Mathematical modelling of wave-current interacted flow in shallow waters.*. Ph.D. thesis, University of Manchester.

Yoon, S. B., and Liu, P. L.-F. (1989). Interactions of currents and weakly nonlinear water waves in shallow water. *Journal of Fluid Mechanics*, *205*, 397–419.

Zhou, Z., Sangermano, J., Hsu, T.-J., and Ting, F. C. K. (2014). A numerical investigation of wave-breaking-induced turbulent coherent structure under a solitary wave. *Journal of Geophysical Research: Oceans*, *119*(10), 6952–6973.